

Numerical Simulation of Shock-Induced Combustion for
Application to the Ram Accelerator Concept

by

Shaye Yungster

A dissertation submitted in partial fulfillment
of the requirements for the degree of

Doctor of Philosophy

University of Washington

1989

Approved by



(Chairperson of Supervisory Committee)

Program Authorized

to Offer Degree

Aeronautics and Astronautics

Date

October 16 1989

In presenting this dissertation in partial fulfillment of the requirements for the Doctoral degree at the University of Washington, I agree that the Library shall make its copies freely available for inspection. I further agree that extensive copying of this dissertation is allowable only for scholarly purposes, consistent with "fair use" as prescribed in the U. S. Copyright Law. Requests for copying or reproduction of this dissertation may be referred to University Microfilms, 300 North Zeeb Road, Ann Arbor, Michigan 48106, to whom the author has granted "the right to reproduce and sell (a) copies of the manuscript in microform and/or (b) printed copies of the manuscript made for microform."

is assumed. The flow, combustion phenomena, and performance characteristics of the engine are being investigated for use in a microform.

Signature Shaye Jungster

Date October 16 1989

University of Washington

Abstract

Numerical Simulation of Shock-Induced Combustion for Application to the Ram Accelerator Concept

by Shaye Yungster

Chairperson of Supervisory Committee:

Prof. A. P. Bruckner

Dept. of Aeronautics and Astronautics

A numerical scheme for calculating hypersonic flows involving shock-induced combustion is presented. The scheme is applied to a hypervelocity mass launcher concept known as the "ram accelerator". The analysis is carried out using a TVD numerical scheme that includes nonequilibrium chemistry, real gas effects, and a 7 species-8 reaction combustion model for hydrogen/oxygen mixtures. Inviscid flow is assumed. The flow, combustion phenomena, and performance characteristics of the ram accelerator are investigated for several projectile configurations in the superdetonative velocity range of 5.0 to 10.0 km/s. The distribution of various physical quantities along the ram accelerator, as well as temperature contours, are presented. Plots of ballistic efficiency and thrust pressure ratio are also included. Ballistic efficiencies of up to 28% and thrust pressure ratios as high as 17% were obtained. The effects of nose blunting on the flow and combustion processes in the ram accelerator are also investigated for a particular configuration. Several code validation tests are presented. In particular, the hypersonic, exothermic blunt body flow problem is examined in detail for mixtures of hydrogen/oxygen and hydrogen/air, and the numerical results are compared with experimental results.

TABLE OF CONTENTS

List of Figures	iv
List of Tables	viii
List of Symbols	ix
Chapter 1 Introduction	1
Chapter 2 Numerical Formulation	5
2.1 Nondimensional Variables	5
2.2 Governing Equations	6
2.3 Combustion Model	9
2.4 Calculation of the chemical source term	11
2.5 Numerical Method	12
2.6 Further Simplification	16
2.7 Boundary conditions	17
Chapter 3 Benchmark Test Cases	20
3.1 Nonreacting, Perfect Gas Studies	20
3.1.1 Wedge at $M=10$	20
3.1.2 Sphere at $M=2.94$	22
3.1.3 Sphere at $M=20$	22
3.2 Single-Reaction, Real Gas Studies	22
3.2.1 Illustration of the Point Implicit Technique	25
3.2.2 Wedge at $M=7$	26
3.2.3 Spheres at $M=6$	30
Chapter 4 Exothermic Blunt Body Flow	32
4.1 Subdetonative speeds	33

4.2	Superdetonative speeds	35
4.3	Comparison with F3d/Chem code	40
Chapter 5 Ram Accelerator Studies		45
5.1	Performance as a function of Mach number	45
5.2	Ballistic efficiency and thrust pressure ratio	55
5.3	Performance as a function of area ratio	61
5.4	Performance as a function of gas mixture	61
5.5	Blunt nose effects	64
Chapter 6 Conclusions		74
List of References		76
Appendix A Expressions for the chemical source term		81
Appendix B Expressions for the dissipation terms		83
Appendix C Calculation of the scaling matrix		85
Appendix D TVD Schemes: Fundamental Concepts		89

LIST OF FIGURES

1.1	Schematic of oblique detonation ram accelerator drive mode. . . .	2
2.1	Generalized coordinate transformation	8
2.2	Boundary condition at the wall	18
3.1	Wedge flow considered in section 3.1.1	21
3.2	Nondimensional pressure results for a $M = 10$ wedge flow.	21
3.3	Sphere in supersonic flow, $M = 2.94$	23
3.4	Surface pressure comparison for a sphere, $M = 2.94$	23
3.5	Sphere in hypersonic flow, $M = 20$	24
3.6	Wedge flow considered in section 3.2.2	28
3.7	Nondimensional pressure results for a $M = 7$ wedge flow with oxygen dissociation.	29
3.8	Degree of dissociation for a $M = 7$ wedge flow with oxygen disso- ciation.	29
3.9	Temperature variation along the stagnation streamline for a $M = 6$ sphere flow with oxygen dissociation.	31
3.10	Degree of dissociation along the stagnation streamline for a $M = 6$ sphere flow with oxygen dissociation.	31
4.1	Shock wave and combustion front in a stoichiometric H_2/O_2 mix- ture at $M=3.55$ (from Ref. 44)	34
4.2	Temperature contours (T/T_∞) for stoichiometric H_2/O_2 , $M=3.55$ flow past a sphere. Experimental shock location obtained from Fig. 4.1.	34
4.3	Distribution of physical quantities along the stagnation streamline for the $M = 3.55$ case.	36
4.4	Shock wave and combustion front in a stoichiometric H_2/air mix- ture at $M=4.18$ (from Ref. 44)	37

4.5	Temperature contours (T/T_∞) for stoichiometric H_2/air , $M=4.18$ flow past a sphere. Experimental shock location obtained from Fig. 4.4.	37
4.6	Distribution of physical quantities along the stagnation streamline for the $M = 4.18$ case.	38
4.7	Overdriven detonation and oblique Chapman-Jouguet detonation in a stoichiometric H_2/O_2 mixture at $M=5.08$ (from Ref. 44) . . .	39
4.8	Temperature contours (T/T_∞) for stoichiometric H_2/O_2 , $M=5.08$ flow past a sphere. Experimental shock location obtained from Fig. 4.7.	39
4.9	Distribution of physical quantities along the stagnation streamline for the $M = 5.08$ case.	41
4.10	Shock-deflagration system in a stoichiometric H_2/air mixture at $M=6.46$ (from Ref. 44)	42
4.11	Temperature contours (T/T_∞) for stoichiometric H_2/air , $M=6.46$ flow past a sphere. Experimental shock location obtained from Fig. 4.10.	42
4.12	Distribution of physical quantities along the stagnation streamline for the $M = 6.46$ case.	43
4.13	Temperature contours (T/T_∞) for stoichiometric H_2/air , $M=6.46$ flow past a sphere. Present method.	44
4.14	Temperature contours (T/T_∞) for stoichiometric H_2/air , $M=6.46$ flow past a sphere. Lee and Deiwert's method. ⁴⁶	44
5.1	Typical grid for the ram accelerator. Vertical direction is magnified by a factor of 5.	46
5.2	Ram accelerator configuration on a 1:1 scale.	46
5.3	(a)Temperature contours T/T_∞ ; (b)temperature distribution; for a 14° projectile. $U_1 = 5.2$ km/s ($M=7$), mixture: $2H_2 + O_2 + 5He$	48
5.4	(a)Temperature contours T/T_∞ ; (b)temperature distribution; for a 14° projectile. $U_1 = 5.9$ km/s ($M=8$), mixture: $2H_2 + O_2 + 5He$	49
5.5	(a)Temperature contours T/T_∞ ; (b)temperature distribution; for a 14° projectile. $U_1 = 6.7$ km/s ($M=9$), mixture: $2H_2 + O_2 + 5He$	50

5.6	(a)Temperature contours T/T_∞ ; (b)temperature distribution; for a 14° projectile. $U_1 = 8.1$ km/s ($M=11$), mixture: $2H_2 + O_2 + 5He$	51
5.7	Mach number distribution along the tube wall and projectile surface for the $M=8$ case.	53
5.8	Mach number distribution along the tube wall and projectile surface for the $M=9$ case.	53
5.9	Species mass fraction distribution along the projectile surface for the $M=8$ case.	54
5.10	Species mass fraction distribution along the projectile surface for the $M=9$ case.	54
5.11	Pressure distribution along the tube wall and projectile surface for the $M=7$ case.	56
5.12	Pressure distribution along the tube wall and projectile surface for the $M=8$ case.	56
5.13	Pressure distribution along the tube wall and projectile surface for the $M=9$ case.	57
5.14	Pressure distribution along the tube wall and projectile surface for the $M=11$ case.	57
5.15	(a)Temperature contours T/T_∞ ;(b)particle traces; for a 12° projectile. ($M = 11$), mixture: $2H_2 + O_2 + 5He$	58
5.16	Control Volume used for the ram accelerator	59
5.17	Ballistic efficiency as a function of ram accelerator projectile speed and Mach number for two projectile geometries. Mixture: $2H_2 + O_2 + 5He$	62
5.18	Thrust pressure ratio as a function of ram accelerator projectile speed and Mach number for two projectile geometries. Mixture: $2H_2 + O_2 + 5He$	62
5.19	Ballistic efficiency as a function of projectile-to-tube area ratio. Mixture: $2H_2 + O_2 + 5He$	63
5.20	Thrust pressure ratio as a function of projectile-to-tube area ratio. Mixture: $2H_2 + O_2 + 5He$	63
5.21	Nondimensional thrust as a function of Mach number.	65

5.22	Nondimensional thrust as a function of projectile speed.	65
5.23	Ballistic efficiency as a function of projectile speed.	66
5.24	Temperature contours (T/T_∞) for a 12° projectile. $U_1 = 7.98$ km/s ($M=10$), mixture: $5H_2 + O_2 + 4He$	66
5.25	Temperature contours (T/T_∞) for a 12° projectile. $U_1 = 8.77$ km/s ($M=11$), mixture: $5H_2 + O_2 + 4He$	67
5.26	Temperature contours (T/T_∞) for a 12° projectile. $U_1 = 9.57$ km/s ($M=12$), mixture: $5H_2 + O_2 + 4He$	67
5.27	Grid used for the blunt nose studies	69
5.28	Temperature contours (T/T_∞) for a blunt projectile. $M = 4.2$, nose radius $R = 0.06$ cm, mixture: stoichiometric H_2/air	70
5.29	Temperature contours (T/T_∞) in the nose region of the blunt pro- jectile.	70
5.30	Pressure contours (p/p_∞) for a blunt projectile. $M = 4.2$, nose radius $R = 0.06$ cm, mixture: stoichiometric H_2/air	72
5.31	Particle traces for the blunt projectile.	72
5.32	Comparison of pressure distribution on the projectile surface for reacting and frozen flows.	73
5.33	Comparison of temperature distribution on the projectile surface for reacting and frozen flows.	73

LIST OF TABLES

2.1	Reaction rate coefficients for hydrogen combustion	10
3.1	Rate coefficients for oxygen reaction	27
4.1	Experimental data on the exothermic blunt body flows	33
5.1	Properties of the four gas mixtures	68

LIST OF SYMBOLS

A	flux Jacobian matrix $A = \frac{\partial F}{\partial q}$
A_p	maximum projectile cross sectional area
A_t	tube cross sectional area
a	frozen speed of sound (defined in Eq. B8)
a_j	eigenvalues of A
a_k	eigenvalues of B
B	flux Jacobian matrix $B = \frac{\partial G}{\partial q}$
c_i	mass fraction ρ_i/ρ
c_p	specific heat at constant pressure of the gas mixture
c_{pi}	specific heat at constant pressure of species i
c_v	specific heat at constant volume of the gas mixture
c_{vi}	specific heat at constant volume of species i
c_∞	free stream speed of sound
D	Chapman-Jouguet detonation speed
D	scaling matrix (defined in Eq. 2.21)
Da	Damköhler number (defined in Eq. 2.15)
e	total energy per unit volume
F	Thrust
F	flux vector (ξ component)
G	flux vector (η component)
H	axisymmetric source term
h_0	total enthalpy per unit mass
h_i^0	heat of formation per unit mass of species i
I	unit matrix
J	grid Jacobian defined in Eq. 2.4
j	grid index along ξ
\hat{j}	parameter; $\hat{j} = 0$ for plane flow and $\hat{j} = 1$ for axisymmetric flow
k	grid index along η

$K_{b,j}$	backward rate constant of j th reaction
$K_{f,j}$	forward rate constant of j th reaction
L	characteristic length
M	Mach number, (also $M = \rho u$ in Appendix C)
M_i	molecular weight of species i
M_O	molecular weight of atomic oxygen (section 3.2.2)
N	momentum density $N = \rho v$
n	number of species in the combustion model, (also normal direction)
p	pressure
Q	rate of heat release into the flow (defined in Eq. 5.9)
\hat{Q}	"limiter" function (defined in Eq. 2.27)
\mathbf{q}	vector of conserved flow variables
R	universal gas constant, (also body nose radius)
\mathbf{R}_j	matrix of eigenvectors of \mathbf{A}
\mathbf{R}_k	matrix of eigenvectors of \mathbf{B}
R_∞	free stream gas constant
r	cylindrical radius
r_p	maximum projectile radius
r_t	tube radius
S	distance along projectile
$S(x)$	cross sectional area of projectile at station x
T	temperature
t	time coordinate
U	contravariant velocity (defined in Eq. 2.4)
U_1	projectile speed
u	velocity component in the x direction
V	contravariant velocity (defined in Eq. 2.4)
V_n	normal velocity component
V_t	tangential velocity component
v	velocity component in the y direction
\mathbf{W}	chemical source term
w_i	rate of change of the density of species i

x	horizontal coordinate
y	vertical coordinate
y_i	concentration of species i
$\dot{y}_{i,j}$	rate of change of the concentration of species i in reaction j
\dot{y}_i	total rate of change of the concentration of species i from all reactions

Greek Symbols

α	degree of dissociation
α	vector defined in Eq. 2.25
γ	ratio of specific heats
η	curvilinear coordinate normal to body surface
η_b	ballistic efficiency (defined in Eq. 5.2)
ξ	curvilinear coordinate along body surface
ρ	density
ρ_i	density of species i
τ_f	characteristic convection time
τ_{ch}	characteristic chemical time
Φ	dissipation vector
ϕ^l	elements of the dissipation vector (given in Eq. 2.23)
ϕ_t	thrust pressure ratio (defined in Eq. 5.15)

Superscripts

$(\bar{})$	dimensional quantity
$(\dot{})$	time derivative
$()^n$	time level n

Subscripts

$()_\infty$	free stream conditions
$()_e$	exit of control volume

ACKNOWLEDGMENTS

The author wishes to express his sincere appreciation to Dr. Adam Bruckner and to Professor Abraham Hertzberg for their guidance, support and encouragement during the course of this study. Their many suggestions greatly improved the quality of this work. In particular, it was a pleasure having had Dr. Bruckner as a thesis advisor. Special thanks are also due to Dr. Scott Eberhardt for his assistance in the development of the CFD code and for many helpful discussions. The author is also grateful to G. Smeets of the Institut Franco-Allemand de Reserches de Saint Louis, France, for supplying him with the original photographs of the projectiles flying through combustible gas mixtures. Finally, the author wishes to express his thanks to his family for their constant support.

This work was supported in part by USAF Contract No. F08635-84-K-0143, ONR Contract No. N000014-88-K-0565 and by a grant from the Olin Corporation.

DEDICATION

To Sonia, Nir and Yael

Chapter 1

INTRODUCTION

The possibility of using shock-induced combustion in hypersonic airbreathing engines and hypersonic mass launchers has been investigated during the last few years. Such an approach has been considered as an alternative to the supersonic combustion ramjet for propelling space transportation vehicles such as the NASP (National Aerospace Plane) in a configuration known as the Oblique Detonation Wave Engine (ODWE)^{1,2}.

Also, experimental and theoretical research is being carried out on a new ramjet-in-tube concept, developed at the University of Washington, known as the "ram accelerator"³⁻⁹. In this concept, a shaped projectile can, in principle, be accelerated efficiently to velocities up to 12 km/s by means of detonation waves or other shock-induced combustion modes. This concept is being experimentally and theoretically investigated at the University of Washington³⁻⁹. Also, Rom & Kivity¹⁰ have presented a preliminary analysis of hypervelocity accelerators utilizing oblique detonation waves.

Although several ram accelerator operation modes have been proposed³, our discussion will center on the "oblique detonation" mode shown in Fig. 1.1. In order to operate in this combustion mode, the projectile must fly at superdetonative speeds, i.e., speeds above the Chapman-Jouguet detonation speed of the gas mixture. Preliminary experimental evidence of ram accelerator operation in this velocity range was presented by Kull et.al.¹¹.

While the gas dynamic principles that govern the flow and combustion processes in the ram accelerator (operating in the "oblique detonation" mode) are similar to those related to hypersonic airbreathing propulsion systems, particularly to the ODWE concept, the device is operated in a different manner.

In the oblique detonation ram accelerator operation mode (Fig. 1.1), the center-body is a projectile fired into a tube filled with a premixed gaseous fuel/oxidizer

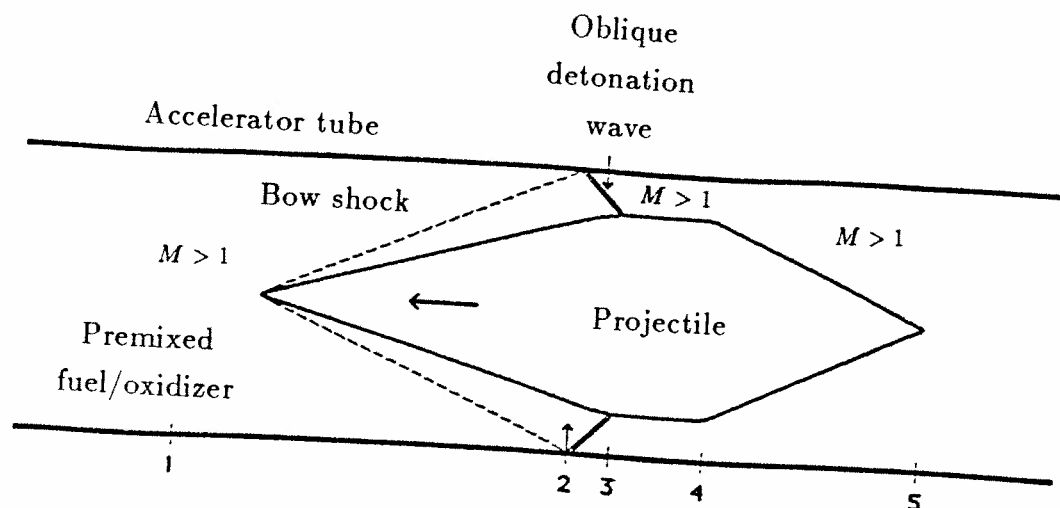


Figure 1.1: Schematic of oblique detonation ram accelerator drive mode.

There is no propellant on board the projectile. Ignition of the fuel/oxidizer mixture is achieved by means of a series of shock waves that increase its temperature until the ignition temperature is reached at some desired location. At this point, rapid chemical reactions release energy into the flowing stream. The energy addition will establish either a detonation wave or a coupled or decoupled shock-deflagration system, depending primarily on the mixture composition, pressure and tube size[†]. The combustion process creates a high pressure region over the back of the projectile, producing a thrust force. The pressure, composition, chemical energy density and speed of sound of the mixture can be controlled to optimize the performance for a given flight condition.

The ram accelerator concept has the potential for a number of applications, such as hypervelocity impact studies and direct launch to orbit of acceleration insensitive payloads^{12,13}. It also offers the possibility of studying flow fields and combustion processes of interest to hypersonic airbreathing vehicles.

[†]Such shock-induced combustion modes will be discussed in detail in Chapter 4

It is a known fact that computational fluid dynamics (CFD) is playing a major role in the development of hypersonic propulsion^{14,15}, due to its ability to predict, in principle, all the relevant flow and combustion phenomena at conditions for which experimental facilities do not currently exist. At the University of Washington, a CFD capability has also been developed, in support of the experimental effort, almost since its conception^{7-9,16}. These studies have improved our understanding of the ram accelerator, and will certainly continue to provide new information necessary for the achievement of higher speeds.

The present work, represents the latest effort in the development of new and efficient CFD techniques for the study of the ram accelerator concept operating in the "oblique detonation" mode. The new numerical technique developed is a departure from the previous CFD model described in Refs. 9 and 16. The earlier model was based on a global Arrhenius rate equation, with the Arrhenius constants determined from experimental ignition delay studies. The current model is more accurate in that it accounts for the reaction kinetics of a 7 species 8 reaction combustion model. Nonetheless, the earlier results were encouraging in that they predicted superdetonative operation was possible.

Therefore, one of the main contribution of the present study is the inclusion, for the first time, of reaction kinetics in computations of the ram accelerator concept.

The new numerical scheme has been validated/calibrated by using benchmark test cases for which analytical, numerical or experimental results are available. These validation tests will be presented in Chapters 3 and 4, following the description of the complete numerical scheme, which is presented in Chapter 2. In particular, the "exothermic blunt body flow" problem is described in detail. This type of flow, which consists of blunt projectiles flying into detonable gas mixtures, serves as an excellent benchmark test problem, since it includes shock-induced combustion phenomena ranging from decoupled and coupled shock-deflagration systems to overdriven and oblique detonation waves. In the present work, comparisons between experimental and numerical results on the exothermic blunt body flow problem are presented. Such numerical calculations are unique, in the sense that they represent the first successful numerical simulations ever conducted on the exothermic blunt body flow problem, with the aim of reproducing experimental results. Due to its

importance, the exothermic blunt body flow problem is presented in a separate chapter (Chapter 4).

Finally, the flow, combustion, and performance characteristics of several ram accelerator configurations in the superdetonative velocity range of 5.0 to 10.0 km/s are analyzed and discussed in Chapter 5.

Due to the similarity between the flow and combustion processes in the ram accelerator and those associated with hypersonic airbreathing engines, it is clear that the numerical studies presented here are also of direct value to the NASP.

Flow over a blunt body, remains a major challenge in the following sections, the chapter on hypersonic airbreathing engines.

Chapter 2

NUMERICAL FORMULATION

The fundamental flow and combustion processes in the ram accelerator, operating in the "oblique detonation" mode, can be simulated with the Euler equations, including finite rate chemistry and a combustion model. Viscous effects, although potentially important, are only of secondary importance. For this reason, and due to the fact that the computational resources required for conducting full Navier-Stokes calculations would exceed those presently available at the University of Washington, the present study is limited to inviscid flow. Aside from the additional computational resources needed, the proper modeling of some fundamental viscous, hypersonic flow phenomena, such as boundary layer transition, turbulent combustion and reacting separated flows, remains a major challenge.

In the following sections, the complete numerical formulation used in the present study is described in detail.

2.1 Nondimensional Variables

In order to simplify our analysis, it is convenient to introduce nondimensional variables. Denoting *dimensional* variables with the superscript (\sim), the following nondimensional variables are defined:

$$\begin{aligned}
 x &= \frac{\tilde{x}}{L} & y &= \frac{\tilde{y}}{L} & t &= \frac{\tilde{t}c_\infty}{L} \\
 \rho_i &= \frac{\tilde{\rho}_i}{\rho_\infty} & u &= \frac{\tilde{u}}{c_\infty} & v &= \frac{\tilde{v}}{c_\infty} \\
 e &= \frac{\tilde{e}}{\rho_\infty c_\infty^2} & p &= \frac{\tilde{p}}{\gamma_\infty p_\infty} & T &= \frac{\tilde{T}}{\gamma_\infty T_\infty} \\
 c_{p_i} &= \frac{\tilde{c}_{p_i}}{R_\infty} & R &= \frac{\tilde{R}}{R_\infty} & h_i^0 &= \frac{\tilde{h}_i^0}{c_\infty^2}
 \end{aligned} \tag{2.1}$$

In the above, x and y are the spatial coordinates, and t is time. u and v are the x and y velocity components respectively, p is pressure, e is the total energy per unit volume and ρ_i is the density of the i th species. T denotes the temperature, c_{pi} is the specific heat at constant pressure of the i th species, γ is the ratio of specific heats, R is the universal gas constant, and h_i^0 denotes the heat of formation per unit mass of the i th species. The subscript ∞ denotes free stream conditions, and R_∞ denotes the free stream gas constant. The free stream speed of sound is denoted by c_∞ .

With these nondimensionalization, the gasdynamic equations, presented in the next section, retain the exact same form as those for dimensional variables. The advantage of using nondimensional variables is that all of the conservative properties will be of order one, and the boundary conditions are simplified.

2.2 Governing Equations

As previously mentioned, the present study is limited to inviscid flow and considers two-dimensional or axisymmetric flow. For the case of chemically reacting flows, the Euler equations, with the global continuity equation replaced by all the species continuity equations, are used. They can be expressed in the following conservation form for a gas containing n species and in general curvilinear coordinates (ξ, η)

$$\frac{\partial \mathbf{q}}{\partial t} + \frac{\partial \mathbf{F}}{\partial \xi} + \frac{\partial \mathbf{G}}{\partial \eta} + \hat{j} \mathbf{H} = \mathbf{W} \quad (2.2)$$

where

$$\mathbf{q} = J^{-1} \begin{bmatrix} \rho_1 \\ \rho_2 \\ \vdots \\ \rho_n \\ \rho u \\ \rho v \\ e \end{bmatrix}, \quad \mathbf{F} = J^{-1} \begin{bmatrix} \rho_1 U \\ \rho_2 U \\ \vdots \\ \rho_n U \\ \rho u U + \xi_x p \\ \rho v U + \xi_y p \\ U(e + p) \end{bmatrix} \quad (2.3)$$

$$\mathbf{G} = J^{-1} \begin{bmatrix} \rho_1 V \\ \rho_2 V \\ \vdots \\ \rho_n V \\ \rho u V + \eta_x p \\ \rho v V + \eta_y p \\ V(e + p) \end{bmatrix}, \quad \mathbf{H} = \frac{J^{-1}}{r} \begin{bmatrix} \rho_1 v \\ \rho_2 v \\ \vdots \\ \rho_n v \\ \rho uv \\ \rho v^2 \\ v(e + p) \end{bmatrix}$$

$$\mathbf{W} = J^{-1} \begin{bmatrix} w_1 \\ w_2 \\ \vdots \\ w_n \\ 0 \\ 0 \\ 0 \end{bmatrix}$$

The equations describe two-dimensional flow if $\hat{j} = 0$ and axisymmetric flow if $\hat{j} = 1$. The variable r is the cylindrical radius. Here, ρ denotes the mixture density $\rho = \sum_{i=1}^n \rho_i$. The terms w_i represent the production of species from chemical reactions, and depend on the particular reaction mechanism being considered. Their calculation, using the standard methods of Ref. 17, is given in section 2.4 and in Appendix A. Finally, the grid Jacobian J and the contravariant velocities U and V are defined as follows

$$\begin{aligned} J^{-1} &= x_\xi y_\eta - x_\eta y_\xi \\ U &= \xi_x u + \xi_y v; \quad V = \eta_x u + \eta_y v \\ \xi_x &= J y_\eta; \quad \xi_y = -J x_\eta \\ \eta_x &= -J y_\xi; \quad \eta_y = J x_\xi \end{aligned} \tag{2.4}$$

The terms x_ξ , x_η , etc., are the grid metric terms $\frac{\partial x}{\partial \xi}$, $\frac{\partial x}{\partial \eta}$, etc.

Equations 2.2 to 2.4 were obtained from the Euler equations in Cartesian coordinates by means of a generalized coordinate transformation of the form $\xi = \xi(x, y)$

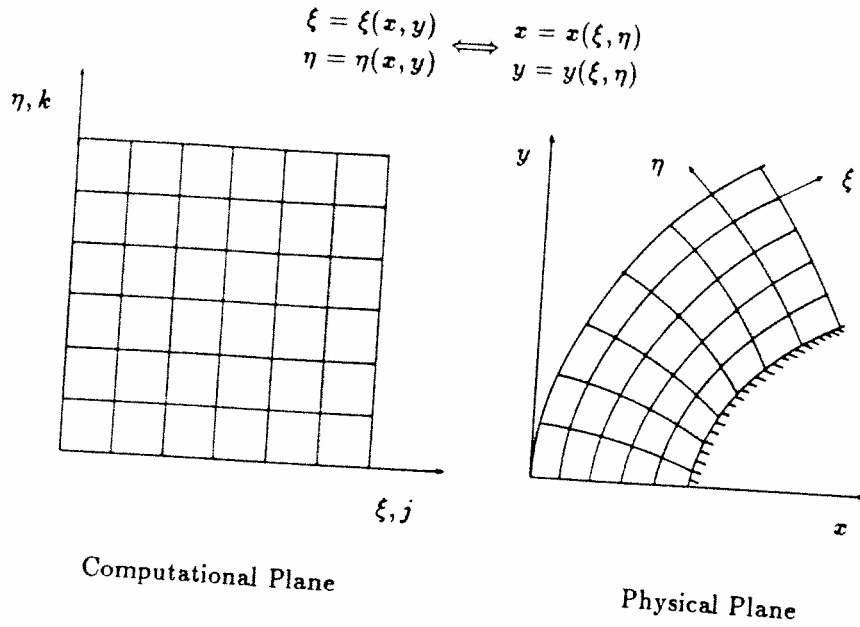


Figure 2.1: Generalized coordinate transformation

and $\eta = \eta(x, y)$ which is actually a mapping of physical points (x, y) to points in a computational plane (ξ, η) as shown in Fig. 2.1.

The equation of state used is that for a mixture of thermally perfect gases

$$p = \sum_{i=1}^n \frac{\rho_i}{M_i} RT \quad (2.5)$$

where M_i is the molecular weight of the i th species. The temperature T , is determined from the definition of the total energy :

$$\sum_{i=1}^n c_i \int^T c_{v,i} dT = \frac{e}{\rho} - \frac{1}{2}(u^2 + v^2) - \sum_{i=1}^n c_i h_i^0 \quad (2.6)$$

where $c_i = \rho_i/\rho$, $c_{v,i}$ is the specific heat at constant volume of the i th species, and h_i^0 is the heat of formation for species i . A Newton-Raphson iterative method is used to solve for the temperature. Only a few iterations (≤ 3) are necessary for convergence. Expressions for the specific heats as a function of temperature are obtained from the JANAF tables¹⁸ and use the following polynomial fit¹⁹

$$\frac{c_{p,i}}{R} = A_1 + A_2 T + A_3 T^2 + A_4 T^3 + A_5 T^4 \quad (2.7)$$

where A_1, \dots, A_5 are constants. The curve fit constants are given for three temperature ranges: 300 to 1000 °K, 1000 to 6000 °K and 6000 to 15000 °K.

It should be mentioned that recent work by Wada et.al.²⁰ has shown that the assumption of constant specific heat in calculating chemically reacting flows can lead to large errors, because temperatures (on which the reaction rates strongly depend) tend to be overestimated.

2.3 Combustion Model

The combustion model used for the present study is the one proposed by Moretti²¹ which consists of 6 reacting species H , O , H_2O , OH , O_2 , H_2 , and an inert species such as Argon or Nitrogen. Eight reactions are assumed to be significant:

1. $H + O_2 \rightleftharpoons OH + O$
2. $O + H_2 \rightleftharpoons OH + H$
3. $H_2 + OH \rightleftharpoons H + H_2O$
4. $2OH \rightleftharpoons O + H_2O$
5. $H_2 + X \rightleftharpoons 2H + X$
6. $H_2O + X \rightleftharpoons OH + H + X$
7. $OH + X \rightleftharpoons O + H + X$
8. $O_2 + X \rightleftharpoons 2O + X$

where X is any of the above seven species. The forward and backward reaction rates for the i th reaction, K_{fi} and K_{bi} , are given by expressions of the form

$$K_i = A_i T^{b_i} e^{-C_i/T} \quad (2.8)$$

The reaction coefficients A_i , b_i , and C_i were taken from Evans and Schexnayder²² and are listed in Table 2.1.

Table 2.1: Reaction rate coefficients for hydrogen combustion²²

Reaction No.	Forward rates [†]			Backward rates [†]		
	A_i	b_i	C_i	A_i	b_i	C_i
1	2.2×10^{14}	0.0	8455	1.5×10^{13}	0.0	0
2	7.5×10^{13}	0.0	5586	3.0×10^{13}	0.0	4429
3	2.0×10^{13}	0.0	2600	8.4×10^{13}	0.0	10116
4	5.3×10^{12}	0.0	503	5.8×10^{13}	0.0	9059
5	5.5×10^{18}	-1.0	51987	1.8×10^{18}	-1.0	0
6	5.2×10^{21}	-1.5	59386	4.4×10^{20}	-1.5	0
7	8.5×10^{18}	-1.0	50830	7.1×10^{18}	-1.0	0
8	7.2×10^{18}	-1.0	59340	4.0×10^{17}	-1.0	0

[†] rate constant $K_i = A_i T^{b_i} e^{-C_i/T}$ in $\text{cm}^3/\text{mole} - \text{s}$ or $\text{cm}^6/\text{mole}^2 - \text{s}$

Evans and Schexnayder analyzed hydrogen/air supersonic flames using the above system of 7 species and 8 reactions. The results were compared with those obtained with a system consisting of 12 species and 25 reactions. The main difference between the 8-reaction and the 25-reaction model was the addition of HO_2 , NO , and NO_2 . Reactions involving HO_2 molecules are important for low temperature ignition studies. The main conclusions of their study are :

1) Although the 25-reaction model was superior to the 8-reaction model for prediction of ignition (due to the presence of more reaction paths for the creation and depletion of free radicals such as H , O , and OH), once ignition occurs, the 8-reaction model results are as good as those from the 25-reaction model.

2) In a system where external means for ignition are provided or where spontaneous ignition is known to be fast, the 8-reaction system was found to be adequate.

More complicated models for hydrogen combustion have also been proposed^{23,24}. They differ from the 8-reaction model, mainly by the inclusion of HO_2 (hydroperoxyl) and H_2O_2 (hydrogen peroxide). For the ram accelerator studies, the inclusion of these species could be important at the lower Mach number flight regime, where

low temperature ignition occurs. At higher Mach numbers, such species are probably unimportant.

Finally, we should point out that relatively simple and fast combustion models for hydrogen combustion have been proposed^{25,26}. However, such models require the determination of several parameters, which are adjusted to agree with a given set of experimental data. For this reason, their range of applicability is, in general, somewhat limited. In computations involving fuels with a more complex chemical structure, such as hydrocarbons, the development of such "global" combustion models could be very useful.

2.4 Calculation of the chemical source term

The procedure for calculating the chemical source term \mathbf{W} appearing in equation (2.2) is described below. Only a general outline of the technique will be presented in this section. The detailed expressions for the terms w_i , based on the combustion model discussed above, are given in Appendix A. Also, note that dimensional variables are used in the following derivation.

Denote \tilde{y}_i as the concentration of species Y_i (in moles per cubic centimeter) and M_i as its molecular weight. Then

$$\tilde{y}_i = \frac{\tilde{\rho}_i}{M_i} \quad (2.9)$$

The chemical equation for a general elementary reaction j in a gas mixture containing n species can be written as

$$\sum_{s=1}^n \nu'_{s,j} Y_s \rightleftharpoons \sum_{s=1}^n \nu''_{s,j} Y_s \quad (2.10)$$

where $\nu'_{s,j}$ and $\nu''_{s,j}$ are the stoichiometric coefficients appearing on the left and right in reaction j . The rate of change of the concentration of species i in reaction j , $\dot{\tilde{y}}_{i,j}$, is given by¹⁷

$$\dot{\tilde{y}}_{i,j} = (\nu''_{i,j} - \nu'_{i,j}) K_{f,j} \prod_{s=1}^n \tilde{y}_s^{\nu'_{s,j}} + (\nu'_{i,j} - \nu''_{i,j}) K_{b,j} \prod_{s=1}^n \tilde{y}_s^{\nu''_{s,j}} \quad (2.11)$$

The total rate of change of the concentration of the i th species caused by all of the chemical reactions is

$$\dot{\bar{y}}_i = \sum_j \dot{\bar{y}}_{i,j} \quad (2.12)$$

The components w_i , of the chemical source term \mathbf{W} , are given by

$$\bar{w}_i = \dot{\bar{y}}_i M_i \quad (2.13)$$

The above expression represents the rate of change of the density of the i th species (in grams per second per cubic centimeter). When this expression is inserted into the nondimensional equations of motion (equation (2.2)), it is modified, giving the following final form

$$w_i = J^{-1} \frac{L}{c_\infty \rho_\infty} \bar{w}_i \quad (2.14)$$

Specific expressions for w_i based on the combustion model used in the present study are given in Appendix A.

2.5 Numerical Method

The equation set describing chemically reacting flows is difficult to solve due to the fact that it is mathematically stiff. Stiffness can be defined as the ratio of the largest to the smallest time scale. In reacting flows, the time scales associated with the chemistry tend to be much smaller than the time scale of fluid motion, sometimes by orders of magnitude. For the equation set being discussed here, the degree of stiffness is determined by the ratio of the characteristic convection time, τ_f , to the characteristic reaction time, τ_{ch} , a parameter known as the Damköhler number

$$Da = \frac{\tau_f}{\tau_{ch}} \quad (2.15)$$

In general there will be one Damköhler number associated with each chemical reaction.

There are currently two approaches to solving stiff systems of equations. One approach is to uncouple the fluid dynamics equations from the rate equations. Each timestep consists of a fluid dynamics step with frozen chemistry followed by a chemical reaction step (or several small steps) without flow interaction^{18,27}. The second

approach solves the fully coupled equation set simultaneously. This approach requires an implicit treatment of the chemical source terms which, as shown by Bussing and Murman²⁸, essentially rescales the equations in time so that all events occur on a similar pseudo-time scale. In the past few years, several algorithms have been developed for calculating nonequilibrium flows based on this approach.^{20,28-31} When the stiffness is entirely dominated by the chemistry (as is the case in the present study), the semi-implicit total variation diminishing (TVD)[†] method of Yee and Shinn³⁰ appears to be one of the most efficient methods available. However, if the stiffness is not solely dominated by the chemistry (e.g., stiffness due to viscous effects and/or a highly irregular grid), the fully implicit method of Park and Yoon³¹ (which is based on the LU-SGS implicit factorization scheme of Yoon and Jameson³²), would be a more efficient approach.

In the present study, the fully coupled inviscid equation set (2.2) is solved using a time marching method based on the TVD algorithm developed by Yee and Shinn³⁰, sometimes referred as the "Point Implicit TVD MacCormack" scheme. Yee and Shinn's scheme is, in turn, a slight modification of Roe's³³ one step TVD Lax-Wendroff scheme. The advantage of the predictor-corrector MacCormack scheme over the one-step Lax-Wendroff formulation lies in the more efficient manner in which the source terms are treated in multidimensional problems.

In the present study, the method of Yee and Shinn is extended to generalized coordinates and further modified to include real gas effects. Also, Yee and Shinn's studies have been limited so far to the use of the global two-step chemistry model of Rogers and Chinitz²⁵ for hydrogen/air combustion. In the present work, a more complex combustion model, which includes 7 species and 8 reactions, has been incorporated into the algorithm.

In generalized coordinates, for a grid spacing $\Delta\xi = \Delta\eta = 1$, and taking for simplicity $\hat{j} = 0$, the Point Implicit TVD MacCormack scheme is given by Predictor:

$$\begin{aligned} D_{j,k}^n \Delta q_{j,k}^{(1)} = & -\Delta t (F_{j,k}^n - F_{j-1,k}^n + G_{j,k+1}^n - G_{j,k}^n) \\ & + \Delta t W_{j,k}^n \end{aligned} \quad (2.16)$$

[†]A summary of the fundamental concepts associated with TVD methods is given in Appendix D.

Corrector:

$$\mathbf{q}_{j,k}^{(1)} = \Delta \mathbf{q}_{j,k}^{(1)} + \mathbf{q}_{j,k}^n \quad (2.17)$$

$$\begin{aligned} \mathbf{D}_{j,k}^1 \Delta \mathbf{q}_{j,k}^{(2)} = & \frac{1}{2} [-\Delta \mathbf{q}_{j,k}^{(1)} - \Delta t (\mathbf{F}_{j+1,k}^{(1)} - \mathbf{F}_{j,k}^{(1)} \\ & + \mathbf{G}_{j,k}^{(1)} - \mathbf{G}_{j,k-1}^{(1)})] + \frac{\Delta t}{2} \mathbf{W}_{j,k}^{(1)} \end{aligned} \quad (2.18)$$

$$\mathbf{q}_{j,k}^{(2)} = \Delta \mathbf{q}_{j,k}^{(2)} + \mathbf{q}_{j,k}^{(1)} \quad (2.19)$$

$$\begin{aligned} \mathbf{q}_{j,k}^{n+1} = \mathbf{q}_{j,k}^{(2)} & + [\mathbf{R}_{j+\frac{1}{2}}^n \Phi_{j+\frac{1}{2}}^n - \mathbf{R}_{j-\frac{1}{2}}^n \Phi_{j-\frac{1}{2}}^n] \\ & + [\mathbf{R}_{k+\frac{1}{2}}^n \Phi_{k+\frac{1}{2}}^n - \mathbf{R}_{k-\frac{1}{2}}^n \Phi_{k-\frac{1}{2}}^n] \end{aligned} \quad (2.20)$$

Here $\mathbf{R}_{j\pm\frac{1}{2}}$ denotes the matrix of eigenvectors of the flux Jacobian matrix $\mathbf{A} = \frac{\partial \mathbf{F}}{\partial \mathbf{q}}$ evaluated at some symmetric average of $\mathbf{q}_{j,k}$ and $\mathbf{q}_{j\pm 1,k}$, denoted as $\mathbf{q}_{j\pm\frac{1}{2}}$, and $\mathbf{R}_{k\pm\frac{1}{2}}$ denotes the matrix of eigenvectors of the flux Jacobian matrix $\mathbf{B} = \frac{\partial \mathbf{G}}{\partial \mathbf{q}}$ evaluated at $\mathbf{q}_{k\pm\frac{1}{2}}$. The "scaling matrix" \mathbf{D} is given by :

$$\mathbf{D}^n = (\mathbf{I} - \Delta t \theta \frac{\partial \mathbf{W}}{\partial \mathbf{q}}); \quad \mathbf{D}^1 = (\mathbf{I} - \frac{\Delta t}{2} \theta \frac{\partial \mathbf{W}}{\partial \mathbf{q}}) \quad (2.21)$$

where Δt is the time-step, and θ is a parameter in the range $0 \leq \theta \leq 1$. All our calculations were done with $\theta = 1$ for maximum numerical stability. The time-step is restricted by the CFL (Courant, Lewy and Friedrichs) condition^{34,35}, which in generalized coordinates is given by

$$\Delta t \leq \frac{1}{|U| + |V| + a \sqrt{\xi_x^2 + \xi_y^2} + a \sqrt{\eta_x^2 + \eta_y^2}} \quad (2.22)$$

where a is the frozen speed of sound. The elements, $\phi_{j+\frac{1}{2}}^l$, of the dissipation vector $\Phi_{j+\frac{1}{2}}$ are :

$$\phi_{j+\frac{1}{2}}^l = \frac{1}{2} [\Psi(\nu_{j+\frac{1}{2}}^l) - (\nu_{j+\frac{1}{2}}^l)^2] [\alpha_{j+\frac{1}{2}}^l - \hat{Q}_{j+\frac{1}{2}}^l] \quad (2.23)$$

$$\nu_{j+\frac{1}{2}}^l = \Delta t a_{j+\frac{1}{2}}^l \quad (2.24)$$

$$\alpha_{j+\frac{1}{2}}^l = \mathbf{R}_{j+\frac{1}{2}}^{-1} (\mathbf{q}_{j+1,k} - \mathbf{q}_{j,k}) \quad (2.25)$$

Here $a_{j+\frac{1}{2}}^l$ denotes the eigenvalues of A evaluated at $q_{j+\frac{1}{2}}$, and $\alpha_{j+\frac{1}{2}}^l$ denotes the elements of the vector $\alpha_{j+\frac{1}{2}}$. The function Ψ is :

$$\Psi(z) = \begin{cases} |z| & |z| \geq \epsilon \\ \frac{(z^2 + \epsilon^2)}{2\epsilon} & |z| < \epsilon \end{cases} \quad .05 \leq \epsilon \leq .2 \quad (2.26)$$

The "limiter" function $\hat{Q}_{j+\frac{1}{2}}$ used in this study is given by :

$$\hat{Q}_{j+\frac{1}{2}}^l = \minmod(\alpha_{j-\frac{1}{2}}^l, \alpha_{j+\frac{1}{2}}^l, \alpha_{j+\frac{3}{2}}^l) \quad (2.27)$$

where the *minmod* function of a list of arguments is equal to the smallest number in absolute value if the list of arguments is of the same sign, or is equal to zero if any argument is of the opposite sign. Alternative forms of the "limiter" function are given in Ref. 30, and are also presented in Appendix D. The eigenvalues and eigenvectors of the fully coupled chemically reacting equations were obtained by Eberhardt and Brown³⁶ in Cartesian coordinates. They have been extended to generalized coordinates and used for calculating the vectors $R\Phi$ appearing in equation (2.20). The resulting expressions for $R\Phi$ are given in Appendix B.

Besides solving the stiffness problem, this method has several desirable properties, such as second-order accuracy in space, robustness, and the ability to achieve high resolution of shock waves, without the spurious oscillations associated with the more classical second-order schemes. The main disadvantage of the method is, however, that the solutions are not in general time accurate, making the scheme suitable only for steady state calculations.

Before moving on to describe a simplification to the above scheme, it should be mentioned that when coupling chemical energy release to fluid dynamics, problems can arise when the chemical reactions are very fast (i.e. very large Damköhler numbers). For very fast chemistry, most of the heat release takes place in a very short distance behind the shock wave, and if the grid resolution is not high enough to capture this process, errors in the computed quantities, including temperature, can occur. Because of the strong dependence of the reaction rates on temperature, this situation can cause the release of energy much sooner than it should be released. The result can be runaway chemical reactions and nonphysical flame or detonation

velocities. One way to prevent this problem is to limit the Damköhler number to a value such that the heat release is distributed among at least two or three cells. This approach was taken in the present study; alternative approaches to this problem are discussed by Oran and Boris³⁷.

2.6 Further Simplification

One can simplify the predictor and corrector steps (equations (2.16) and (2.18)) by partitioning the vectors \mathbf{q} , \mathbf{F} , \mathbf{G} , \mathbf{W} and the matrix \mathbf{D} as follows:

$$\mathbf{q} = \begin{bmatrix} \mathbf{q}^I \\ \mathbf{q}^{II} \end{bmatrix} \quad \mathbf{q}^I = J^{-1} \begin{bmatrix} \rho_1 \\ \rho_2 \\ \vdots \\ \rho_{ns} \end{bmatrix} \quad \mathbf{q}^{II} = J^{-1} \begin{bmatrix} \rho_1 u \\ \rho_2 v \\ e \end{bmatrix} \quad (2.28)$$

$$\mathbf{F} = \begin{bmatrix} \mathbf{F}^I \\ \mathbf{F}^{II} \end{bmatrix} \quad \mathbf{G} = \begin{bmatrix} \mathbf{G}^I \\ \mathbf{G}^{II} \end{bmatrix} \quad (2.29)$$

$$\mathbf{W} = \begin{bmatrix} \mathbf{W}^I \\ \mathbf{W}^{II} \end{bmatrix} \quad \mathbf{W}^I = \begin{bmatrix} w_1 \\ w_2 \\ \vdots \\ w_{ns} \end{bmatrix} \quad \mathbf{W}^{II} = \begin{bmatrix} 0 \\ 0 \\ 0 \end{bmatrix} \quad (2.30)$$

$$\mathbf{D} = \begin{bmatrix} \mathbf{D}^{11} & \mathbf{D}^{12} \\ \mathbf{D}^{21} & \mathbf{D}^{22} \end{bmatrix} \quad (2.31)$$

Here \mathbf{D}^{21} is a null matrix and \mathbf{D}^{22} is an identity matrix. Expressions for the matrices \mathbf{D}^{11} and \mathbf{D}^{12} are given in Appendix C.

With the above definitions, the predictor and corrector steps are calculated by the following procedure: taking the predictor step, for example, one first solves for $(\Delta \mathbf{q}^{II})^{(1)}$ by

$$(\Delta \mathbf{q}^{II})_{j,k}^{(1)} = -\Delta t (\mathbf{F}_{j,k}^{II} - \mathbf{F}_{j-1,k}^{II} + \mathbf{G}_{j,k+1}^{II} - \mathbf{G}_{j,k}^{II})^n \quad (2.32)$$

then for $(\Delta \mathbf{q}^I)^{(1)}$ by

$$(\mathbf{D}_{j,k}^{11})^n (\Delta \mathbf{q}^I)_{j,k}^{(1)} = (RHS)^I - (\mathbf{W}_{j,k}^I)^n - (\mathbf{D}_{j,k}^{12})^n (\Delta \mathbf{q}^{II})_{j,k}^{(1)} \quad (2.33)$$

where $(RHS)^I$ is the right-hand side of equation (2.32) with all the indices "II" replaced by "I". Therefore, instead of inverting the \mathbf{D} matrix of dimension $(n + 3, n + 3)$, one only has to invert the \mathbf{D}^{11} matrix which is (n, n) . The same procedure can be applied to the corrector step.

2.7 Boundary conditions

In this section we will discuss the boundary conditions, focusing on the ram accelerator configuration (see Fig. 1.1). For this case, the boundary conditions are specified as follows:

The flow is supersonic ahead of the projectile so that all flow variables are known. The flow remains supersonic throughout the ram accelerator and, therefore, we can impose a zero-gradient outflow condition. The wall boundaries are specified by the following procedure: The velocity components u and v at the wall are obtained from the condition of zero normal velocity component at the wall. Referring to Fig. 2.2, the normal and tangential velocity components, denoted by V_n and V_t respectively, at a solid surface described by $\eta = \text{const}$ are given by

$$V_n = \frac{\eta_x u + \eta_y v}{\sqrt{\eta_x^2 + \eta_y^2}} \quad (2.34)$$

and

$$V_t = \frac{\eta_y u - \eta_x v}{\sqrt{\eta_x^2 + \eta_y^2}} \quad (2.35)$$

Solving for the velocity components u and v at the wall we obtain

$$\begin{pmatrix} u \\ v \end{pmatrix}_{\text{wall}} = \frac{1}{\sqrt{\eta_x^2 + \eta_y^2}} \begin{bmatrix} \eta_y & \eta_x \\ -\eta_x & \eta_y \end{bmatrix} \begin{pmatrix} V_t \\ V_n \end{pmatrix} \quad (2.36)$$

In the above equation, we specify $V_n = 0$ and V_t is obtained by extrapolation from the interior

$$V_t = \frac{(\eta_y)_{j,1} u_{j,2} - (\eta_x)_{j,1} v_{j,2}}{\sqrt{(\eta_x)_{j,1}^2 + (\eta_y)_{j,1}^2}} \quad (2.37)$$

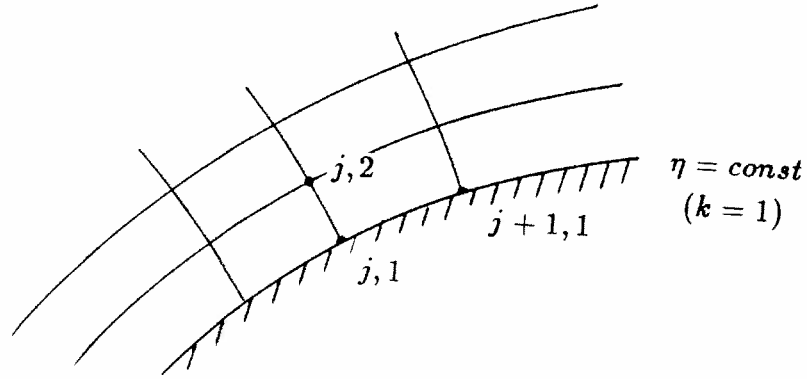


Figure 2.2: Boundary condition at the wall

The pressure is obtained by solving the normal momentum equation at the wall. This equation is obtained in the following way:

$$\frac{\partial p}{\partial n} = \frac{\eta_x \frac{\partial p}{\partial x} + \eta_y \frac{\partial p}{\partial y}}{\sqrt{\eta_x^2 + \eta_y^2}} \quad (2.38)$$

From the two momentum equations (in the x and y directions), the following expressions, valid for plane or axisymmetric flow, are obtained

$$-\frac{\partial p}{\partial x} = \rho \frac{\partial u}{\partial t} + \rho u \frac{\partial u}{\partial x} + \rho v \frac{\partial u}{\partial y} \quad (2.39)$$

$$-\frac{\partial p}{\partial y} = \rho \frac{\partial v}{\partial t} + \rho u \frac{\partial v}{\partial x} + \rho v \frac{\partial v}{\partial y} \quad (2.40)$$

Combining equations (2.38) to (2.40) and transforming them to generalized coordinates (ξ, η) results in the following normal momentum equation applied at the wall

$$(\eta_x \xi_x + \xi_y \eta_y) p_\xi + (\eta_x^2 + \eta_y^2) p_\eta = -\rho U (\eta_x u_\xi + \eta_y v_\xi) \quad (2.41)$$

The ξ derivatives are centered-differenced and the η derivatives use first-order one-sided differencing.

In the results presented here, the wall was assumed to be adiabatic and fully non-catalytic, which implies that the total enthalpy, h_0 , is constant, and that the normal gradient of each species mass fraction, c_i , is zero at the wall

$$\left(\frac{\partial c_i}{\partial n}\right)_{wall} = 0 \quad (2.42)$$

This equation can be written in a form similar to the normal momentum equation (equation (2.41))

$$(\eta_x \xi_x + \xi_y \eta_y) c_{i\xi} + (\eta_x^2 + \eta_y^2) c_{i\eta} = 0 \quad (2.43)$$

The gas temperature, T , at the wall is then obtained from the definition of total enthalpy

$$h_0 = \sum_{i=1}^n c_i \int^T c_{p_i} dT + \frac{1}{2}(u^2 + v^2) + \sum_{i=1}^n c_i h_i^0 \quad (2.44)$$

A Newton-Raphson iterative method is used to solve for T . The density, ρ , at the wall is obtained from the equation of state

$$\rho = \frac{p}{\sum_{i=1}^n \frac{c_i}{M_i} RT} \quad (2.45)$$

Finally, the species densities, ρ_i , at the wall are obtained from the relation

$$\rho_i = c_i \rho \quad (2.46)$$

Chapter 3

BENCHMARK TEST CASES

The performance and accuracy of the present TVD scheme is demonstrated by the examples presented in the following sections. Section 3.1, presents results for a nonreacting perfect gas, followed by a series of studies on real gas flows with a single-reaction chemistry model, which are presented in section 3.2.

3.1 Nonreacting, Perfect Gas Studies

In this section, a series of studies for a nonreacting perfect gas ($\gamma = 1.4$) is presented, and the results compared with analytic or other numerical results available. The studies were conducted for wedges and spheres.

3.1.1 Wedge at $M=10$

The first case considered, consists of a computation of the flowfield produced by a 15° half angle wedge moving at a Mach number $M = 10$. The wedge and associated coordinate system is shown in Fig. 3.1. The analytic solution for this problem can be obtained from the oblique shock relations (see for example Ref. 38). The exact analytic solution gives the following results:

Shock wave angle (measured from the wedge surface) $\beta_{shock} = 4.94^\circ$.
Dimensionless pressure $p/(\gamma p_\infty) = 9.57$.

The numerical results obtained with the present method for the wedge flow are presented in Fig. 3.2. The grid points are taken in a direction normal to the wedge surface. The first grid point (# 1) corresponds to the wedge surface, and each subsequent grid point corresponds to an angular increment $\Delta\beta = 0.25^\circ$. Note that the shock wave is captured in essentially two grid points with no oscillations. The numerical result is in excellent agreement with the analytic solution.

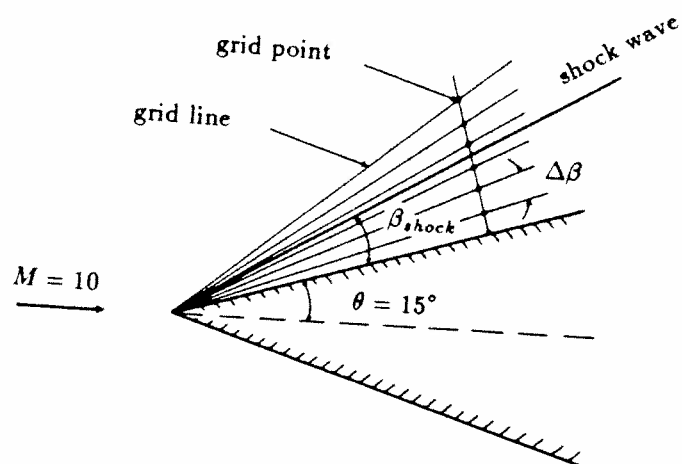


Figure 3.1: Wedge flow considered in section 3.1.1

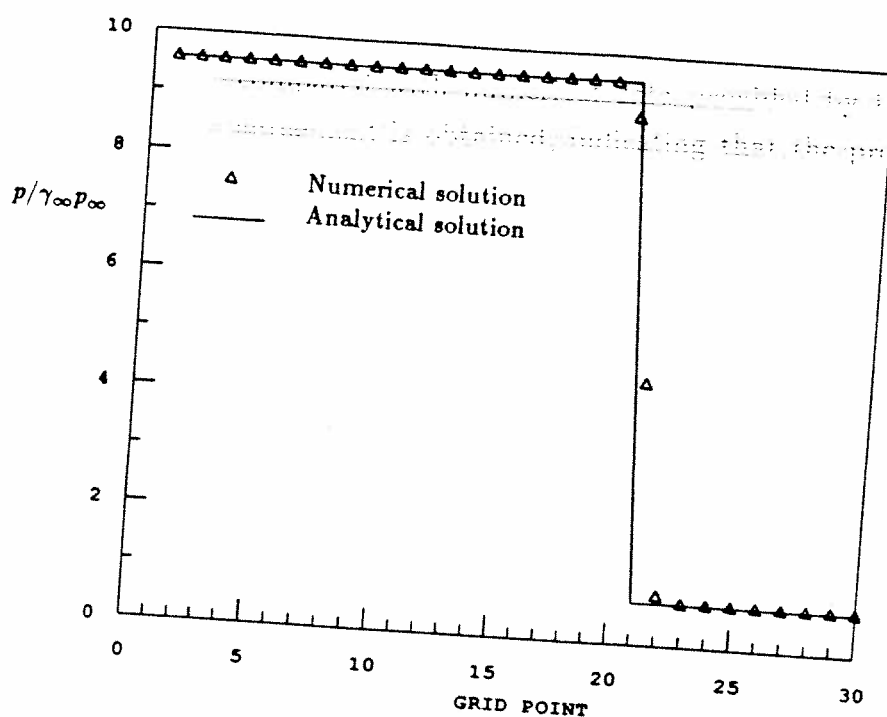


Figure 3.2: Nondimensional pressure results for a $M = 10$ wedge flow.

3.1.2 Sphere at $M=2.94$

A computation was performed of a $M = 2.94$ flow past a sphere. The results were then compared with numerical data provided by Chakravarthy et.al.³⁹, which used the SCM method to solve the Euler equations in nonconservative form. The bow shock shape produced by the sphere is shown in Fig. 3.3. The location of the shock wave obtained with the present method, was determined using a graphics package known as "plot3d". The surface pressure distribution is compared with the data provided by Chakravarthy et.al. in Fig. 3.4. Excellent agreement between the two methods is obtained for both the shock location and the surface pressure distribution.

3.1.3 Sphere at $M=20$

In order to assess the accuracy of the present method in the very high Mach number regime, a computation of a $M = 20$ flow past a sphere was performed. The bow shock shape obtained with the present method, shown in Fig. 3.5, was compared with numerical data provided by Lyubimov and Rusanov⁴⁰. Excellent agreement is obtained, indicating that the present method can accurately predict flow fields in this Mach number range.

3.2 Single-Reaction, Real Gas Studies

Before applying the present code to a case involving a complete reaction mechanism, a series of studies were conducted on real gas single-reaction flows. The main objective of these studies was to evaluate the performance of the code in reproducing the various chemical states that are possible in a given flow: frozen, nonequilibrium and equilibrium.

The case of single-reaction flow provides us also, with an opportunity to illustrate how the point implicit technique works for chemically reacting flows. This illustration will be presented in the following subsection, preceding the presentation of some of the results obtained for this type of flow.

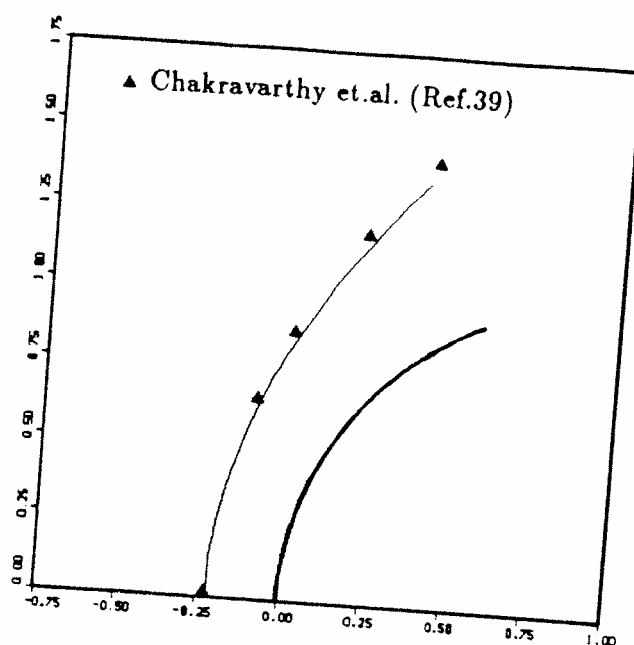


Figure 3.3: Sphere in supersonic flow, $M = 2.94$.

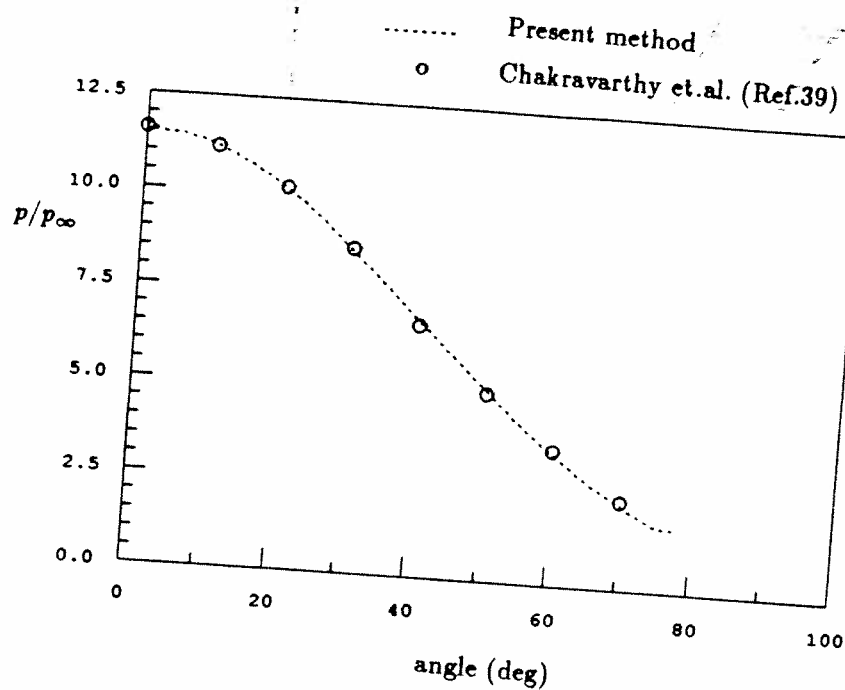


Figure 3.4: Surface pressure comparison for a sphere, $M = 2.94$

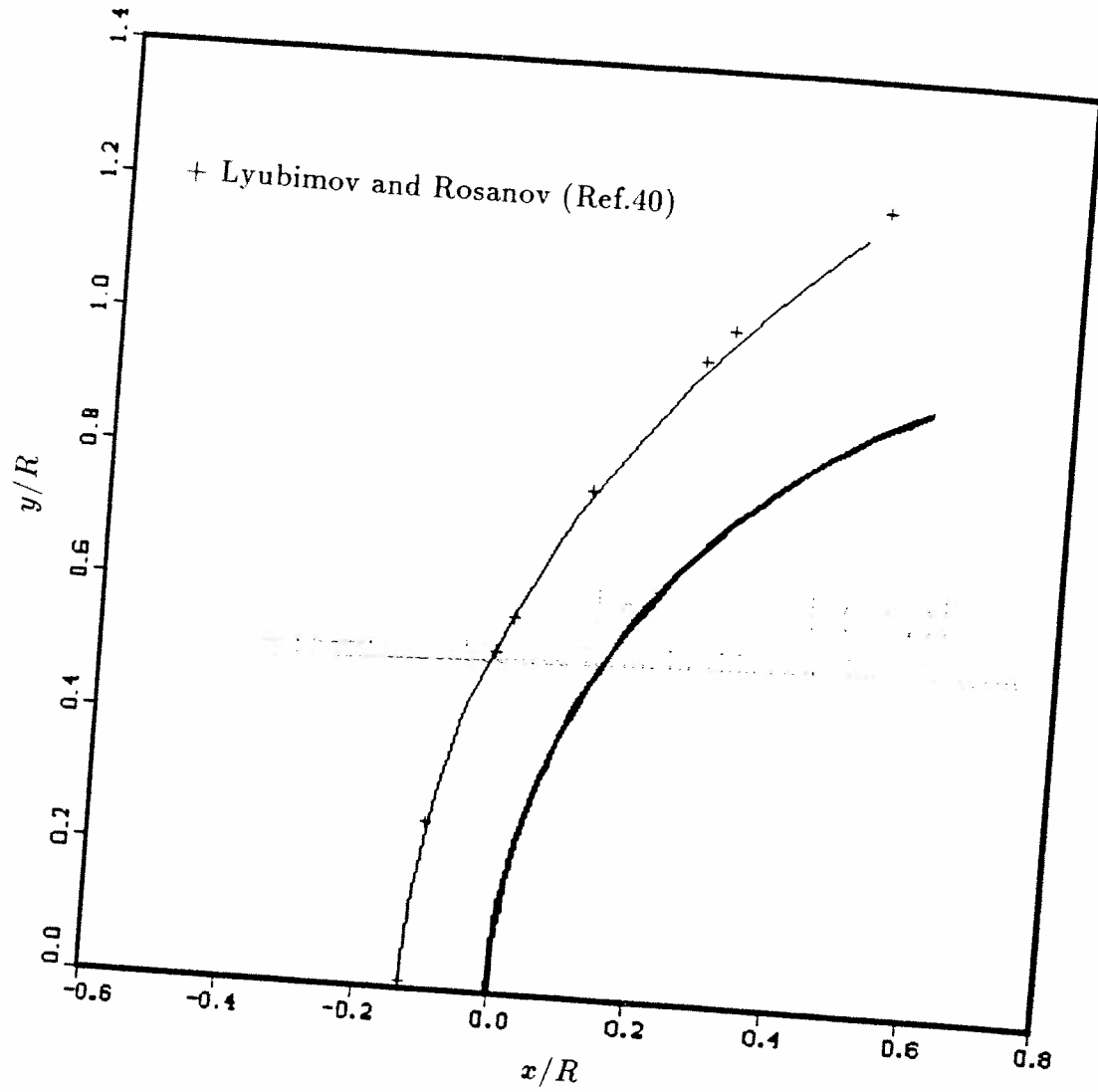


Figure 3.5: Sphere in hypersonic flow, $M = 20$.

3.2.1 Illustration of the Point Implicit Technique

In order to understand how the point implicit technique works, consider a one-dimensional compressible flow case for the O_2 dissociation reaction



For simplicity, only the forward reaction is considered, and the reaction rate is assumed to be constant. A similar case was considered by Bussing and Murman²⁸. The governing equations for this case are

$$\frac{\partial \mathbf{q}}{\partial t} + \frac{\partial \mathbf{F}}{\partial x} = \mathbf{W} \quad (3.2)$$

with

$$\mathbf{q} = \begin{bmatrix} \rho_1 \\ \rho_2 \\ \rho u \\ e \end{bmatrix} \quad \mathbf{F} = \begin{bmatrix} \rho_1 u \\ \rho_2 u \\ \rho u^2 + p \\ u(e + p) \end{bmatrix} \quad \mathbf{W} = \begin{bmatrix} w_1 \\ -w_1 \\ 0 \\ 0 \end{bmatrix} \quad (3.3)$$

The chemical source term, in this case, has the form

$$w_1 = -k_f \rho_1 \quad (\rho_1 = \rho_{O_2}) \quad (3.4)$$

The characteristic chemical time is defined as

$$\tau_{ch} = \frac{1}{k_f} = \frac{-1}{\frac{\partial w_1}{\partial \rho_1}} \quad (3.5)$$

Consider only the predictor step. The scaling matrix defined in equation 2.21 becomes

$$D = \begin{bmatrix} 1 - \Delta t \frac{\partial w_1}{\partial \rho_1} & 0 & 0 & 0 \\ \Delta t \frac{\partial w_1}{\partial \rho_1} & 1 & 0 & 0 \\ 0 & 0 & 1 & 0 \\ 0 & 0 & 0 & 1 \end{bmatrix} \quad (3.6)$$

The predictor step for the momentum (q_3) gives from equation (2.32)

$$\Delta q_3 = -\Delta t (F_j - F_{j-1}) \quad (3.7)$$

Δt is usually limited by the CFL stability condition³⁴ giving

$$\Delta t = \frac{\Delta x}{|u + a|} \equiv \tau_f \quad (3.8)$$

where a is the speed of sound. Assume for simplicity that $\Delta x = 1$, then the predictor step for specie 1 (q_1) gives from equation (2.33)

$$(1 - \Delta t \frac{\partial w_1}{\partial \rho_1}) \Delta q_1 = -\Delta t (F_j - F_{j-1}) + \Delta t w_1 \quad (3.9)$$

Noting that $\tau_f = \Delta t$, we obtain

$$\Delta q_1 = -\frac{\tau_f}{1 + \frac{\tau_f}{\tau_{ch}}} (F_j - F_{j-1} - w_1) \quad (3.10)$$

For $\tau_f \gg \tau_{ch}$, i.e., the equations are stiff, we obtain from equations (3.7) and (3.10) the following expressions

$$\Delta q_3 = -\tau_f (F_j - F_{j-1}) \quad (3.11)$$

and

$$\Delta q_1 = -\tau_{ch} (F_j - F_{j-1} - w_1) \quad (3.12)$$

It can be seen that, for this example, the "fluid dynamic" variables are advanced using a time step τ_f , and the "chemical variables" are advanced using τ_{ch} . Interestingly, the second specie is calculated by the following scheme:

$$\Delta \rho_2 = \Delta \rho - \Delta \rho_1 \quad (3.13)$$

$$= \tau_f \left(\frac{\partial \rho}{\partial t} \right) - \tau_{ch} \left(\frac{\partial \rho_1}{\partial t} \right) \quad (3.14)$$

$$= \tau_f [-(\rho u)_j + (\rho u)_{j-1}] + \tau_{ch} [(\rho_1 u)_j - (\rho_1 u)_{j-1} - w_1] \quad (3.15)$$

Thus, in general, the point implicit technique advances each state quantity at its own characteristic rate.

3.2.2 Wedge at $M=7$

In this section, we will calculate the nonequilibrium flow over a 30° half angle wedge, assuming that the flowing gas consists of pure oxygen, and assuming also

Table 3.1: Rate coefficients for oxygen reaction

	Forward reaction	Backward reaction
A	3.6×10^{18}	3.0×10^{15}
b	-1	-0.5
C	5.95×10^4	0

that a single chemical reaction (forward and backward) is significant.



The forward and backward reaction rate constants are given by

$$K = AT^b e^{C/T} \quad (3.17)$$

The rate coefficients A, b, C used in the computations are given in Table 3.1.

The wedge and associated coordinate system is shown in Fig. 3.6. A characteristic convection time τ_f can be defined as

$$\tau_f = \frac{L}{u} \quad (3.18)$$

A characteristic chemical time τ_{ch} can be defined as in Vincenti & Kruger¹⁷

$$\tau_{ch} = -1 / \left(\frac{\partial w}{\partial \alpha} \right)_{\rho, T} \quad (3.19)$$

where α is the degree of dissociation. For the present case, the chemical source term w , is given by

$$w(\rho, \alpha, T) = \frac{\rho K_f}{2M_O} [(1 - \alpha)^2 - \frac{2\rho}{M_O K_c} \alpha^2 (1 - \alpha)] \quad (3.20)$$

where $K_c = K_f/K_b$ and M_O is the molecular weight of atomic oxygen.

Figure 3.7 shows pressure distributions as a function of vertical distance normal to the surface, for a $M = 7$ flow past the 30° half angle wedge. Results are presented

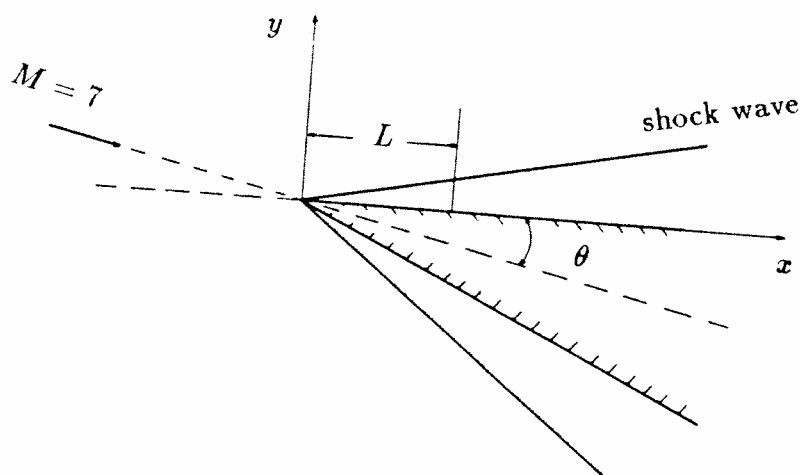


Figure 3.6: Wedge flow considered in section 3.2.2

at three different values of L (see Fig 3.6): $L = 0.01$, $L = 1$ and $L = 100$ cm, with corresponding Damköhler numbers, Da , of 0.01, 1 and 100 respectively. The free stream conditions are: $p_\infty = 1$ atm., and $T_\infty = 2000$ °K. The high free stream temperature was used in order to obtain significant dissociation. For this problem, an analytic solution can be found for the frozen and equilibrium flow cases. These solutions are also plotted in Fig. 3.7. At large distances, L , from the wedge apex (i.e., high Damköhler numbers) the pressure distribution and shock wave angle should approach the equilibrium values. At short distances (i.e., low Damköhler numbers), the solution must approach the frozen flow case. This is clearly shown in Fig. 3.7. Also note that $(y/L)_{shock} = \tan(\beta_{shock})$, and that the shock wave is curved. The shock wave angle, β_{shock} decreases with distance along the wedge. The shock wave angle varies from its frozen value $(\beta_{shock})_{fr} = 36.8^\circ$ to its equilibrium value $(\beta_{shock})_{eq} = 34.9^\circ$. Fig. 3.8 shows the degree of dissociation α . Note that for the $Da = 0.01$ case, the flow is not completely frozen and there is some dissociation. The slight dissociation causes the shock to move closer to the body and, for this reason, the computed shock wave angle in this case is slightly less than the analytic frozen value. The calculated results for the $Da = 100$ case are in close agreement with the analytic equilibrium solution.

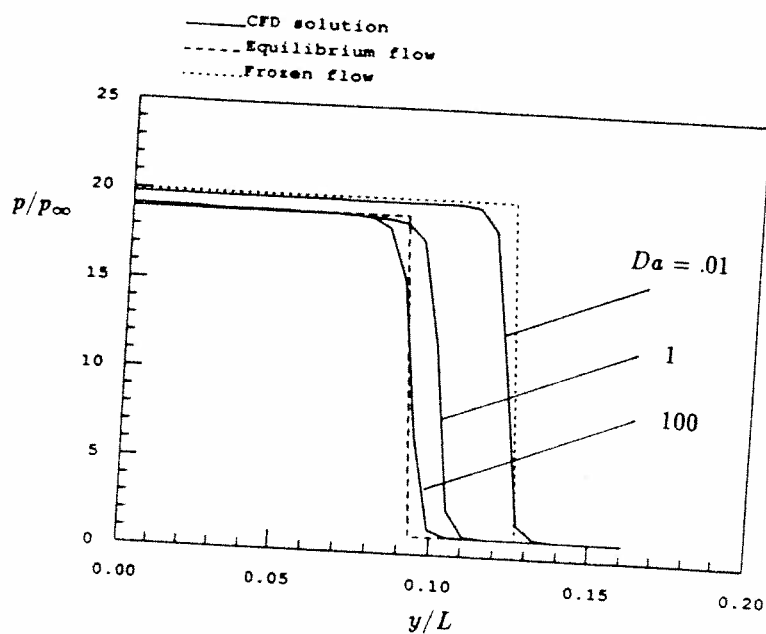


Figure 3.7: Nondimensional pressure results for a $M = 7$ wedge flow with oxygen dissociation.

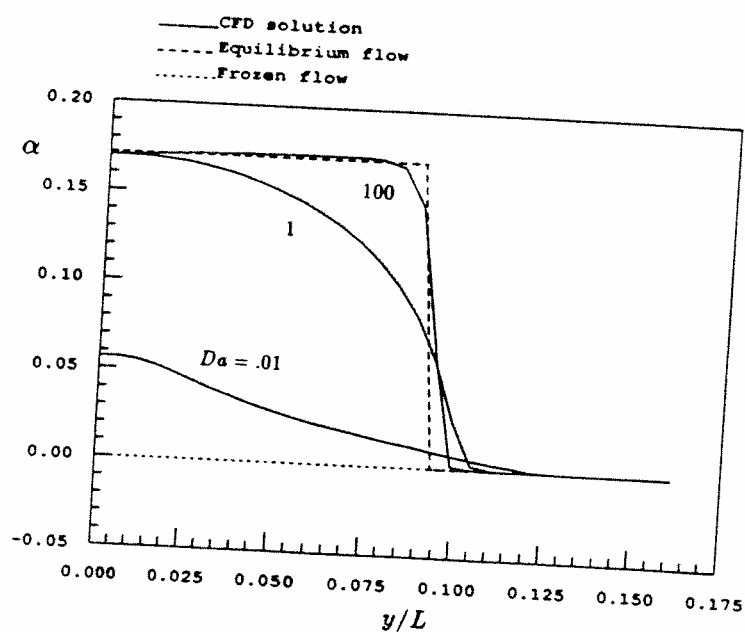


Figure 3.8: Degree of dissociation for a $M = 7$ wedge flow with oxygen dissociation.

3.2.3 Spheres at $M=6$

Calculations with the gas model described above were conducted also for a sphere moving at $M = 6$. The free stream temperature T_∞ was taken to be $800^\circ K$ in this case. Fig. 3.9 shows the nondimensional temperature distribution along the stagnation streamline for five different values of the sphere radius. Fig. 3.10 shows the degree of dissociation for the same five cases. Note that for sphere radii of 1, 10 and 100 cm, the degree of dissociation and the temperature at the stagnation point ($x/R = 0$) are identical, indicating that the flow has reached equilibrium conditions there. For the smaller radii less dissociation is obtained, resulting in higher stagnation temperatures. The $R = 0.001$ case resulted in nearly frozen flow. Note also from Fig. 3.9 that the shock wave location moves closer to the body (i.e. x/R decreases) as more oxygen is dissociated. This is generally true for endothermic chemical reactions. For the case of exothermic reactions as in combustion problems the opposite effect is observed, that is, the shock wave moves away from the body. This effect can be observed in the cases that will be presented in the next chapter for exothermic blunt body flows.

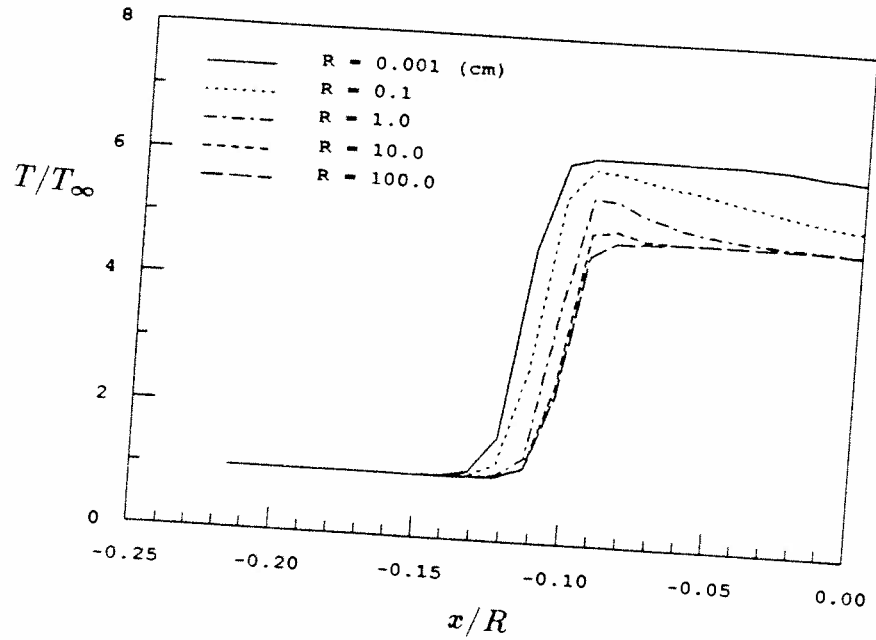


Figure 3.9: Temperature variation along the stagnation streamline for a $M = 6$ sphere flow with oxygen dissociation.

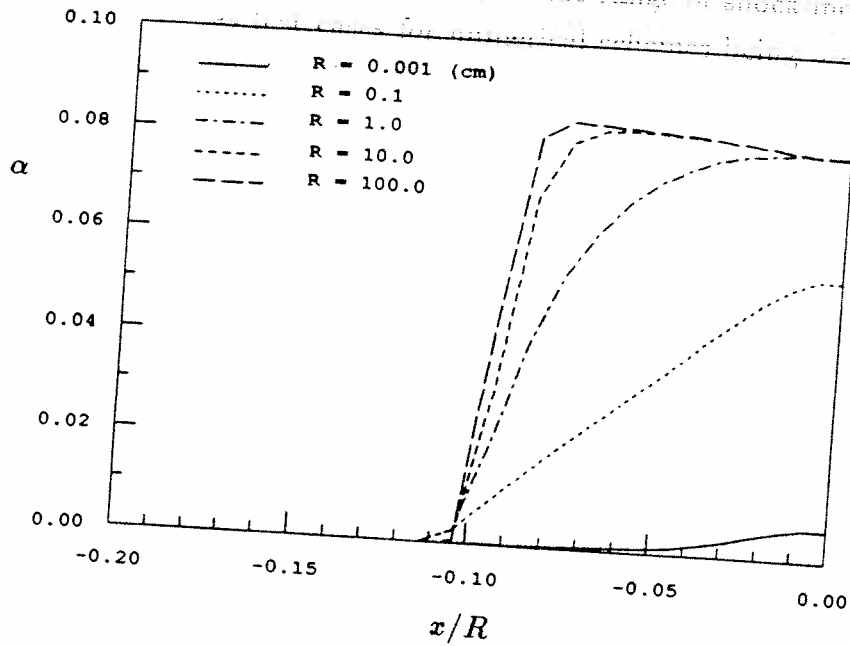


Figure 3.10: Degree of dissociation along the stagnation streamline for a $M = 6$ sphere flow with oxygen dissociation.

Chapter 4

EXOTHERMIC BLUNT BODY FLOW

In Chapter 1, we mentioned several shock-induced combustion modes that can be established in a ram accelerator. These modes include coupled or decoupled shock-deflagration systems, and detonation waves. Such shock-induced combustion phenomena, ranging from decoupled shock-deflagration systems to overdriven detonation waves, were experimentally investigated in the mid 1960's^{41,42} and early 1970's, most notably by a group of researchers at the Institut Franco-Allemand de Recherches de Saint-Louis^{43,44}. Their experiments consisted of firing, among others, spherical projectiles through explosive mixtures of H_2/O_2 and H_2/air . These experiments, covering a wide range of shock-induced combustion modes, can be used as test cases for numerical schemes being used to calculate hypersonic chemically reacting flows.

In this chapter, numerical simulations of exothermic blunt body flows are presented and compared with the experimental results mentioned above. These results are the first computations that have successfully reproduced the various combustion regimes observed in the exothermic blunt body flow experiments conducted at the Institut Franco-Allemand de Recherches de Saint-Louis^{43,44}.

The calculations were carried out for a spherical projectile having a diameter of 15 mm, moving through stoichiometric mixtures (equivalence ratio $\phi = 1$) of H_2/O_2 and H_2/air at pressures of 186 and 320 torr, respectively for each mixture. Four cases are considered. Two of them are for projectile speeds, U_1 , below the Chapman-Jouguet (C-J) detonation speed, D , of the mixture (subdetonative speed), and two cases are presented for superdetonative speeds. The experimental data for the four cases considered are summarized in Table 4.1. The computations of the $M = 3.55$, $M = 5.08$ and $M = 6.46$ cases were carried out on a 42×44 orthogonal grid. The $M = 4.18$ case was computed on a 32×32 grid.

Table 4.1: Experimental data on the exothermic blunt body flows

Fig.	mixture	p torr	speed of sound m/sec	D^\dagger m/sec	U_1 m/sec	M
4.1	$2H_2 + O_2$	186	533	2550	1892	3.55
4.4	$2H_2 + O_2 + 3.76N_2$	320	403	2055	1685	4.18
4.7	$2H_2 + O_2$	186	533	2550	2705	5.08
4.10	$2H_2 + O_2 + 3.76N_2$	320	403	2055	2605	6.46

[†]measured detonation speed (Ref. 44)

4.1 Subdetonative speeds

Figure 4.1, obtained from the work of H. Lehr⁴⁴, shows a picture of a spherical projectile flying through a stoichiometric mixture of H_2/O_2 at a speed $U_1 = 1892$ m/s ($M = 3.55$)[†]. This case produced a decoupled shock-deflagration system, in which the combustion front is separated from the shock wave by an induction zone. Figure 4.2 shows the computational results, obtained by using the present numerical scheme, for the same flight conditions. The numerical calculation shown in Fig. 4.2, which consists of nondimensional temperature contours, successfully reproduced the decoupled shock-deflagration system. The shock wave, induction zone and combustion front can be clearly identified. The experimental shock location, taken from Fig. 4.1, is also shown for comparison. Very good agreement between the computed and the experimentally observed shock location is obtained.

The distribution of physical quantities on the stagnation line is shown in Fig. 4.3. Three zones can be observed in the combustion process, following the initial rise in pressure, temperature and density across the shock wave:

- 1) An induction zone, in which the temperature remains practically constant and the mole fractions of H , O , OH and H_2O increase by several orders of magnitude. In the semilogarithmic plot of mole fractions vs nondimensional distance, the curves

[†]The pictures of the experiments were taken with a shadow technique

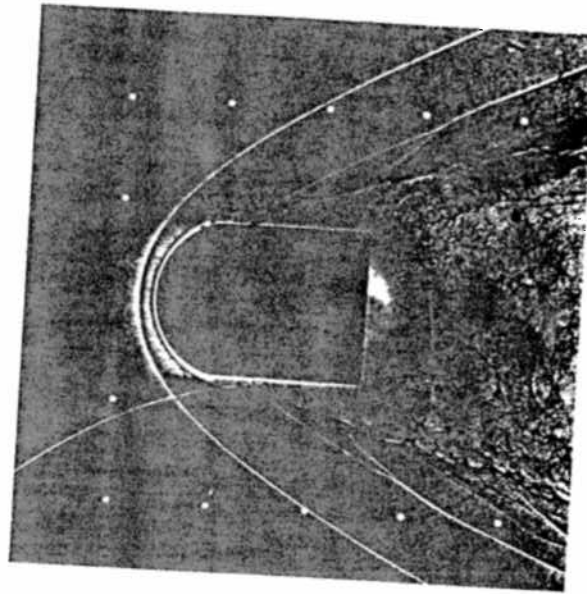


Figure 4.1: Shock wave and combustion front in a stoichiometric H_2/O_2 mixture at $M=3.55$ (from Ref. 44)

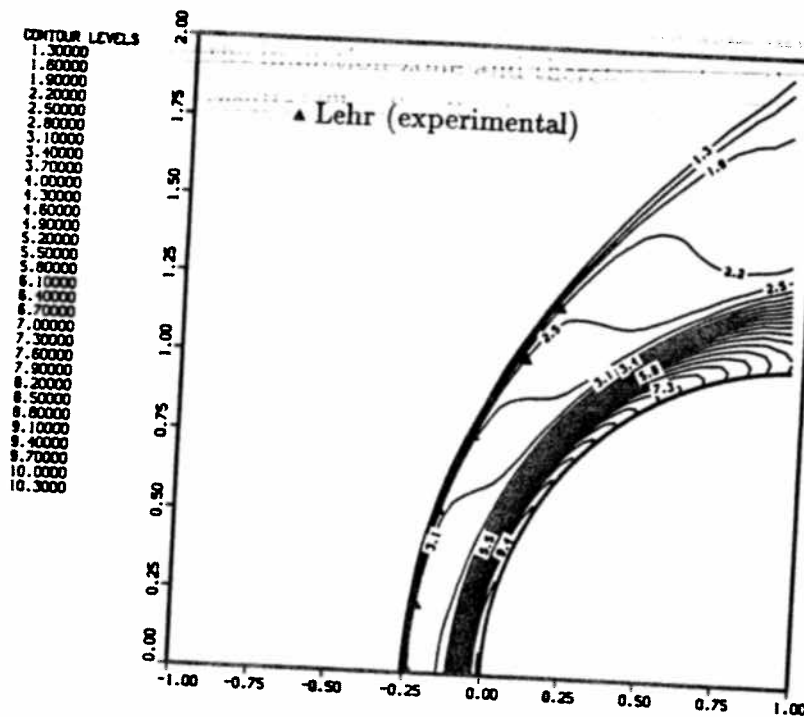


Figure 4.2: Temperature contours (T/T_∞) for stoichiometric H_2/O_2 , $M=3.55$ flow past a sphere. Experimental shock location obtained from Fig. 4.1.

are straight lines. The pressure and density increase slightly in this zone.

2) A reaction zone (also referred to as the "combustion front" in the present work), in which the temperature rises very steeply and the rate of change of the mole fractions diminishes (in particular, the mole fraction of atomic hydrogen reaches a maximum). The pressure distribution is nearly unaffected by the heat release and as a result, the change in density must be opposite to that of temperature in this zone.

3) A final zone, in which the temperature still increases and the density diminishes, but more and more slowly, and the species mole fractions, as well as all the other variables, approach their equilibrium values asymptotically.

Figures 4.4 and 4.5 show the results for the H_2/air mixture for a speed of $U_1 = 1685$ m/s ($M = 4.18$). The predicted shock location is slightly farther out from the body than the experimental location, probably due to a slightly thicker computed combustion zone. The additional heat release predicted between the shock wave and the body has the effect of pushing the shock away from the body. The inclusion of at least some of the endothermic reactions involving N_2 , which would tend to increase the induction zone and therefore reduce the combustion zone, would produce better results. The distribution of the physical quantities shown in Fig. 4.6 shows the same trend as for the H_2/O_2 mixture except that less chemical energy per unit mass is being released resulting in smaller variations in temperature and density behind the shock.

4.2 Superdetonative speeds

When the body is flying at superdetonative speeds, i.e., speeds above the detonation speed of the mixture, a coupled shock and combustion front is formed, whose structure depends on the mixture (and pressure). Figures 4.7 and 4.8 show the experimental and numerical results, respectively, for the H_2/O_2 mixture at a projectile speed $U_1 = 2705$ m/s ($M=5.08$). A combination of overdriven and oblique detonation waves is obtained. Although the detailed structure of the detonation cannot be resolved, the overall effects, such as the location of the overdriven portion of the detonation wave and the angle of the oblique portion, are in close agreement with the experiment.

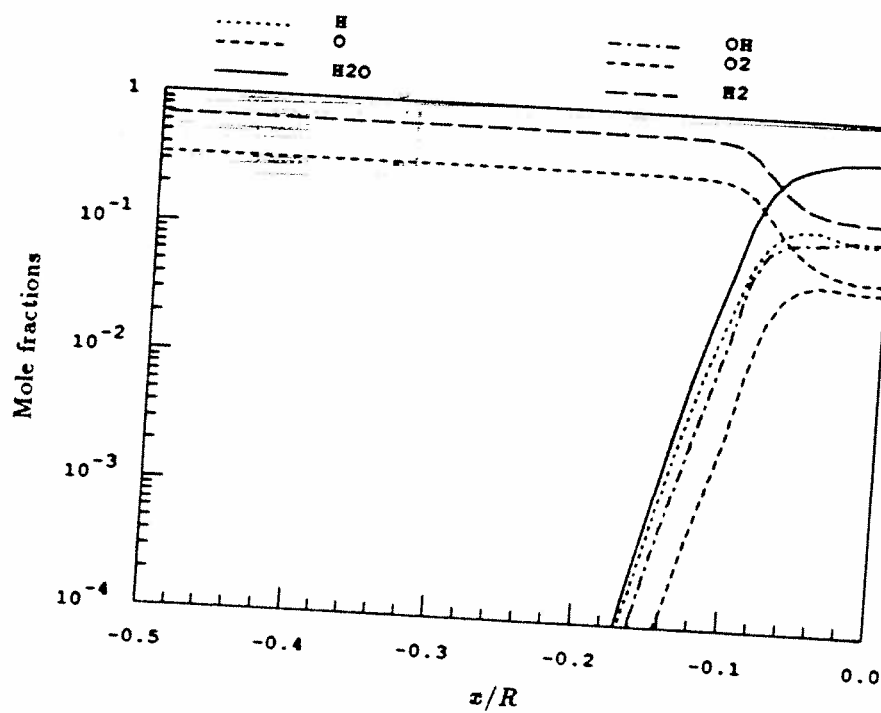
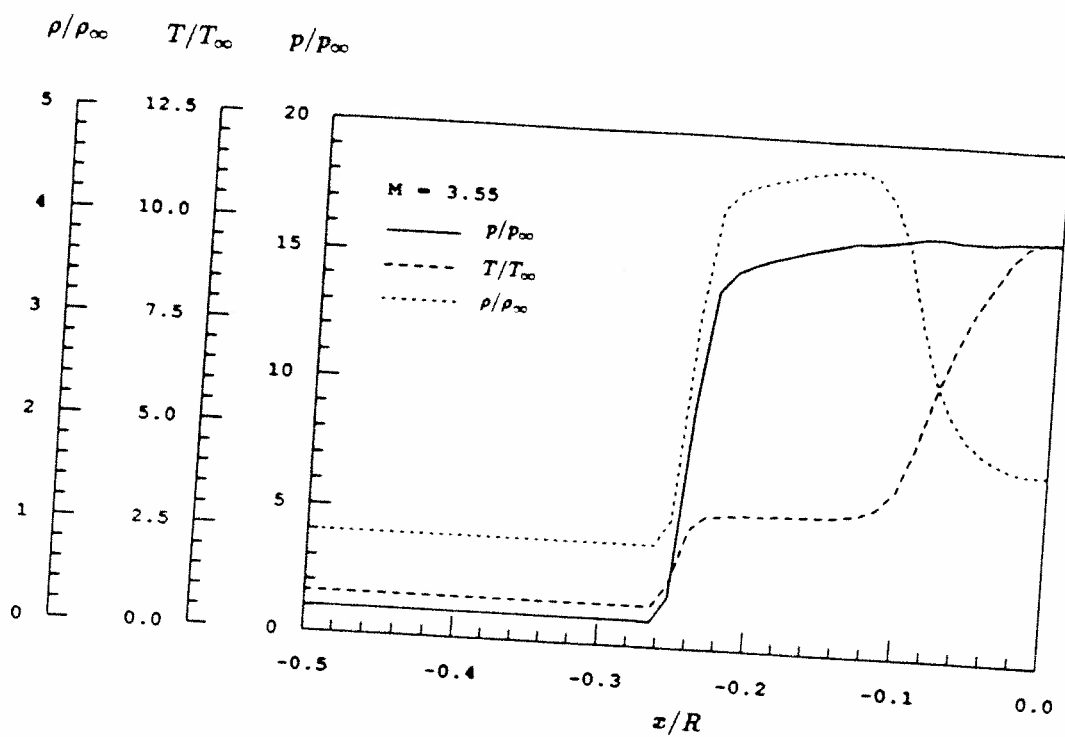


Figure 4.3: Distribution of physical quantities along the stagnation streamline for the $M = 3.55$ case.

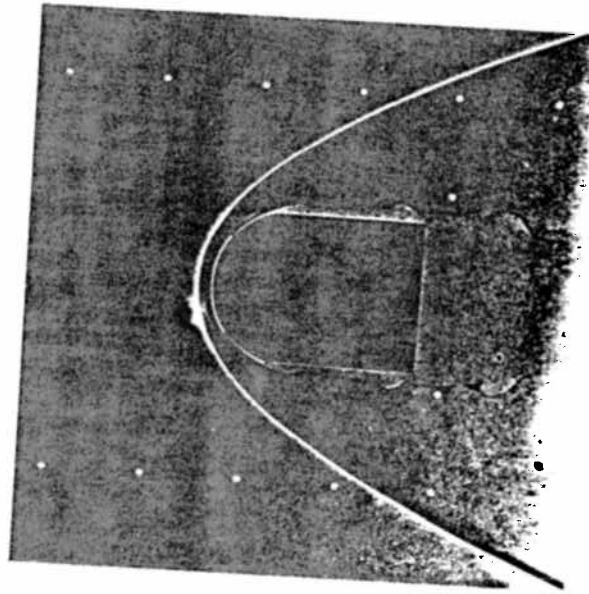


Figure 4.4: Shock wave and combustion front in a stoichiometric H_2/air mixture at $M=4.18$ (from Ref. 44)

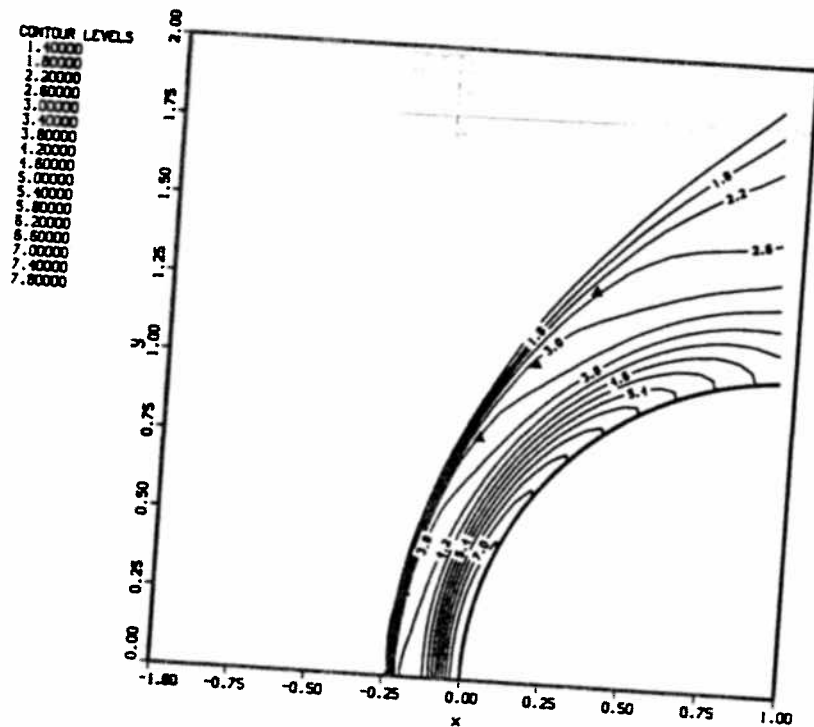


Figure 4.5: Temperature contours (T/T_∞) for stoichiometric H_2/air , $M=4.18$ flow past a sphere. Experimental shock location obtained from Fig. 4.4.

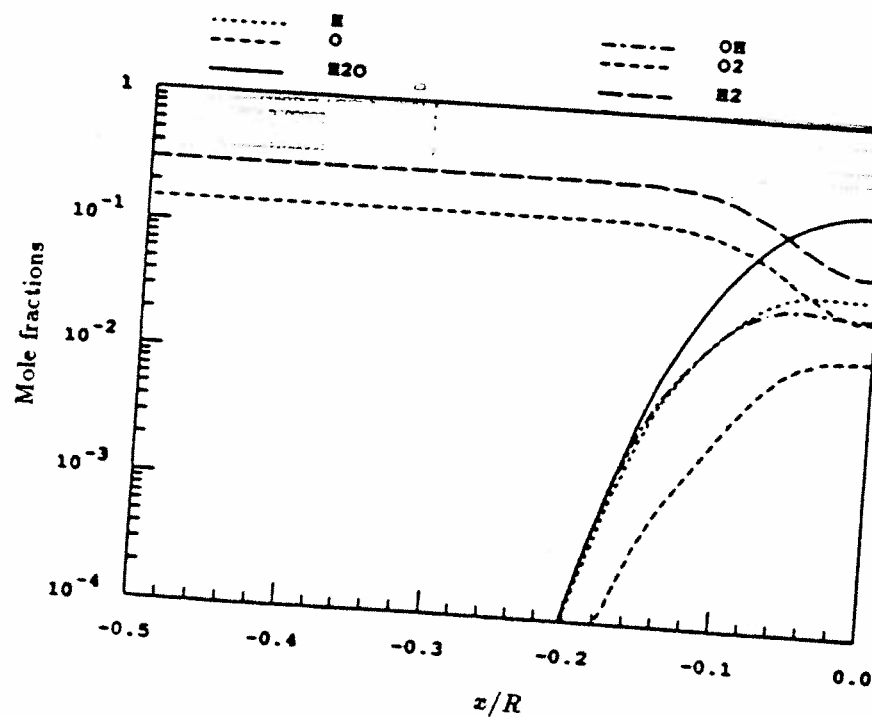
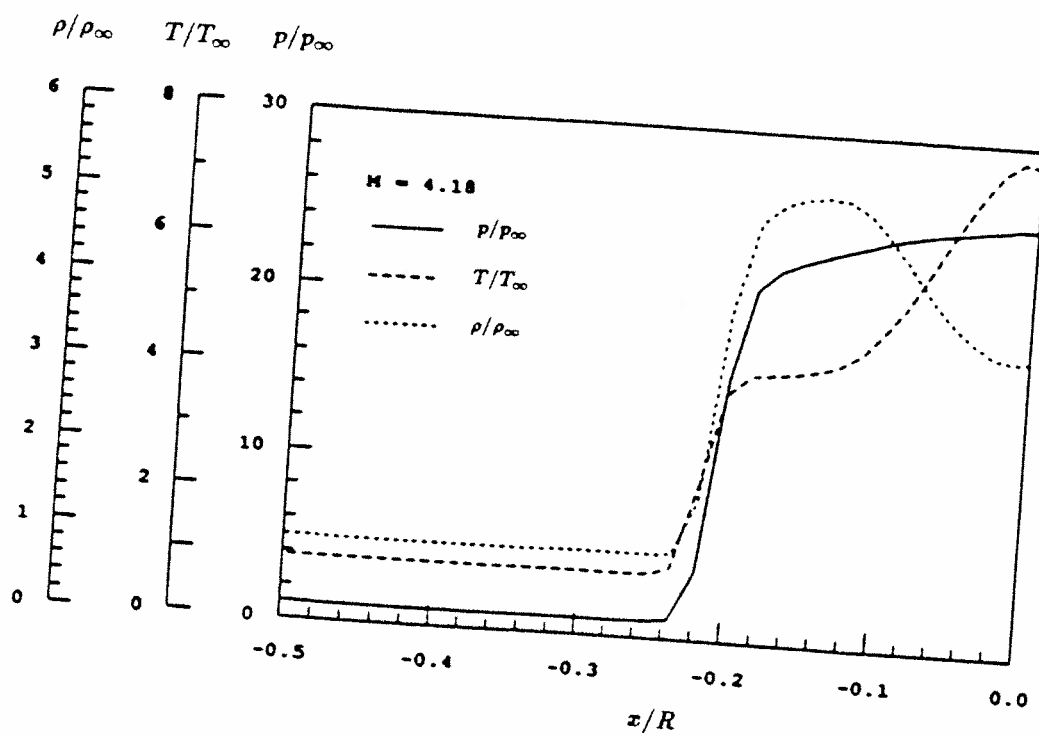


Figure 4.6: Distribution of physical quantities along the stagnation streamline for the $M = 4.18$ case.

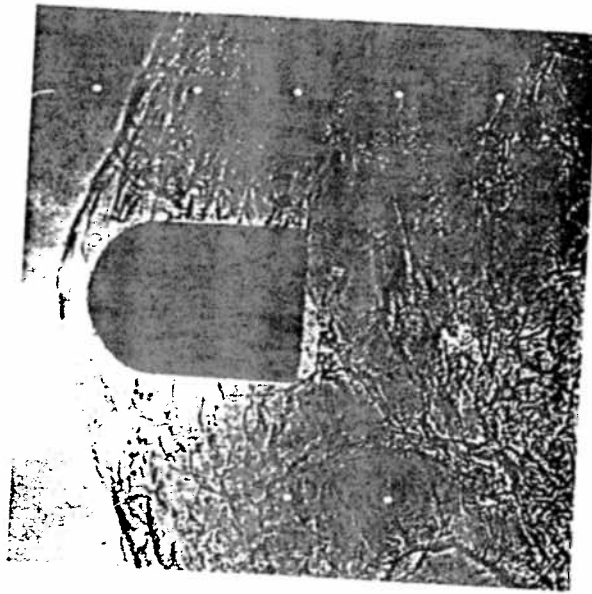


Figure 4.7: Overdriven detonation and oblique Chapman-Jouguet detonation in a stoichiometric H_2/O_2 mixture at $M=5.08$ (from Ref. 44)

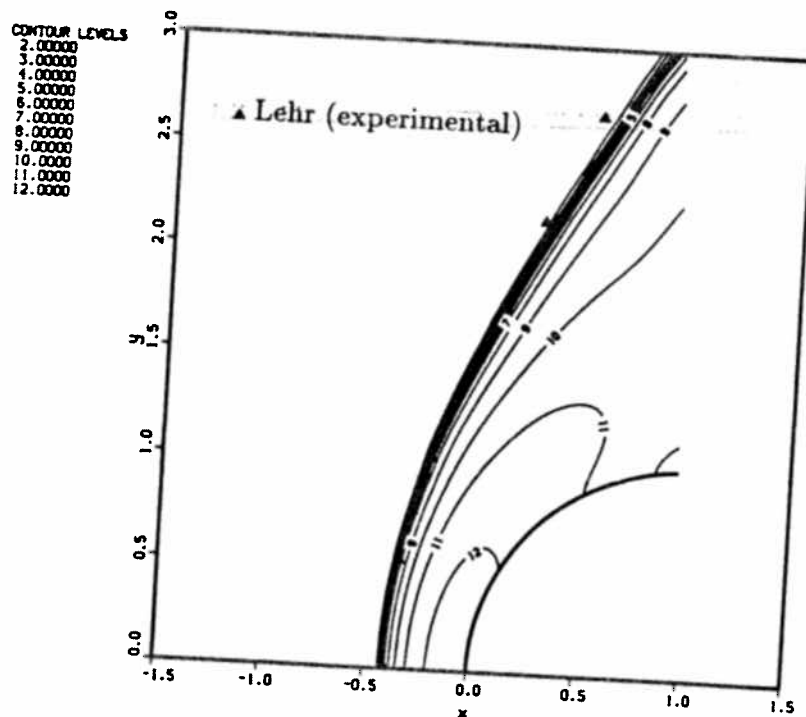


Figure 4.8: Temperature contours (T/T_∞) for stoichiometric H_2/O_2 , $M=5.08$ flow past a sphere. Experimental shock location obtained from Fig. 4.7.

The temperature plot shown in Fig. 4.9 shows that the heat release occurs immediately behind the shock. It is interesting to observe that the pressure plot exhibits a von Neumann spike not observed in nonreacting flows. Fujiwara et.al.⁴⁵, using a two-step reaction model (Korobeinikov model) and assuming constant γ , observed similar von Neumann spikes in their study of detonations supported by a blunt body. The mole fraction plot in Fig. 4.9 shows that the chemical reactions occur in a much shorter region as compared to the $M = 3.55$ (Fig. 4.3) or $M = 4.18$ (Fig. 4.6) cases.

Figures 4.10, 4.11 and 4.12 show the results for the H_2 /air mixture. The projectile speed is $U_1 = 2605$ m/s ($M=6.46$). In this case, the energy release is not high enough to initiate a detonation resulting in a coupled shock-deflagration wave. This fact is also reflected in the numerical calculation. Due to the smaller ratio of chemical energy to kinetic energy, the influence of heat release on the flow is not as strong as for the previous case. This can be seen by comparing Figs. 4.9 and 4.12. For the same reason, the von Neumann spike is not observed in this case. The shock is closer to the body for this same reason.

4.3 Comparison with F3d/Chem code

Recently, Lee and Deiwert⁴⁶ conducted a numerical calculation of the $M = 6.46$ case shown in Fig. 4.10 with the F3d/Chem code. Their code uses an implicit flux vector splitting method with upwind differencing in the streamwise direction and central differencing in the crossflow directions. The chemistry model and the rate coefficients used by Lee and Deiwert are the same as in the present study. Their calculations were made for inviscid flow and utilized a 57×41 grid.

Figures 4.13 and 4.14 show plots of the temperature distribution computed by the present method and by the method of Lee and Deiwert, respectively. The two results are in very good agreement.

The studies presented in this Chapter have provided the means for assessing the accuracy of the numerical scheme. The benchmark computations presented are in good agreement with the experimental results of Lehr and with the numerical results of Lee and Deiwert. Extension to ram accelerator configurations can thus be carried out with confidence. These are presented in Chapter 5.

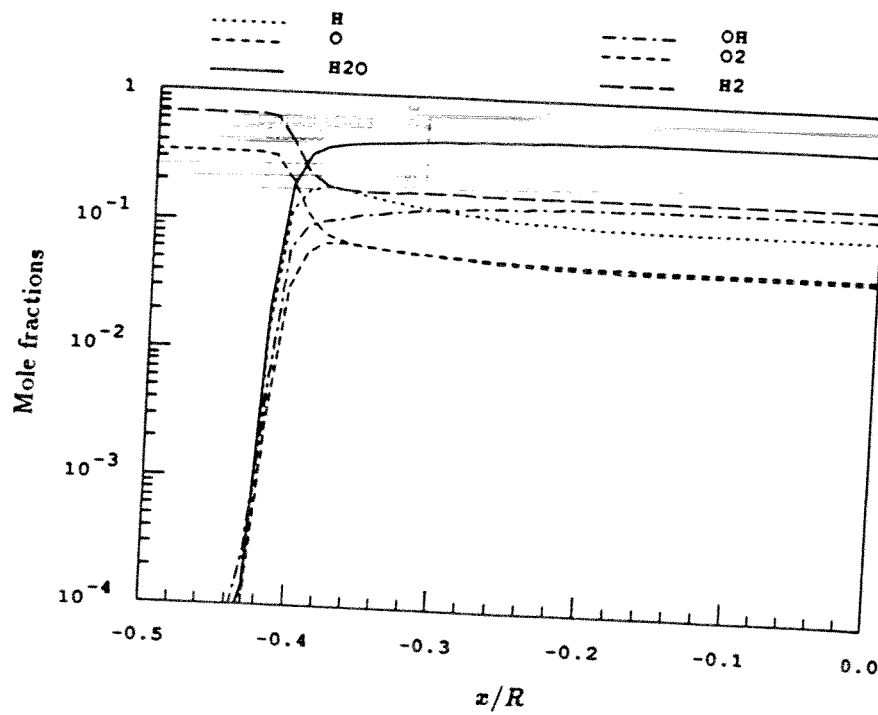
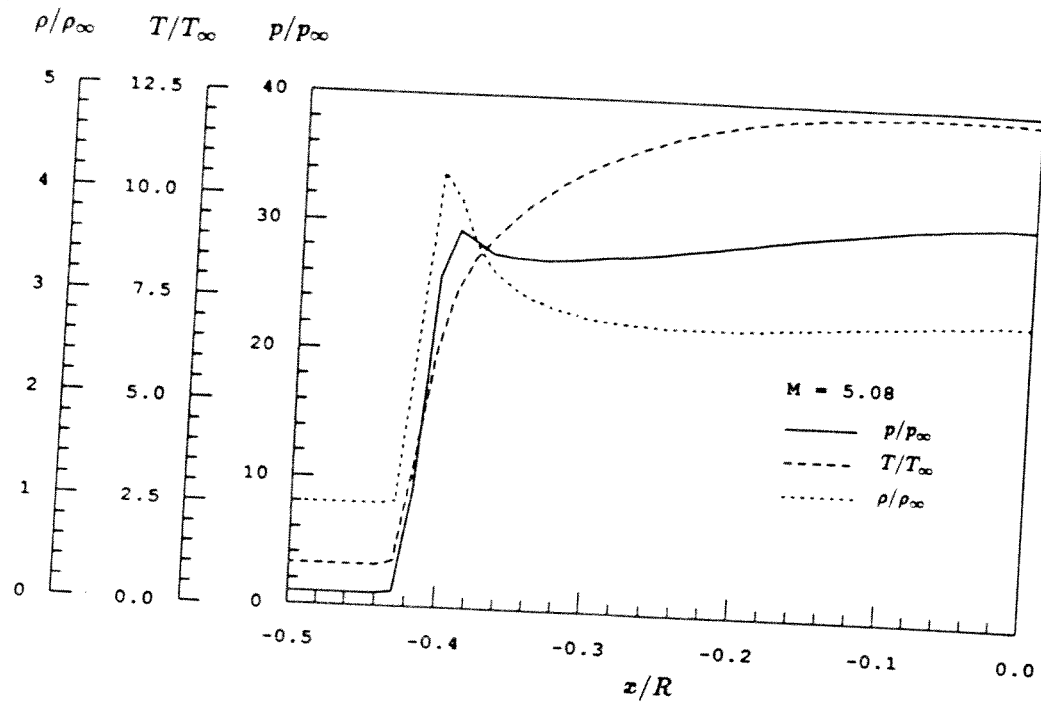


Figure 4.9: Distribution of physical quantities along the stagnation streamline for the $M = 5.08$ case.

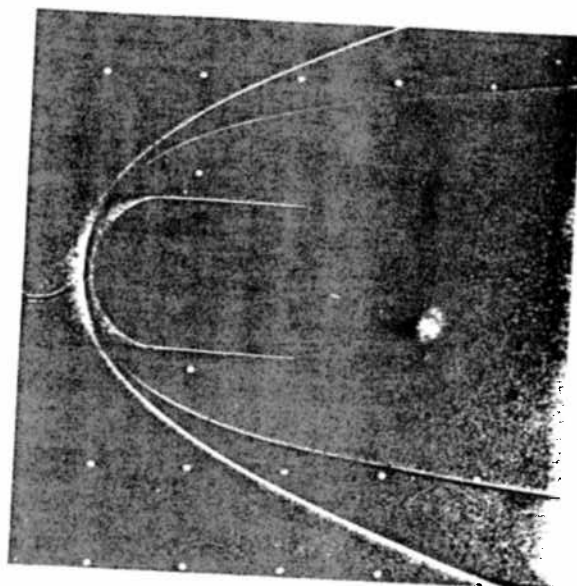


Figure 4.10: Shock-deflagration system in a stoichiometric H_2/air mixture at $M=6.46$ (from Ref. 44)

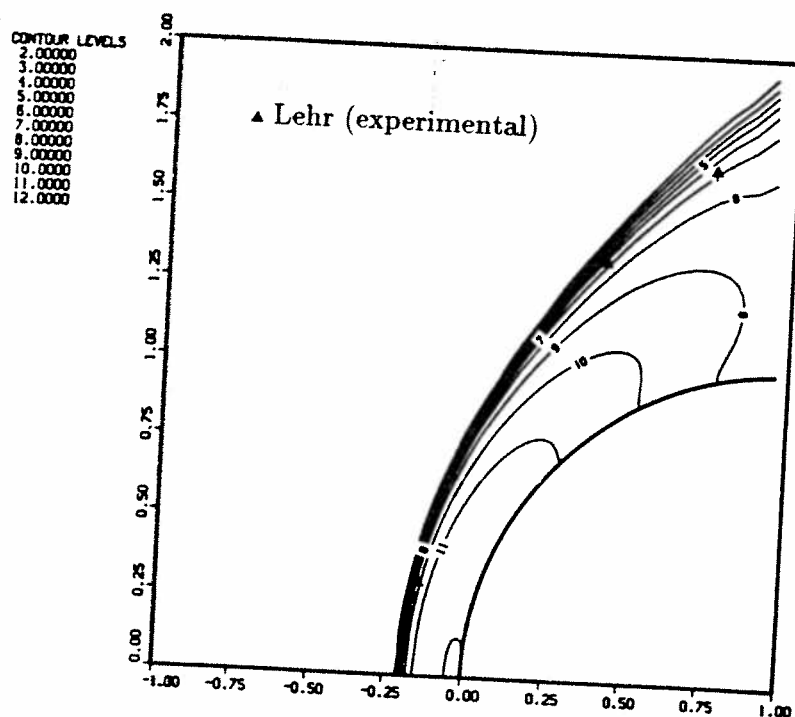


Figure 4.11: Temperature contours (T/T_∞) for stoichiometric H_2/air , $M=6.46$ flow past a sphere. Experimental shock location obtained from Fig. 4.10.

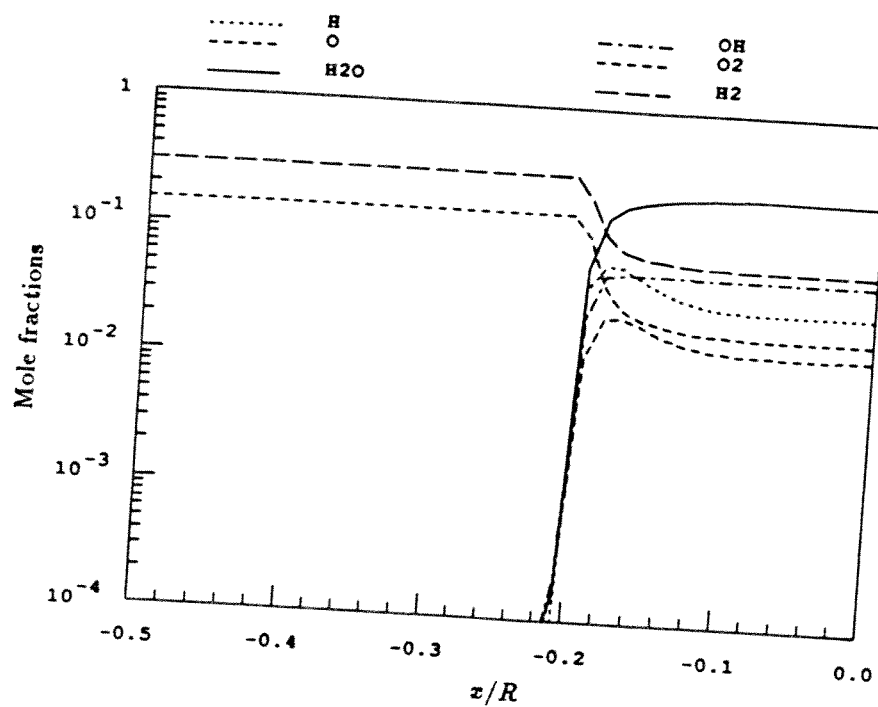
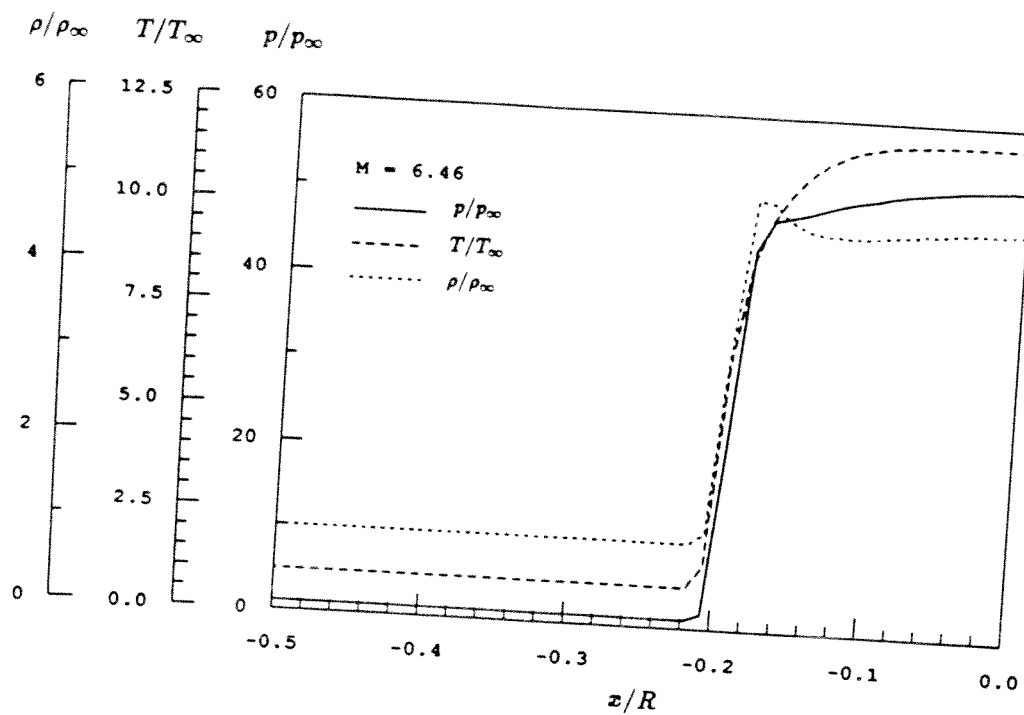


Figure 4.12: Distribution of physical quantities along the stagnation streamline for the $M = 6.46$ case.

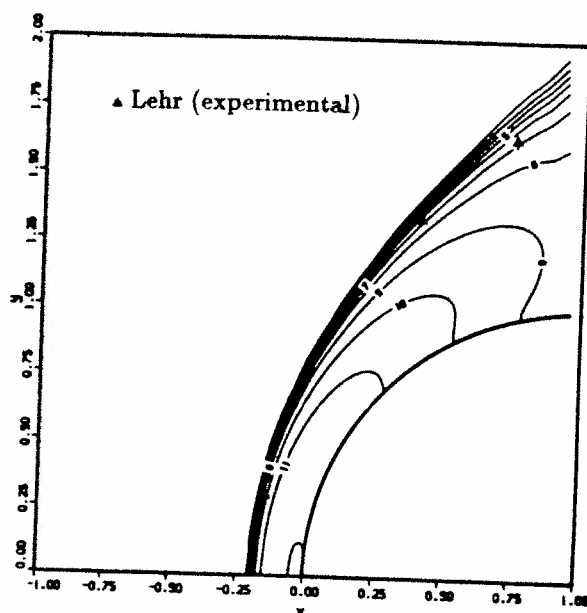


Figure 4.13: Temperature contours (T/T_∞) for stoichiometric H_2/air , $M=6.46$ flow past a sphere. Present method.

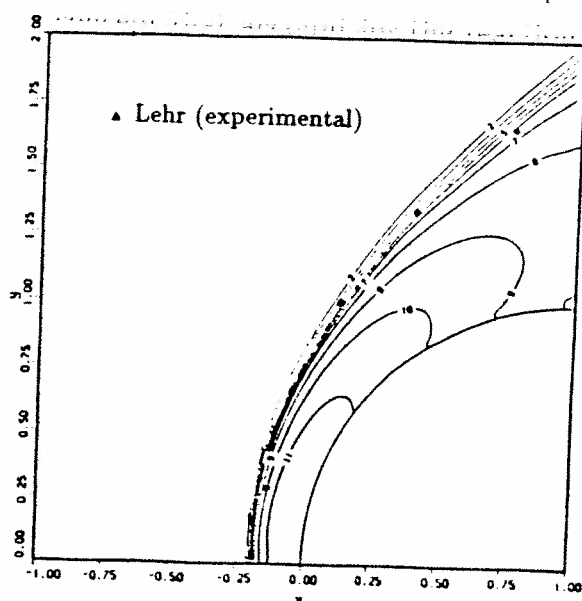


Figure 4.14: Temperature contours (T/T_∞) for stoichiometric H_2/air , $M=6.46$ flow past a sphere. Lee and Deiwert's method.⁴⁶

Chapter 5

RAM ACCELERATOR STUDIES

In this Chapter, the CFD code described previously is used to analyze the performance of various ram accelerator configurations in the superdetonative velocity range of 5.0 to 10.0 km/s. Also, a numerical investigation of the effects of nose blunting on the flow and combustion processes in the ram accelerator is presented.

These results do not represent a complete parametric study of the ram accelerator. The main purpose of these studies is to indicate general performance trends, and to analyze the effects that the different parameters, such as Mach number, projectile shape, projectile-to-wall area ratio, and gas mixture, have on the flow, combustion, and performance characteristics of the ram accelerator.

As was previously mentioned in the introduction, the results to be presented in this chapter represent the first computations ever conducted on the ram accelerator concept that account for the reaction kinetics of a complete combustion model.

Most of the calculations associated with the ram accelerator configuration are carried out on a 125×21 patched grid. A typical grid is shown in Fig. 5.1, where the plot has been magnified by a factor of 5 in the vertical direction for clarity. The same projectile configuration on a 1:1 scale is shown in Fig. 5.2. The free stream temperature, T_∞ , for all the cases presented in this chapter was taken to be $T_\infty = 300^\circ\text{K}$.

5.1 Performance as a function of Mach number

Optimum performance is obtained by keeping the projectile Mach number within a narrow range. This can be accomplished by dividing the launch tube into several segments filled with different propellant mixtures, and constraining the projectile to operate over a limited Mach number range in each segment.

Figures 5.3 to 5.6 show the effects of Mach number on the flow and combustion phenomena in a ram accelerator tube section filled with a gas mixture of $2H_2 +$

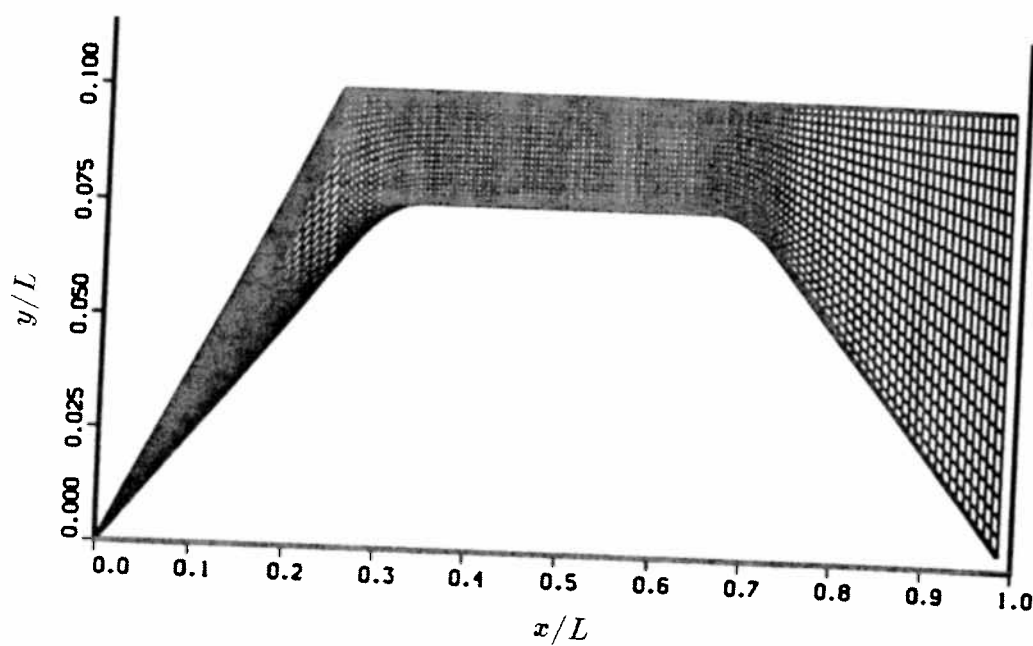


Figure 5.1: Typical grid for the ram accelerator. Vertical direction is magnified by a factor of 5.

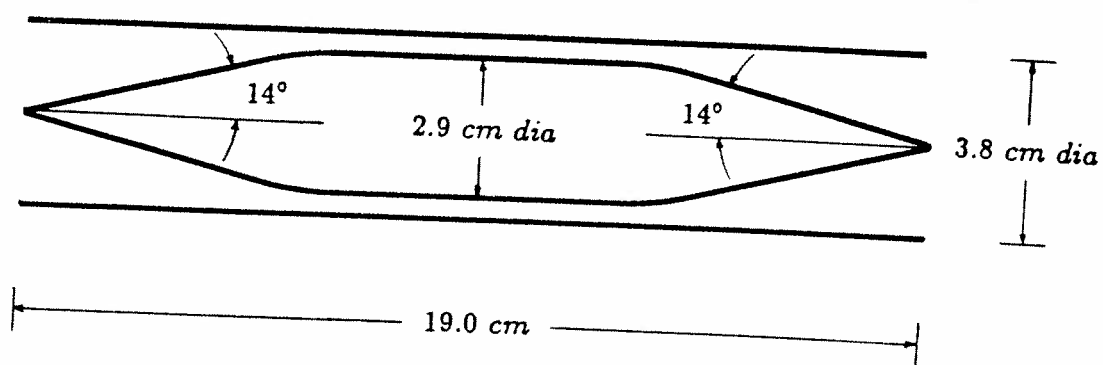


Figure 5.2: Ram accelerator configuration on a 1:1 scale.

$O_2 + 5He$ at a typical fill pressure of 20 atm. A projectile configuration having dimensions close to those of the experimental device presently operating at the University of Washington was chosen for this study (Fig. 5.2). The projectile is composed of two 14° half angle cones and a cylindrical section. The maximum projectile radius is 1.45 cm and its length is 19 cm. The tube radius is 1.9 cm.

Figures 5.3a and 5.3b show temperature contours and the temperature distribution along the projectile surface and tube wall for a Mach number $M = 7$ (flight speed $U_1 = 5.2$ km/s). The contour plot is magnified in the vertical direction by a factor of 5. The numerical solution shows the crisp shock waves captured by the computational method. At these flight conditions, the shock wave system generated by the projectile is not strong enough to ignite the mixture. Therefore, no combustion and no thrust is generated in this case.

A higher flight speed is required in order to ignite the mixture. Figure 5.4 shows the results for a Mach number $M = 8$ ($U_1 = 5.9$ km/s). At this Mach number, ignition is reached behind the second shock reflection, and rapid chemical reactions release energy into the flowing stream establishing a shock-induced combustion front. Shown in the contour plot are the nose bow shock and its reflection from the tube wall, followed by the combustion front and the expansion wave system over the tail of the projectile. A positive thrust force is produced at this flight condition.

The combustion front will remain behind the second shock reflection for a certain Mach number range. As the projectile accelerates inside the tube, the strength of the shock wave system increases and, at a given point, causes the combustion front to jump from the second shock reflection to the first. This situation is shown in Fig. 5.5 for a Mach number $M = 9$ ($U_1 = 6.7$ km/s). Note that due to the effect of the second reflection, which tends to speed up the reactions, the combustion zone at the projectile surface is narrower than at the tube wall.

The upper end of the velocity operating range is reached when the strength of the nose bow shock is sufficiently high to initiate combustion prematurely. For the present projectile configuration and gas mixture, this upper limit is reached near $M = 11$ ($U_1 = 8.1$ km/s). This case is shown in Fig. 5.6.

It is important to point out that in this ram accelerator combustion mode the flow remains supersonic throughout the length of the projectile. This is demon-

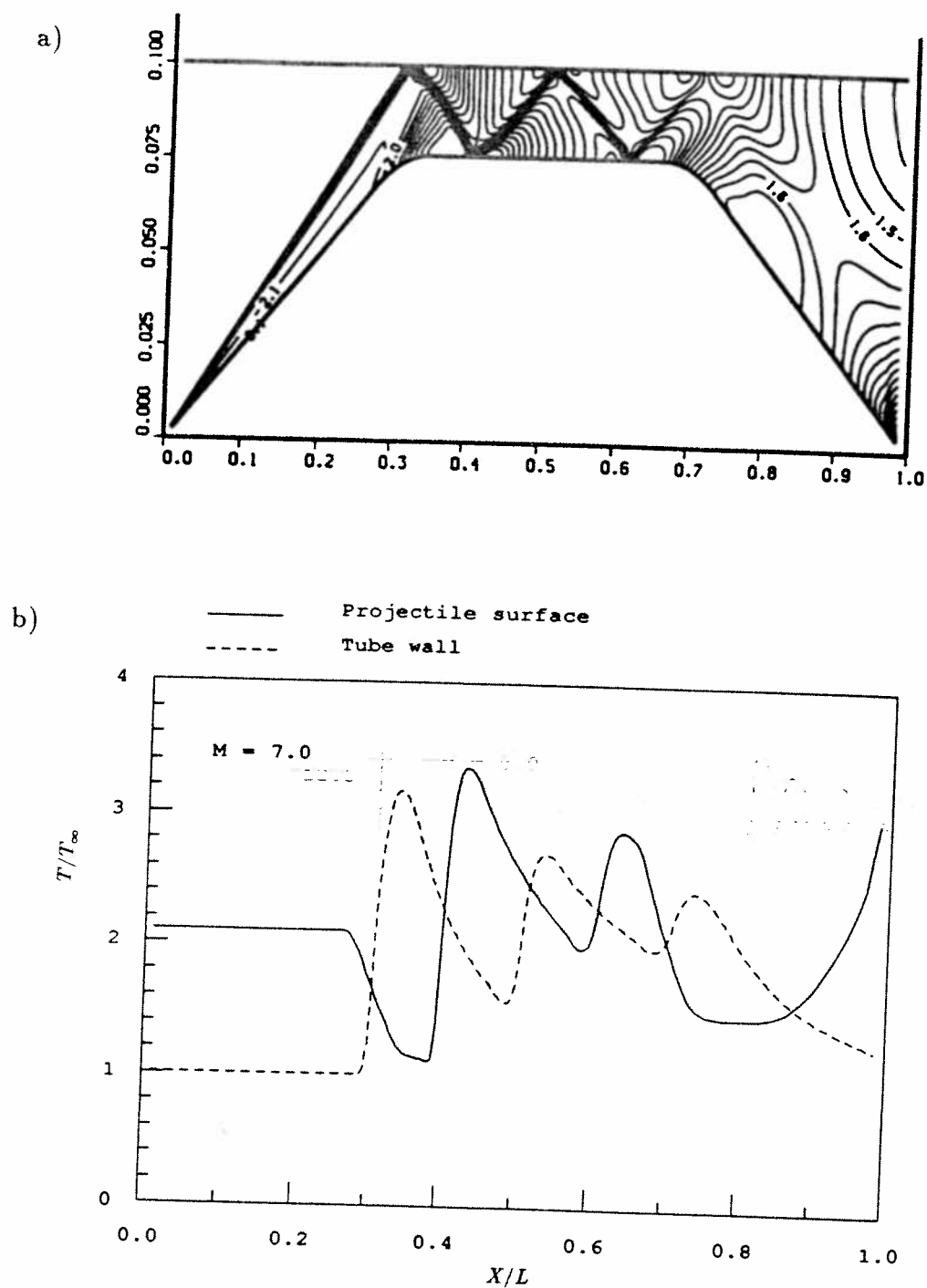


Figure 5.3: (a) Temperature contours T/T_∞ ; (b) temperature distribution; for a 14° projectile. $U_1 = 5.2$ km/s ($M=7$), mixture: $2H_2 + O_2 + 5He$

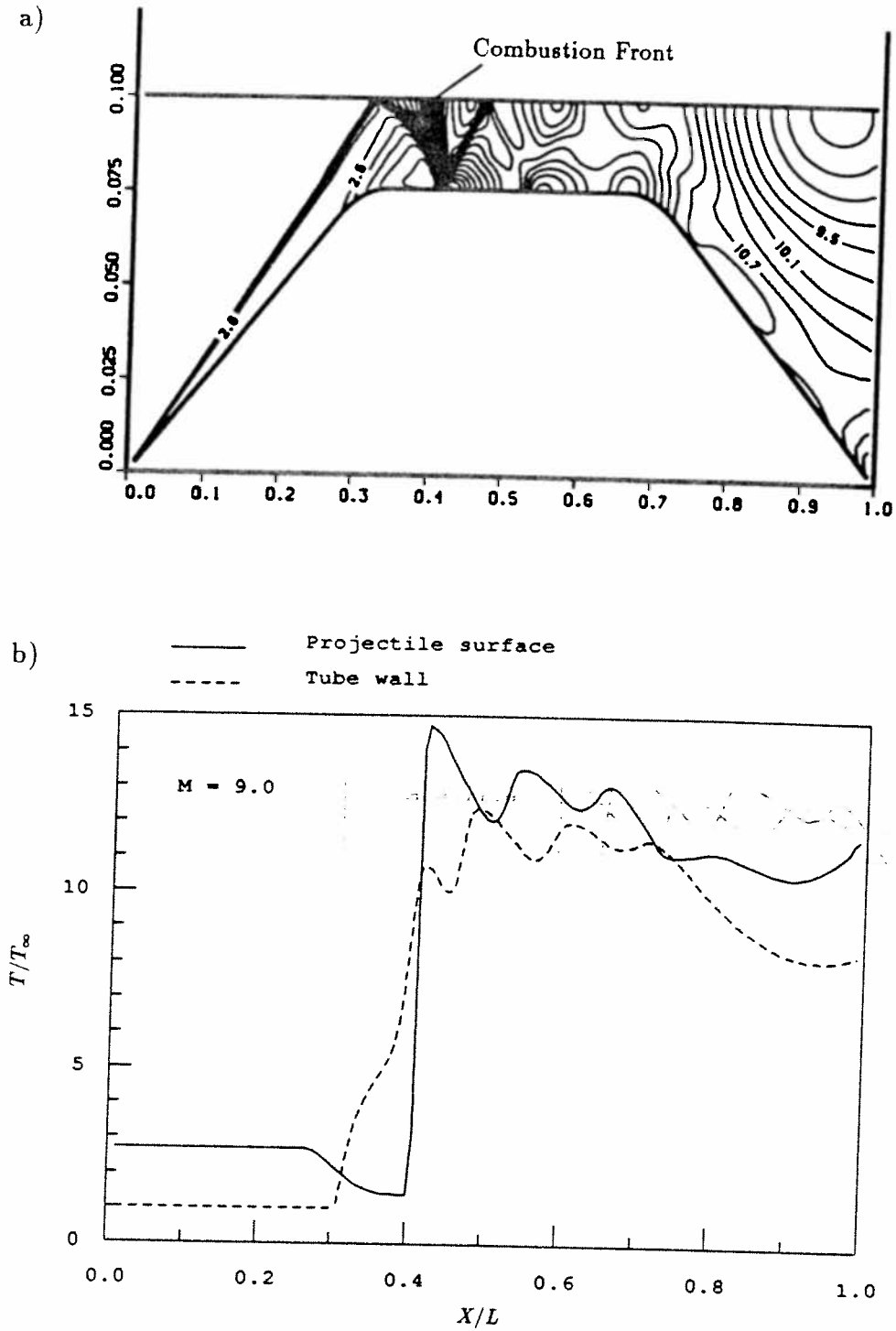


Figure 5.5: (a) Temperature contours T/T_∞ ; (b) temperature distribution; for a 14° projectile. $U_1 = 6.7$ km/s ($M=9$), mixture: $2H_2 + O_2 + 5He$

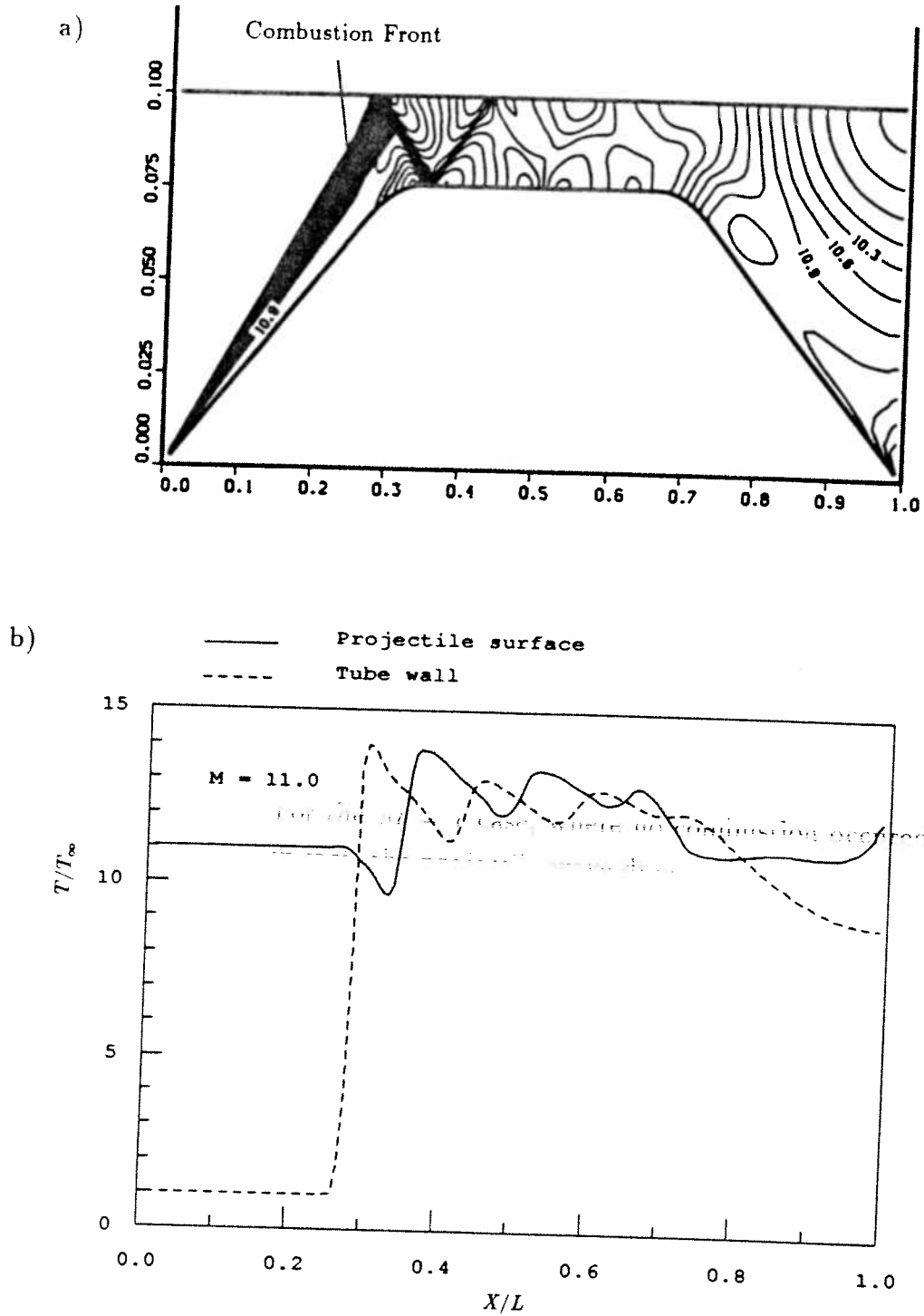


Figure 5.6: (a) Temperature contours T/T_∞ ; (b) temperature distribution; for a 14° projectile. $U_1 = 8.1$ km/s ($M=11$), mixture: $2H_2 + O_2 + 5He$

strated in Fig. 5.7 and Fig. 5.8, which show the variation of Mach number along the projectile surface and tube wall for the $M = 8$ and $M = 9$ cases, respectively.

Figures 5.9 and 5.10 show the species mass fraction distribution along the projectile surface for the $M = 8$ and $M = 9$ cases respectively. Note that some recombination is taking place at the tail of the projectile, indicating that some of the energy tied up in dissociated material is being converted to useful kinetic energy.

The pressure distribution along the projectile surface and tube wall for the four cases discussed above is shown in Figs. 5.11 to 5.14. Note that for the $M = 8$ and $M = 9$ cases the pressure at the projectile tail is higher than that at the nose, and as a result, a positive thrust force is produced.

A nondimensional thrust, F , can be defined as:

$$F = \frac{\bar{F}}{p_{\infty} A_t} \quad (5.1)$$

where \bar{F} is the thrust, p_{∞} is the fill pressure, and A_t is the tube area. For the $M = 8$ and $M = 9$ cases thrust forces $F = 3.27$ and $F = 2.93$ were obtained respectively. For the $M = 7$ case, where no combustion occurred, $F = -2.16$, which represents, in fact, the projectile wave drag.

The $M = 11$ case is particularly interesting, since, although it resulted in a net drag force, $F = -0.61$, its value was almost an order of magnitude lower than that obtained for the same flight conditions but with the assumption that the flow is frozen (no chemical reactions), in which case $F = -5.1$. This indicates that part of the chemical energy released can still be utilized for thrust production[†].

A similar result was observed experimentally by Ruegg and Dorsey⁴¹, who noted a large reduction of the drag coefficient of spherical missiles (fired into detonable mixtures) when combustion was established in the shocked gas. They even suggested the possibility of attaining positive thrust by properly shaping the projectile, however, to the best of this author's knowledge this was never attempted.

Before moving on to the next section, it is interesting to observe some particle traces in a ram accelerator configuration. These are shown in Fig. 5.15, which show

[†]For a 12° nose/tail half angle projectile, a very small positive thrust force was obtained in the case of premature combustion in a $2H_2 + O_2 + 5He$ mixture.

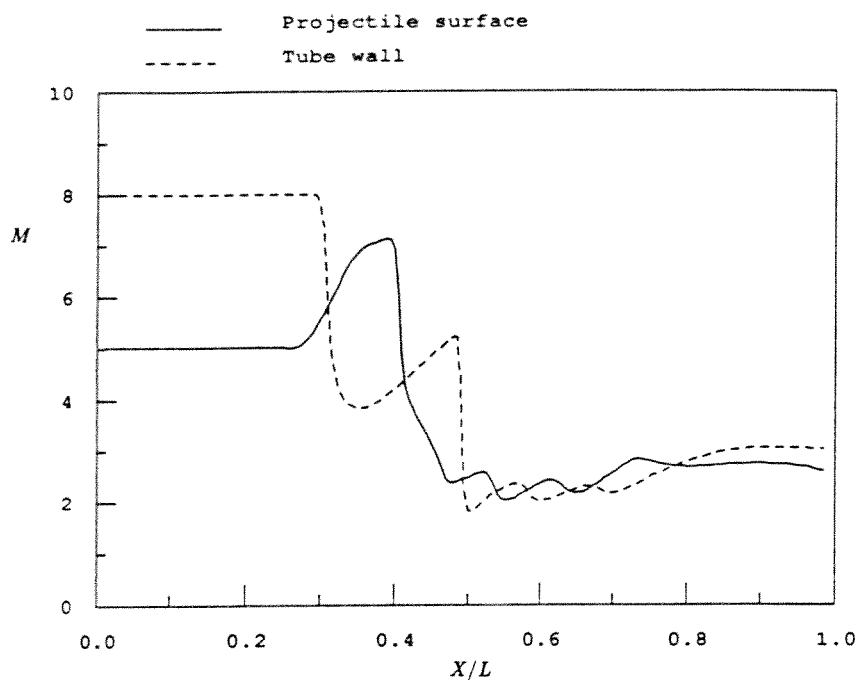


Figure 5.7: Mach number distribution along the tube wall and projectile surface for the $M=8$ case.

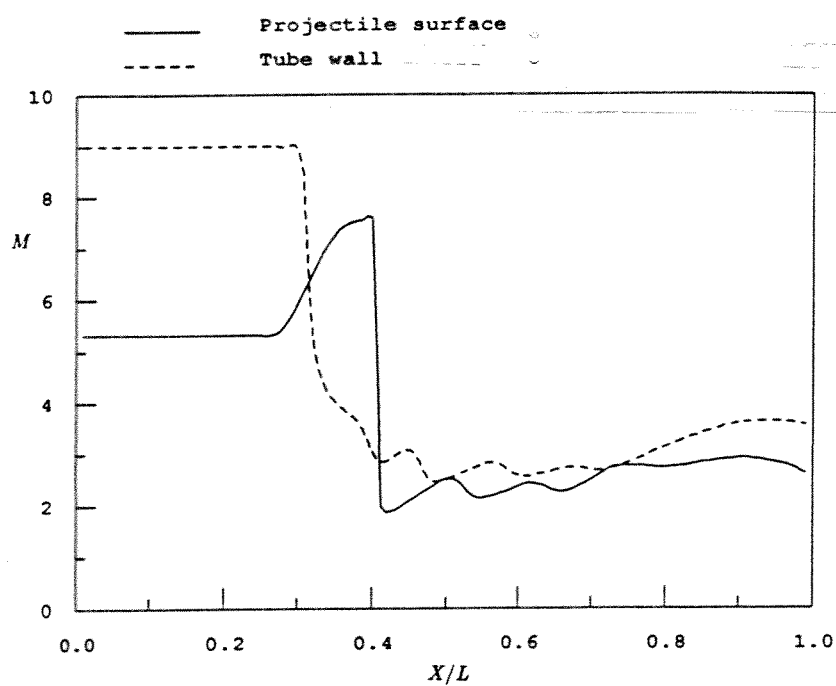


Figure 5.8: Mach number distribution along the tube wall and projectile surface for the $M=9$ case.

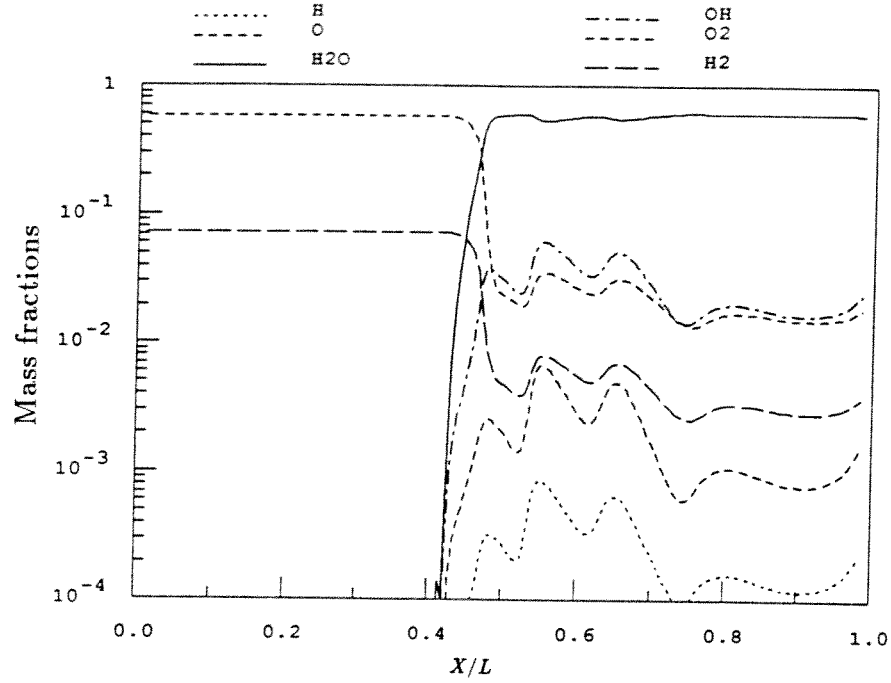


Figure 5.9: Species mass fraction distribution along the projectile surface for the M=8 case.

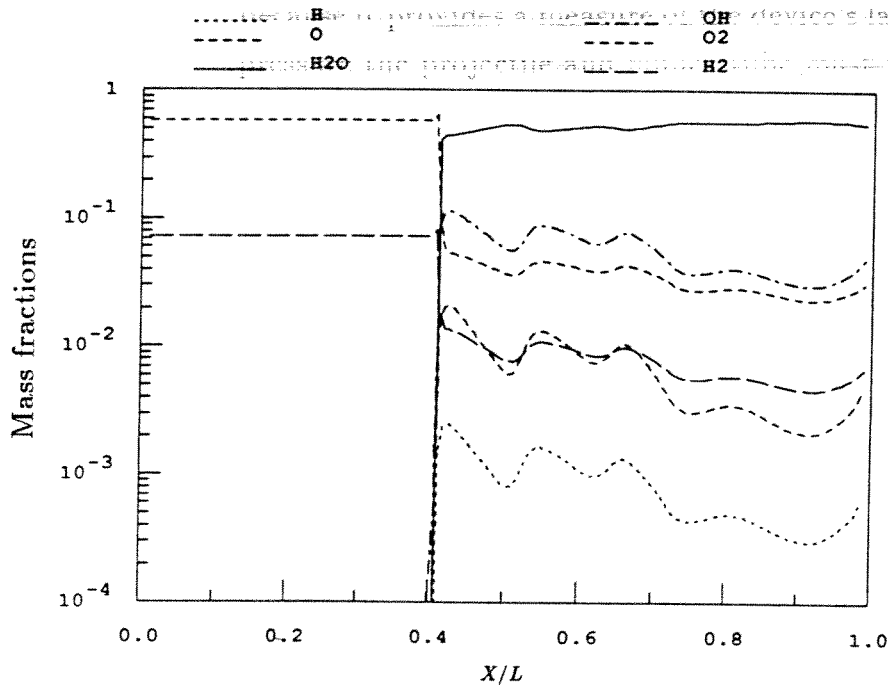


Figure 5.10: Species mass fraction distribution along the projectile surface for the M=9 case.

temperature contours and particle traces for a 12° nose/tail half angle projectile moving at $M = 9$ into the same $2H_2 + O_2 + 5He$ mixture.

5.2 Ballistic efficiency and thrust pressure ratio

The performance of the ram accelerator can be characterized by two main parameters: ballistic efficiency and thrust pressure ratio. The ballistic efficiency, η_b , is defined here as the ratio of the rate of change of kinetic energy of the projectile to the rate of expenditure of chemical energy. It can be expressed in the following way

$$\eta_b = \frac{\bar{F}U_1}{\bar{Q}} \quad (5.2)$$

where U_1 is the projectile speed, and \bar{Q} is the rate of heat release into the flow. The thrust pressure ratio, ϕ_t , is the net average drive pressure on the projectile (the thrust divided by the maximum projectile cross-sectional area) divided by the maximum cycle pressure. This ratio is an important performance parameter because it provides a measure of the device's launch capability versus the maximum pressure the projectile and launch tube must survive.

The thrust on the projectile is calculated by integrating the pressure over the length of the projectile³⁴

$$\bar{F} = -\bar{D} = -\int_0^L \bar{p} d\tilde{S} \quad (5.3)$$

where, $\tilde{S}(\tilde{x}) = \pi\tilde{r}^2$ is the cross-sectional area of the projectile at \tilde{x} . Equation (5.3) can also be written as

$$\bar{F} = -2\pi \int_0^L \bar{p}\tilde{r} \frac{d\tilde{r}}{d\tilde{x}} d\tilde{x} \quad (5.4)$$

The nondimensional thrust is then given by

$$F = \frac{\bar{F}}{p_\infty A_t} = -2 \frac{\gamma_\infty}{r_t^2} \int_0^1 pr \frac{dr}{dx} dx \quad (5.5)$$

The heat release is calculated as follows:

In steady state, the energy equation applied to the control volume of Fig. 5.16 is given by

$$\int_A (\tilde{e} + \bar{p}) \tilde{\mathbf{u}} \cdot \tilde{\mathbf{n}} dA = 0 \quad (5.6)$$

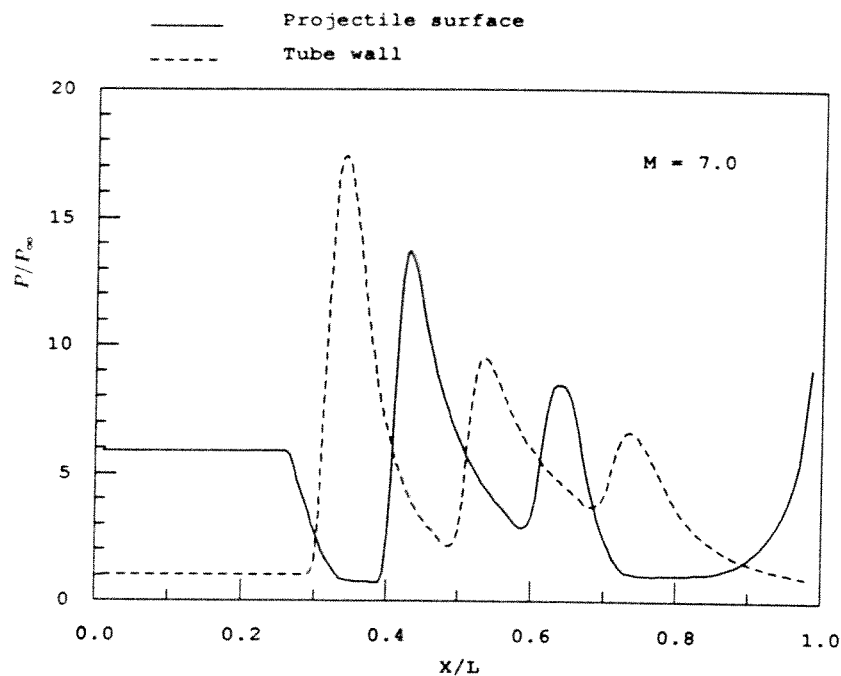


Figure 5.11: Pressure distribution along the tube wall and projectile surface for the $M=7$ case.

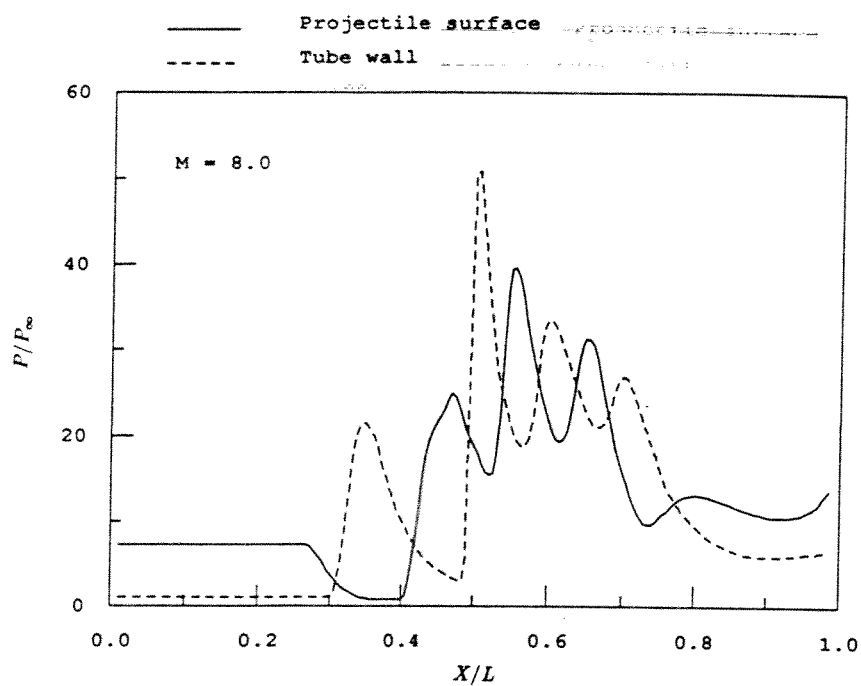


Figure 5.12: Pressure distribution along the tube wall and projectile surface for the $M=8$ case.

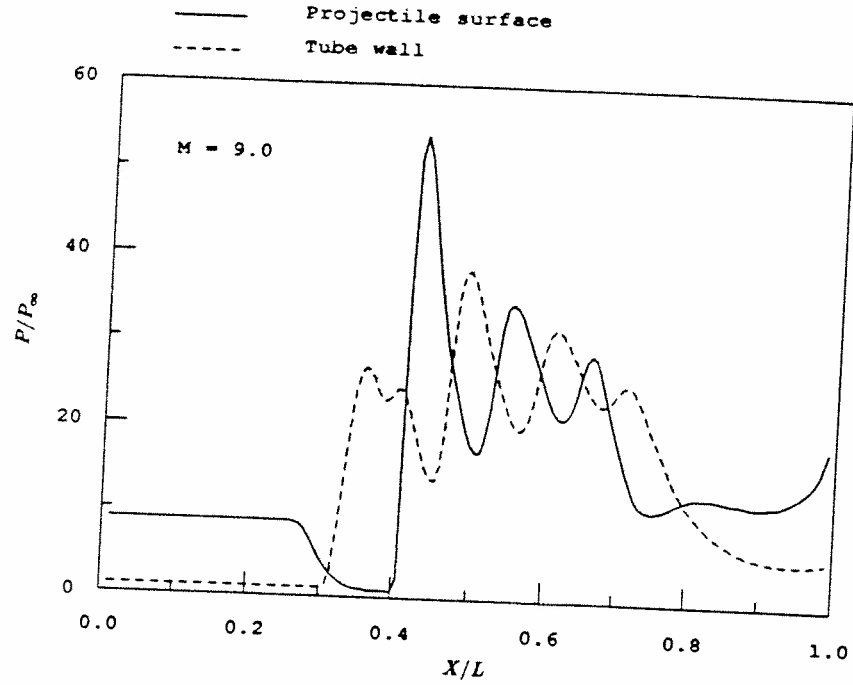


Figure 5.13: Pressure distribution along the tube wall and projectile surface for the $M=9$ case.

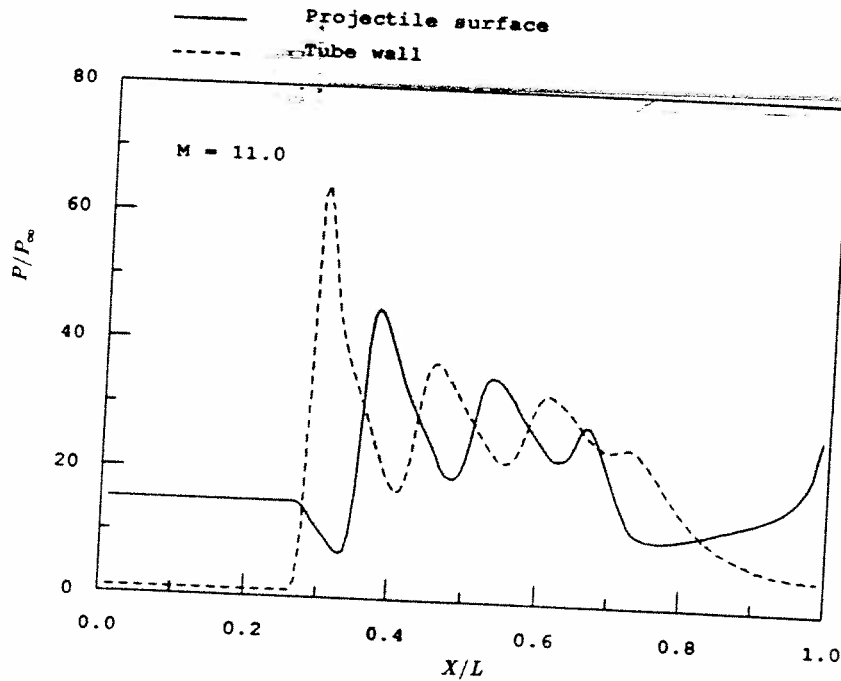
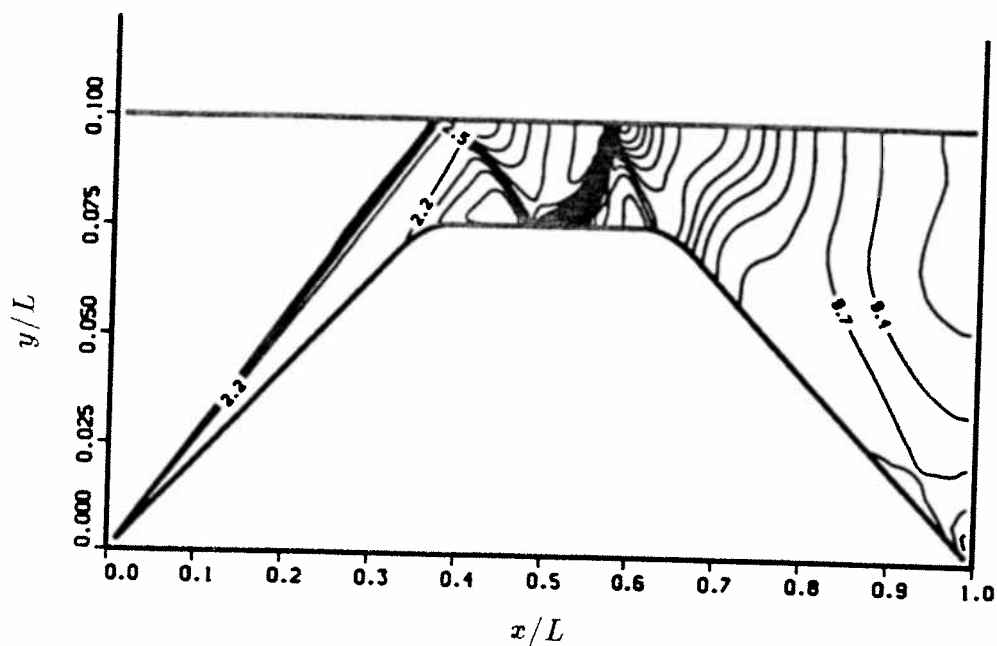


Figure 5.14: Pressure distribution along the tube wall and projectile surface for the $M=11$ case.

a)



b)

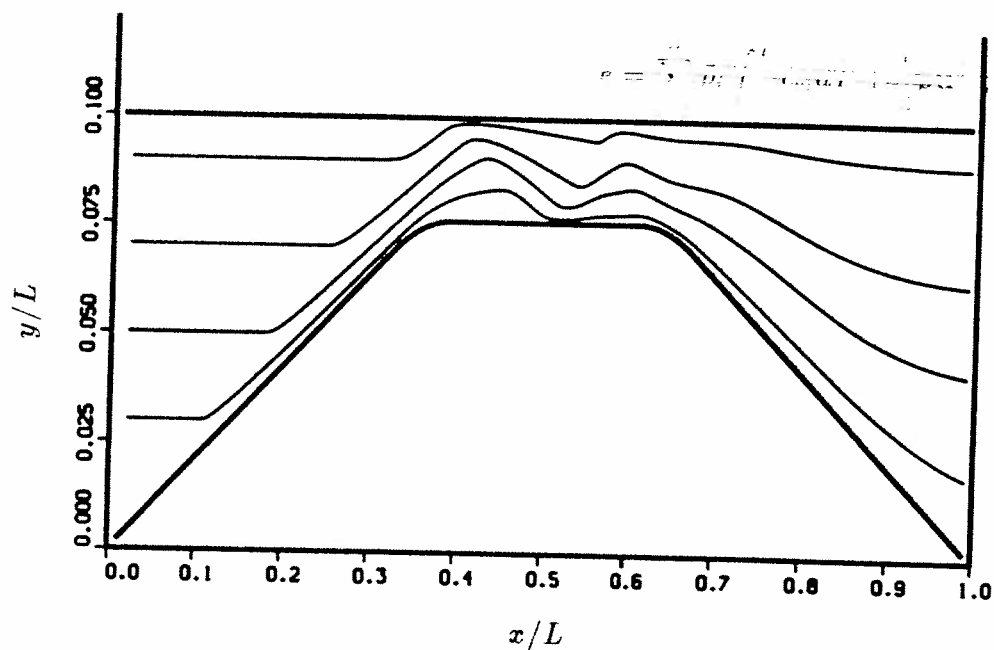


Figure 5.15: (a) Temperature contours T/T_∞ ; (b) particle traces; for a 12° projectile. ($M = 11$), mixture: $2H_2 + O_2 + 5He$

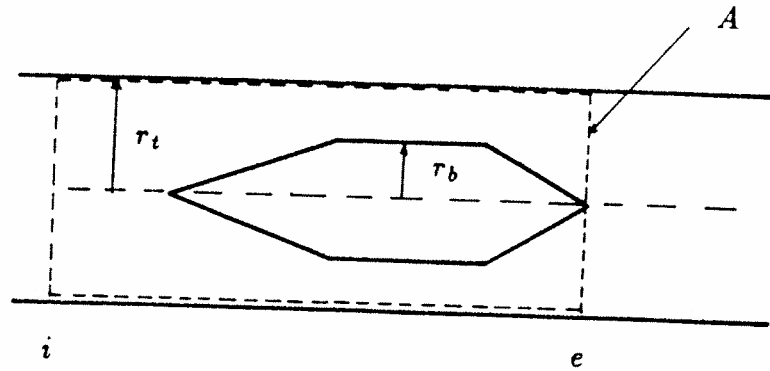


Figure 5.16: Control Volume used for the ram accelerator

where

$$e = \sum_{i=1}^n \tilde{\rho}_i \int_{\tilde{T}}^{\tilde{T}} \tilde{c}_{v,i} d\tilde{T} + \frac{1}{2} \tilde{\rho} \tilde{u}^2 + \sum_{i=1}^n \tilde{\rho}_i \tilde{h}_i^0 \quad (5.7)$$

therefore

$$\int_A \left[\sum_{i=1}^n \tilde{\rho}_i \int_{\tilde{T}}^{\tilde{T}} \tilde{c}_{v,i} d\tilde{T} + \frac{1}{2} \tilde{\rho} \tilde{u}^2 + \tilde{p} \right] \tilde{\mathbf{u}} \cdot \tilde{\mathbf{n}} dA = - \int_A \left(\sum_{i=1}^n \tilde{\rho}_i \tilde{h}_i^0 \right) \tilde{\mathbf{u}} \cdot \tilde{\mathbf{n}} dA \quad (5.8)$$

The term on the right hand side of equation 5.8 is identified as the rate of heat release \tilde{Q} . That is

$$\tilde{Q} = - \int_A \left(\sum_{i=1}^n \tilde{\rho}_i \tilde{h}_i^0 \right) \tilde{\mathbf{u}} \cdot \tilde{\mathbf{n}} dA \quad (5.9)$$

At the entrance of the control volume, the only species present are H_2 , O_2 and a diluent, all of which have $h_i^0 = 0$. Therefore, the rate of heat release is given by

$$\tilde{Q} = -2\pi \int_0^{\tilde{r}_t} \left(\sum_{i=1}^n (c_i \tilde{h}_i^0)_e \right) \tilde{\rho}_e \tilde{u}_e \tilde{r} d\tilde{r} \quad (5.10)$$

where the notation $()_e$ has been used to indicate values at the exit of the control

volume. In nondimensional variables, the heat release is given by

$$Q = \frac{\bar{Q}}{\rho_\infty c_\infty^3 L^2} = -2\pi \int_0^{r_t} \left(\sum_{i=1}^n (c_i h_i^0) \right) \rho_e u_e r dr \quad (5.11)$$

The ballistic efficiency is then given by

$$\eta_b = \frac{\bar{F} U_1}{\bar{Q}} = \frac{F p_\infty A_t U_1}{Q c_\infty^3 \rho_\infty L^2} \quad (5.12)$$

$$\frac{p_\infty A_t U_1}{c_\infty^3 \rho_\infty L^2} = \frac{M}{\gamma_\infty} \pi r_t^2 \quad (5.13)$$

and finally

$$\eta_b = \frac{F M}{Q \gamma_\infty} \pi r_t^2 \quad (5.14)$$

Similarly, the thrust pressure ratio, ϕ_t , can be written as

$$\phi_t = \frac{\bar{F}}{A_p \bar{p}_{max}} = \frac{F}{\gamma_\infty p_{max}} \left(\frac{r_t}{r_p} \right)^2 \quad (5.15)$$

The integrals in equations 5.5 and 5.11 are numerically evaluated using Simpson's rule.

Figure 5.17 shows the variation of ballistic efficiency as a function of projectile speed for two different projectiles, one having nose and tail half angles of 12° and the other 14° . The lowest speed data point in each case corresponds to a combustion front generated by the second shock reflection, while the highest speed corresponds to premature combustion at the bow shock. It is observed that higher efficiencies are obtained with the 12° nose projectile (up to 20%), however it must operate at higher speeds and Mach numbers. Note that the 12° projectile produces a very small positive thrust in the case of premature combustion. The operational Mach number range of the 12° projectile is approximately from $M = 9$ to $M = 11$ while that of the 14° projectile is from $M = 8$ to $M = 10$. For a given projectile, the ballistic efficiency decreases with increasing speed. This is due to the fact that the high pressure region behind the combustion zone is not very sensitive to changes in speed, while the nose wave drag increases significantly as the projectile speed increases.

Thrust pressure ratio results are shown in Fig. 5.18. Here, ϕ_t is plotted versus projectile speed. The trends shown here are similar to the trends shown for η_b in Fig. 5.17. Values of ϕ_t as high as 17% are obtained.

5.3 Performance as a function of area ratio

Figure 5.19 shows the ballistic efficiency of two projectiles (having 12° and 14° half nose/tail angles) as a function of projectile-to-tube area ratio, A_p/A_t , where A_p and A_t are the cross-sectional areas of the projectile and tube, respectively. The effect of increasing A_p/A_t is to increase the ballistic efficiency. This trend is similar to that observed in conventional ramjets, for which the thermal efficiency increases with increasing compression ratio. The ballistic efficiency is increased by approximately 50% in going from $A_p/A_t = 0.52$ to $A_p/A_t = 0.70$. There is however, a practical limitation on the maximum value of the area ratio. At values of A_p/A_t close to 1, the boundary layer on the projectile will extend up to the tube wall, reducing the efficiency of the system.

The thrust pressure ratio variation with A_p/A_t is shown in Fig. 5.20. Changing the area ratio does not appear to have a significant effect on ϕ_t , and it remains nearly constant. The small variations are probably associated with the wave interactions taking place for a particular geometric configuration.

5.4 Performance as a function of gas mixture

The performance of the ram accelerator operating in four different mixtures was also investigated for the 14° nose projectile. The four mixtures studied are listed in Table 5.1. The ratio of specific heats of the mixture, γ_∞ , has a significant effect on the ignition characteristics of the ram accelerator. The minimum value of the Mach number necessary to ignite the flow increases significantly with decreasing γ_∞ . Figure 5.21 shows the variation in nondimensional thrust, F , for the four gas mixtures as a function of projectile Mach number. Note that for the $2H_2 + O_2 + 5He$ mixture, having $\gamma_\infty = 1.530$, ignition was achieved at $M = 9$. For the $2H_2 + O_2 + 1.5He + 0.5Ar$ and $5H_2 + O_2 + 4He$ mixtures, having $\gamma_\infty = 1.477$ and $\gamma_\infty = 1.479$ respectively, ignition was possible only at $M = 10$. The fourth mixture, $8H_2 + O_2$,

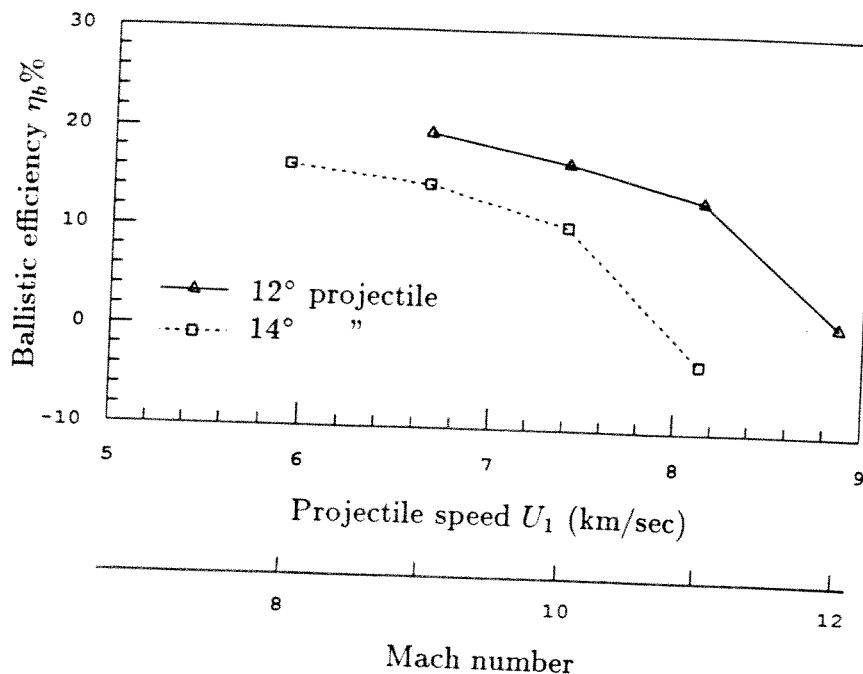


Figure 5.17: Ballistic efficiency as a function of ram accelerator projectile speed and Mach number for two projectile geometries. Mixture: $2H_2 + O_2 + 5He$.

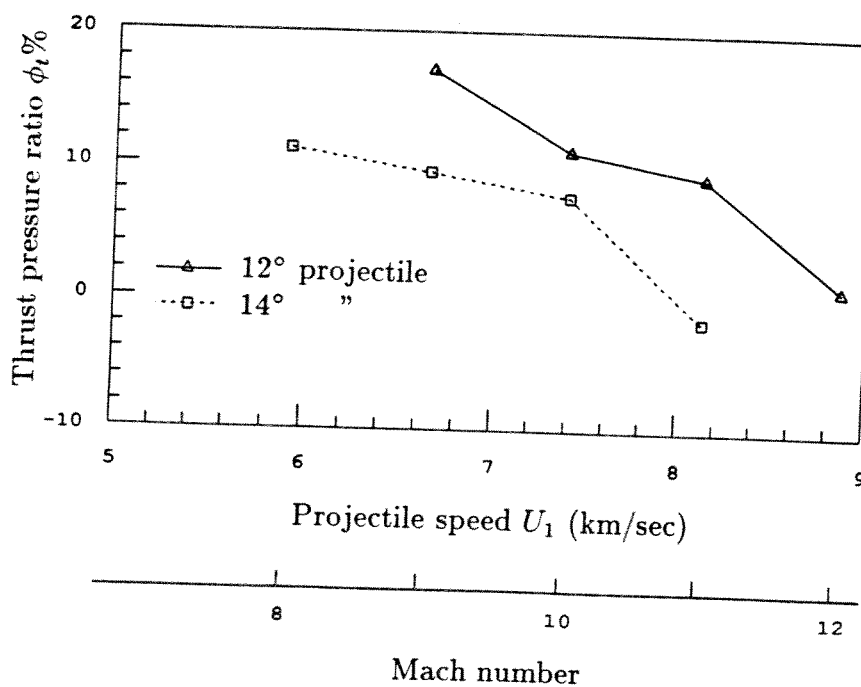


Figure 5.18: Thrust pressure ratio as a function of ram accelerator projectile speed and Mach number for two projectile geometries. Mixture: $2H_2 + O_2 + 5He$.

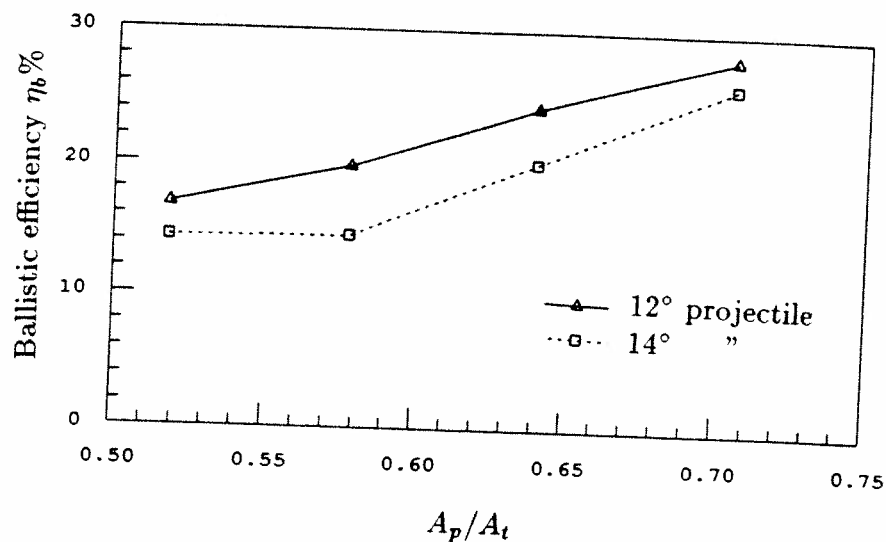


Figure 5.19: Ballistic efficiency as a function of projectile-to-tube area ratio. Mixture: $2H_2 + O_2 + 5He$.

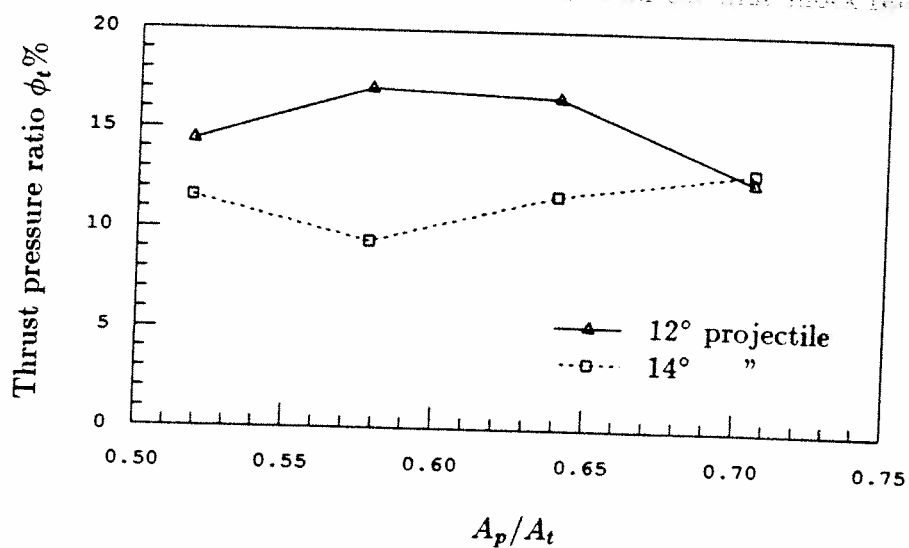


Figure 5.20: Thrust pressure ratio as a function of projectile-to-tube area ratio. Mixture: $2H_2 + O_2 + 5He$.

having the lowest ratio of specific heats ($\gamma_\infty = 1.404$), could not be ignited even at a Mach number $M = 12$.

Figure 5.21 also shows that for a given Mach number, the highest thrust levels are obtained for the mixture having the highest specific chemical energy content (i.e., closer to an H_2/O_2 stoichiometric mixture). Thus, at a Mach number $M = 10$, a higher thrust was obtained with the $2H_2 + O_2 + 1.5He + 0.5Ar$ mixture (having 2 moles of diluent) than with the $2H_2 + O_2 + 5He$ (5 moles of diluent) and the $5H_2 + O_2 + 4He$ (7 moles of diluent) mixtures. As previously mentioned, the $8H_2 + O_2$ mixture failed to ignite in this Mach number range.

Figure 5.22 shows the variation of the nondimensional thrust as a function of projectile speed for the four mixtures of Table 5.1. Note that the first three mixtures listed in Table 5.1 could in principle accelerate the projectile from 5.2 to 9.6 km/s. The ballistic efficiency variation with projectile speed is shown in Fig. 5.23. The $5H_2 + O_2 + 4He$ mixture resulted in relatively low efficiencies. Temperature contours for this mixture are shown in Figs. 5.24 to 5.26. At a Mach number $M = 10$ (Fig. 5.24), the combustion front is clearly decoupled from the second reflected shock wave. At $M = 11$ (Fig. 5.25), the two fronts are coupled. For this configuration, ignition was achieved behind the first shock reflection at $M = 12$ (Fig. 5.26). More efficient mixtures near the 10 km/s speed range should be investigated in the future. In particular, preheating the gas mixture may be necessary for obtaining efficient acceleration near and beyond the 10 km/s mark.

5.5 Blunt nose effects

The numerical results presented in the previous sections of this chapter, apply only to a ram accelerator operating in the superdetonative velocity range ("oblique detonation" mode). In this section, a numerical investigation of the effects of nose blunting on the flow and combustion processes in the ram accelerator is presented. This investigation is relevant to both the "oblique detonation" operation mode and the "thermally choked" operation mode. The "thermally choked" operation mode of the ram accelerator covers the subdetonative velocity range, and it is described in detail in Refs. 3-6.

The purpose of this study was to determine under what conditions a high tem-

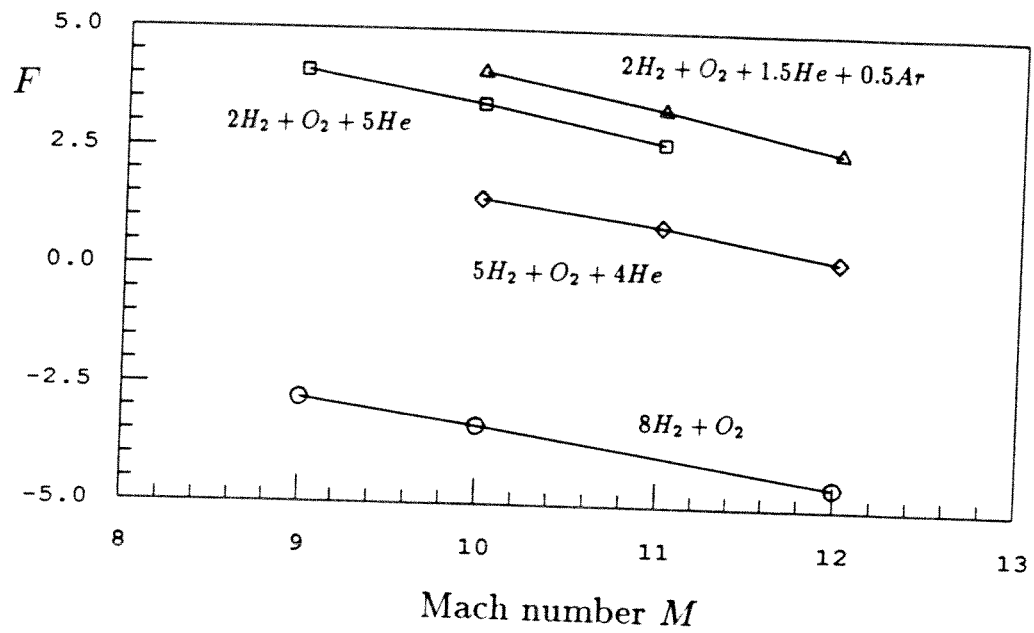


Figure 5.21: Nondimensional thrust as a function of Mach number.

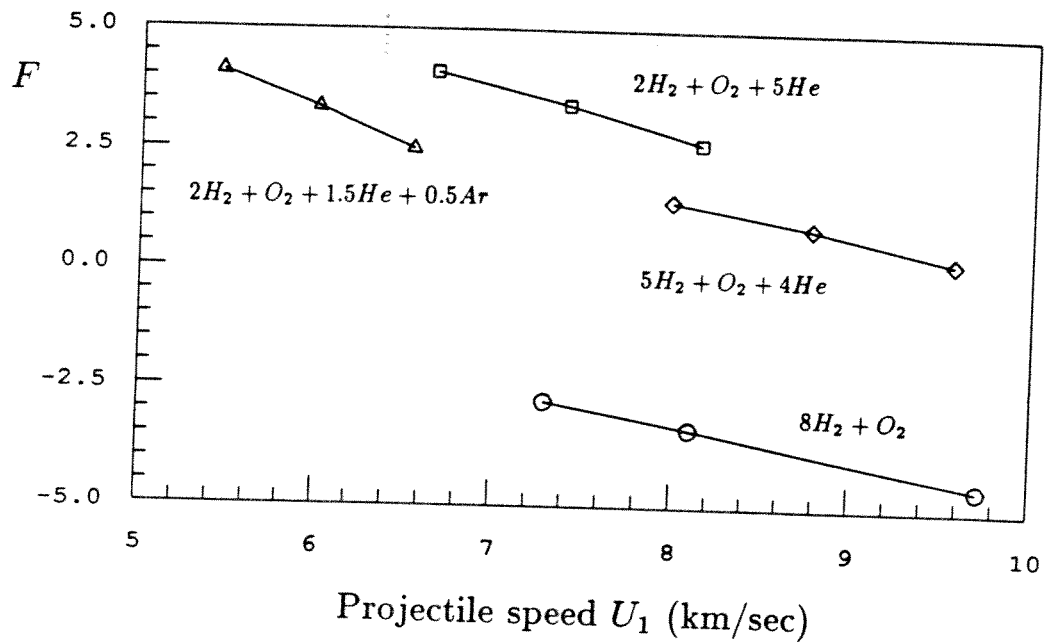


Figure 5.22: Nondimensional thrust as a function of projectile speed.

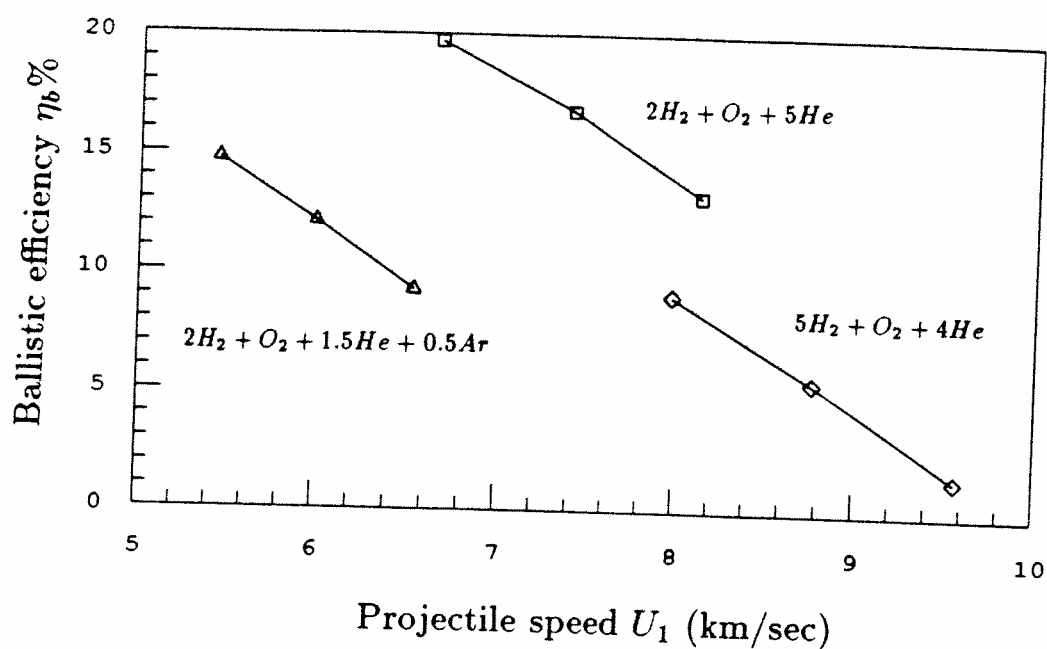


Figure 5.23: Ballistic efficiency as a function of projectile speed.

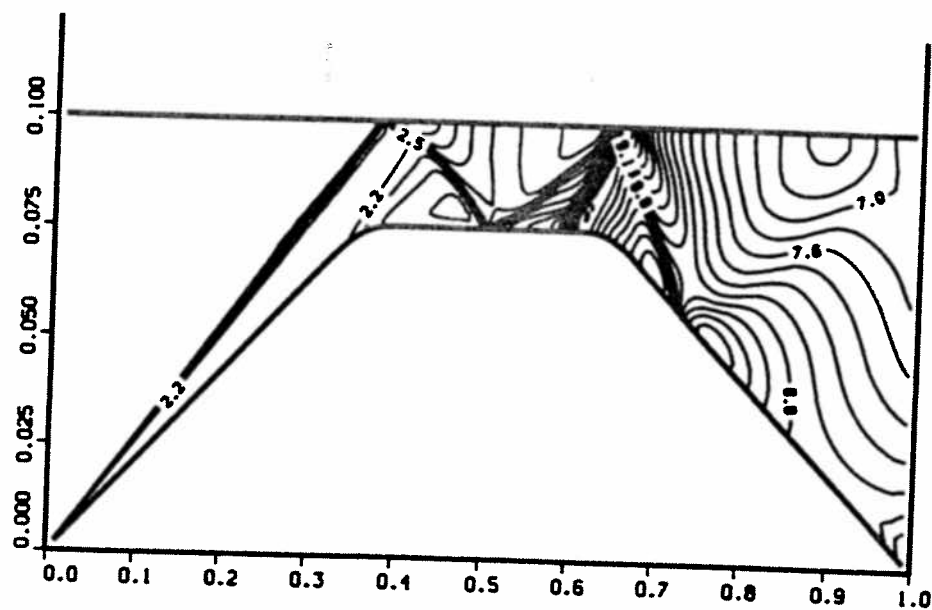


Figure 5.24: Temperature contours (T/T_∞) for a 12° projectile. $U_1 = 7.98$ km/s ($M=10$), mixture: $5H_2 + O_2 + 4He$.

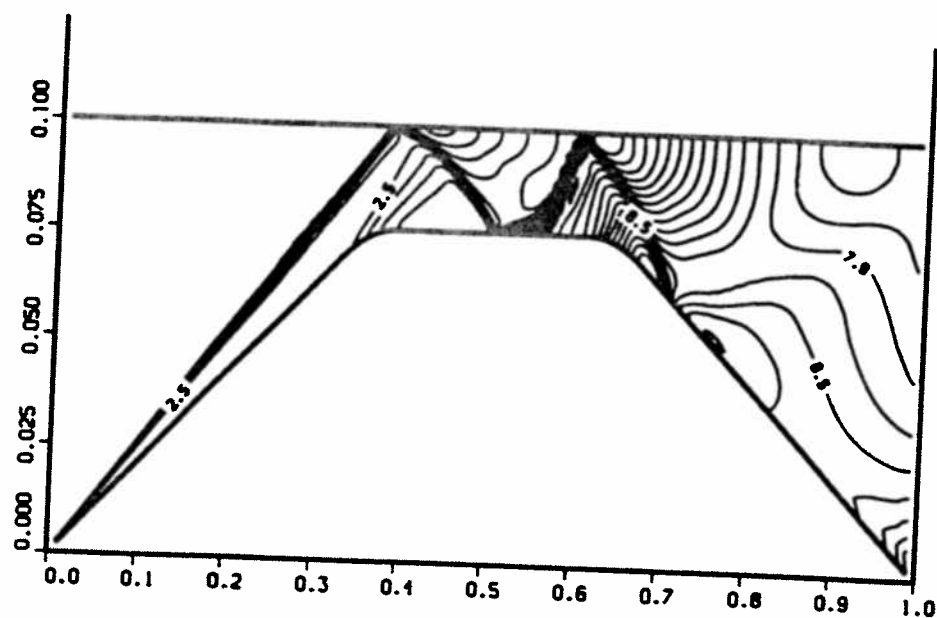


Figure 5.25: Temperature contours (T/T_∞) for a 12° projectile. $U_1 = 8.77$ km/s ($M=11$), mixture: $5H_2 + O_2 + 4He$.

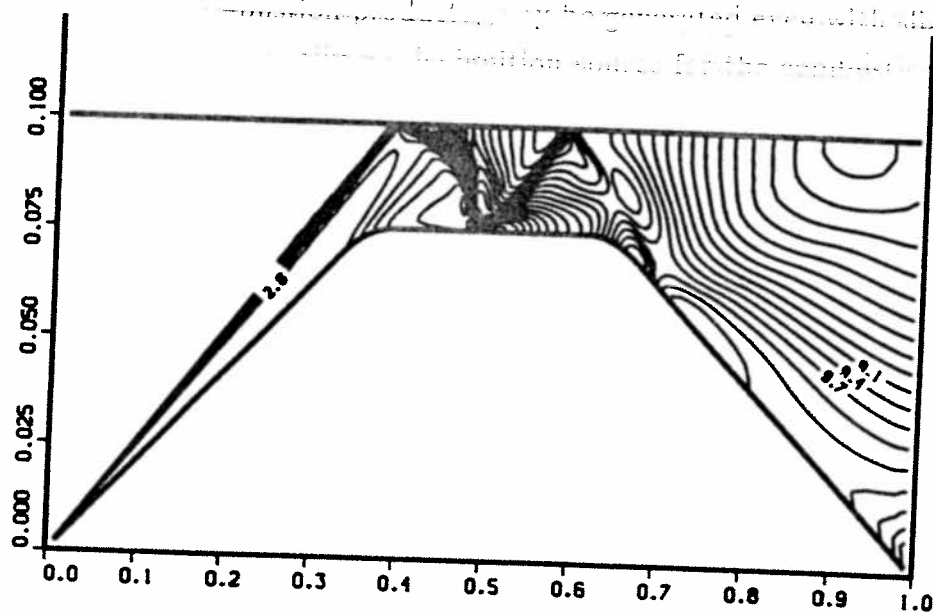


Figure 5.26: Temperature contours (T/T_∞) for a 12° projectile. $U_1 = 9.57$ km/s ($M=12$), mixture: $5H_2 + O_2 + 4He$.

Table 5.1: Properties of the four gas mixtures

<i>Mixture</i>	Molecular weight	p_{∞} <i>atm.</i>	T_{∞} $^{\circ}K$	γ_{∞}	c_{∞} <i>m/s</i>	D^{\dagger} <i>m/s</i>
$2H_2 + O_2 + 1.5He + 0.5Ar$	12.4	20	300	1.477	545.2	2970
$2H_2 + O_2 + 5He$	7.0	20	300	1.530	739.5	3850
$5H_2 + O_2 + 4He$	5.8	20	300	1.479	797.6	3903
$8H_2 + O_2$	5.3	20	300	1.404	810.4	3835

[†]Theoretical C-J detonation speed assuming chemical equilibrium

perature, thin entropy layer, originating from the nose stagnation region might be established, and what the interaction between this entropy layer and the reflected shock-wave coming from the tube wall would be. This study is important, since there is a possibility that such an entropy layer, consisting of high temperature combustion products, may be generated even with slight blunting of the nose, and may actually be the ignition source for the combustion processes in the ram accelerator operating in the "thermally choked" mode.

The projectile shape and grid used for this case is shown in Fig. 5.27. The projectile is composed of a 10° half angle cone with a spherical nose of radius 0.6 mm. The 10° half angle cone was selected to correspond with current projectile configurations being tested in the experimental ram accelerator facility at the University of Washington. A stoichiometric H_2 /air mixture and a pressure of 10 atm was considered. The Mach number is $M = 4.2$ in the present case. Under this conditions, which are typical of "thermally choked" ram accelerator operation, a high temperature entropy layer is formed on the projectile surface, as shown in Figs. 5.28 to 5.31.

Figure 5.28 shows temperature contours. The high temperature, thin entropy layer consisting of combustion products extends along the entire projectile surface. The nose region is shown in more detail in Fig. 5.29. The nose bow shock wave is reflected from the tube wall and it then interacts with the entropy layer. Note that in this interaction, the entropy layer remains very close to the body. However, the

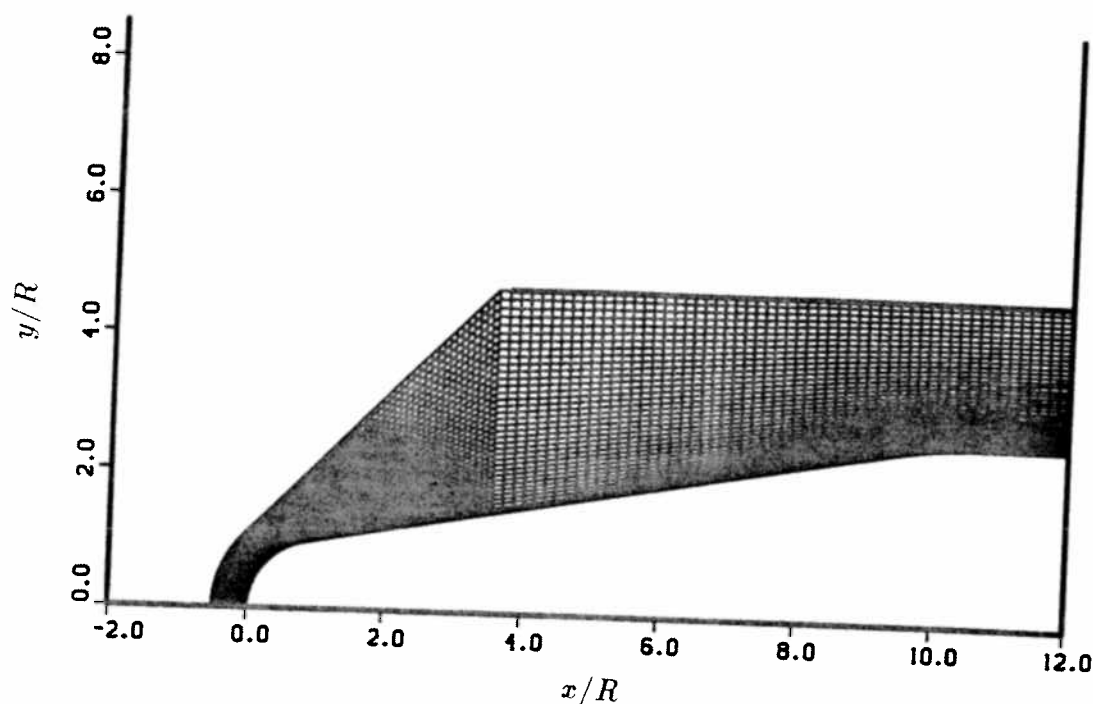


Figure 5.27: Grid used for the blunt nose studies

way in which the shock wave is reflected from the projectile surface is affected by the presence of the entropy layer. Figure 5.30, which consists of nondimensional pressure contours, shows that the shock reflection at the surface is actually a Mach reflection. In this type of reflection, a nearly normal shock that appears near the projectile surface forms a triple intersection point with the incident and "reflected" shock. This effect is more clearly seen in Fig. 5.31, which consists of particle traces. Behind the nearly normal shock, the streamlines are nearly parallel to the projectile surface and the flow is subsonic there. Also, since the streamlines behind the "reflected" shock are not parallel to the projectile surface, the triple point must be actually a short region in which the nearly normal shock continuously curves into the "reflected" shock, rather than being a true discontinuity. In the case of nonreacting flow, a "regular" reflection was observed. The gas properties inside the entropy layer of the reacting flow case, are such that a "regular" reflection is impossible.

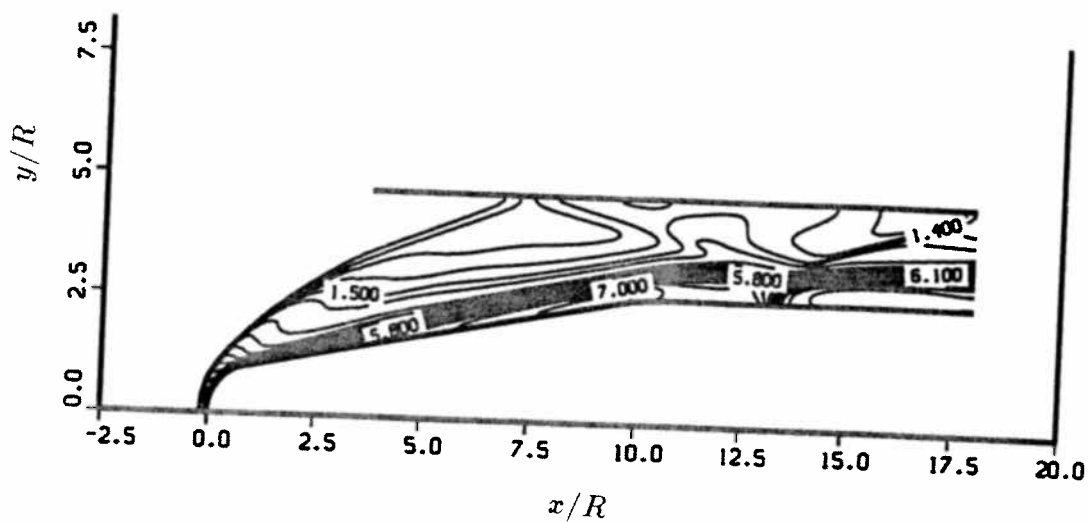


Figure 5.28: Temperature contours (T/T_∞) for a blunt projectile. $M = 4.2$, nose radius $R = 0.06$ cm, mixture: stoichiometric H_2/air .

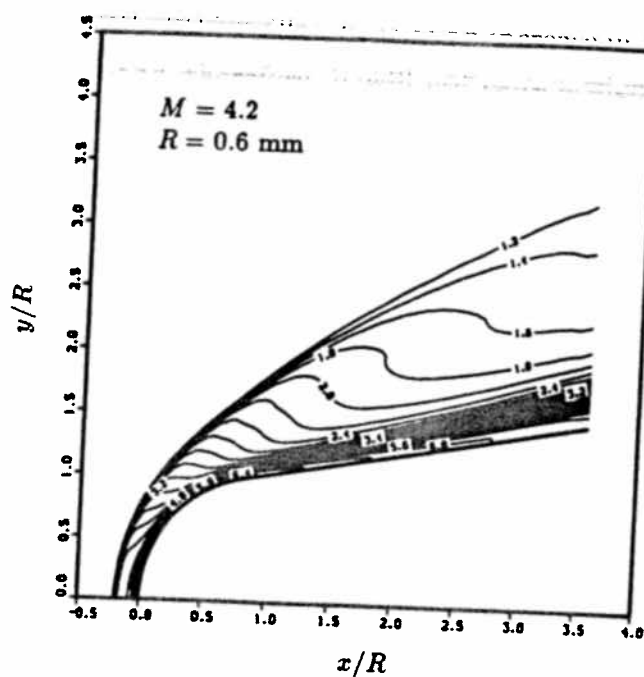


Figure 5.29: Temperature contours (T/T_∞) in the nose region of the blunt projectile.

The effects of viscosity in this type of interaction should also be investigated, since viscosity may provide a physical mechanism to diffuse the high temperature entropy layer into the main flow. A Full Navier-Stokes simulation would be required in this case.

A second effect the author wanted to investigate was the effect of limited combustion on the pressure distribution on the projectile surface. This is shown in Fig. 5.32, which shows a comparison between the results obtained for the chemically reacting case and those that would be obtained if no chemical reactions were allowed (frozen flow), keeping all the other parameters equal. The horizontal coordinate, S/R , in Fig. 5.32 represents the nondimensional distance along the projectile surface. Note that the combustion process has almost no effect on the pressure distribution. This effect is generally observed in unconfined chemically reacting flows. For example, Prabhu⁴⁷ found very small effects on the surface pressure distribution for flows past spheres, in the case of endothermic chemical reactions related to equilibrium air. This effect is very important to the ram accelerator concept, since it indicates that some combustion occurring in the nose area of the projectile can be allowed, and that this will not cause an increase in pressure over the frontal part of the projectile and, therefore, it will not cause a significant reduction in thrust.

As a final comment, Fig. 5.33 shows the temperature distribution along the projectile surface for the reacting and frozen flow cases. It is interesting to note that in the reacting case, the maximum temperature does not occur at the stagnation point but rather at a location on the spherical nose of the body corresponding to an angular distance of approximately 50° from the stagnation point. This is caused by the fact that the flow is in chemical nonequilibrium. If we consider a flow particle moving along the stagnation streamline, the above results indicate that it will not reach complete combustion at the stagnation point, but rather it will continue to react along the body surface. Complete combustion is attained near the 50° location, after which, due to the expansion process in this area of the body, the temperature begins to decrease.

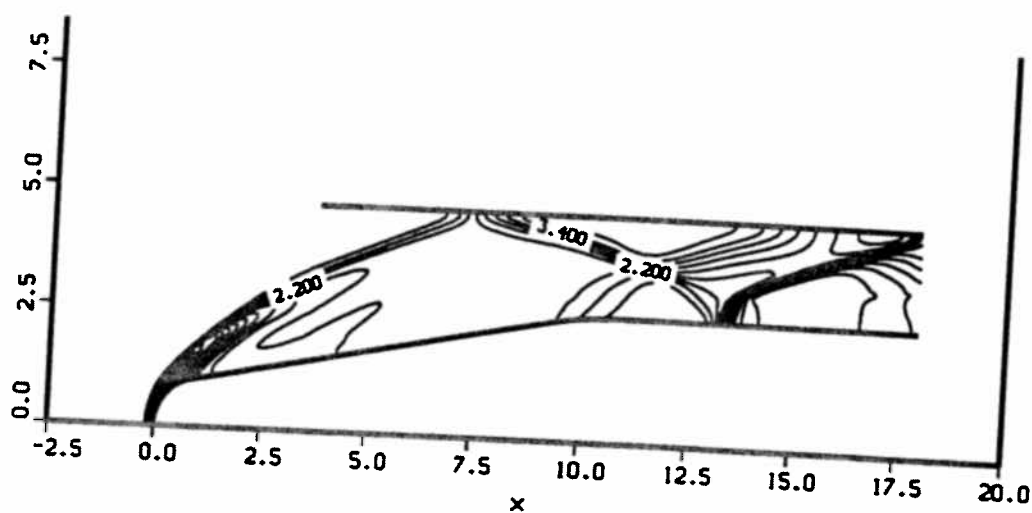


Figure 5.30: Pressure contours (p/p_∞) for a blunt projectile. $M = 4.2$, nose radius $R = 0.06$ cm, mixture: stoichiometric H_2/air .

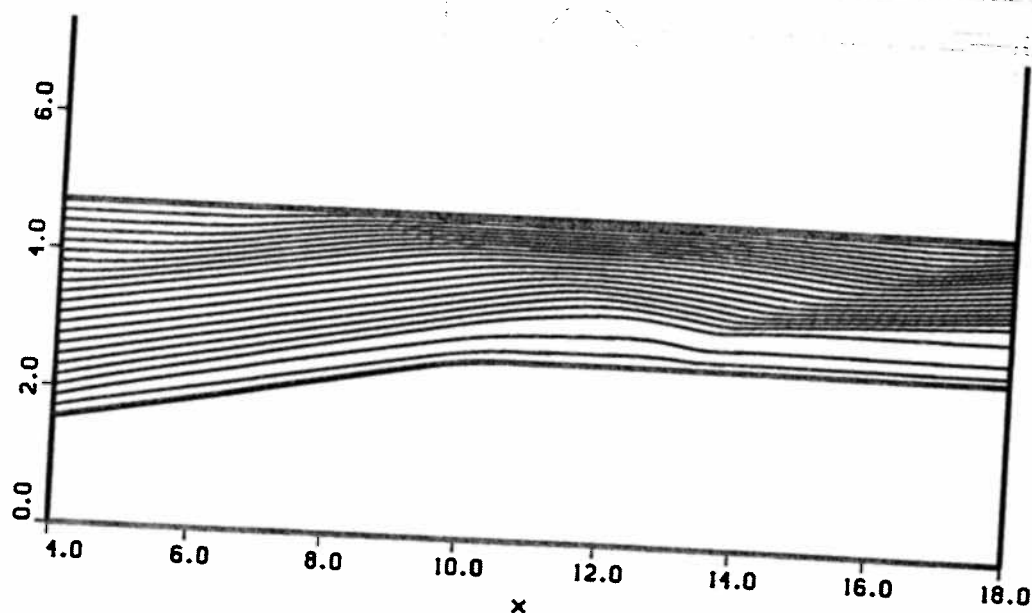


Figure 5.31: Particle traces for the blunt projectile.

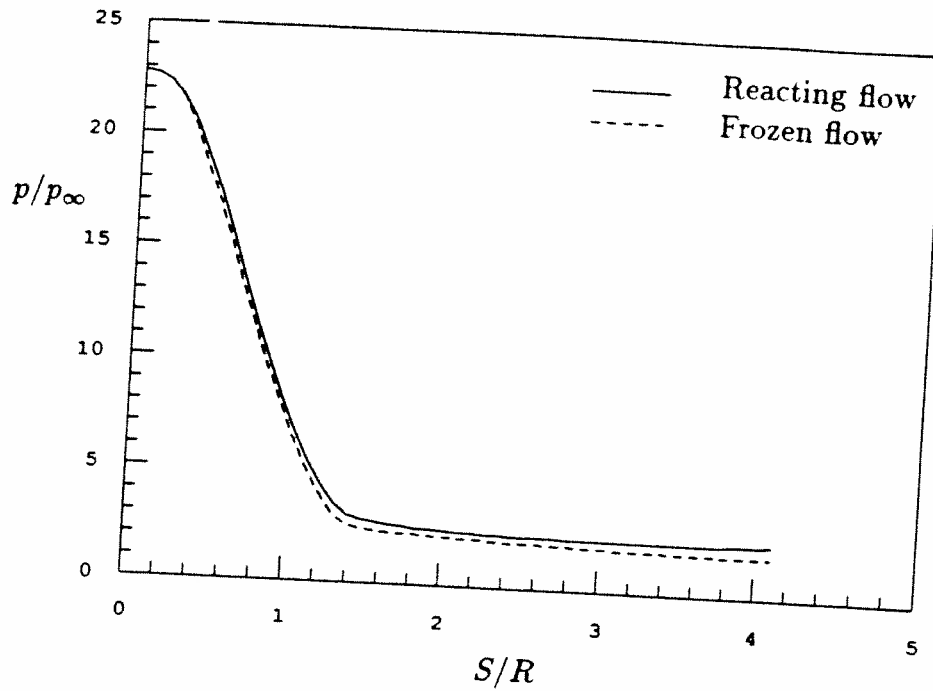


Figure 5.32: Comparison of pressure distribution on the projectile surface for reacting and frozen flows.

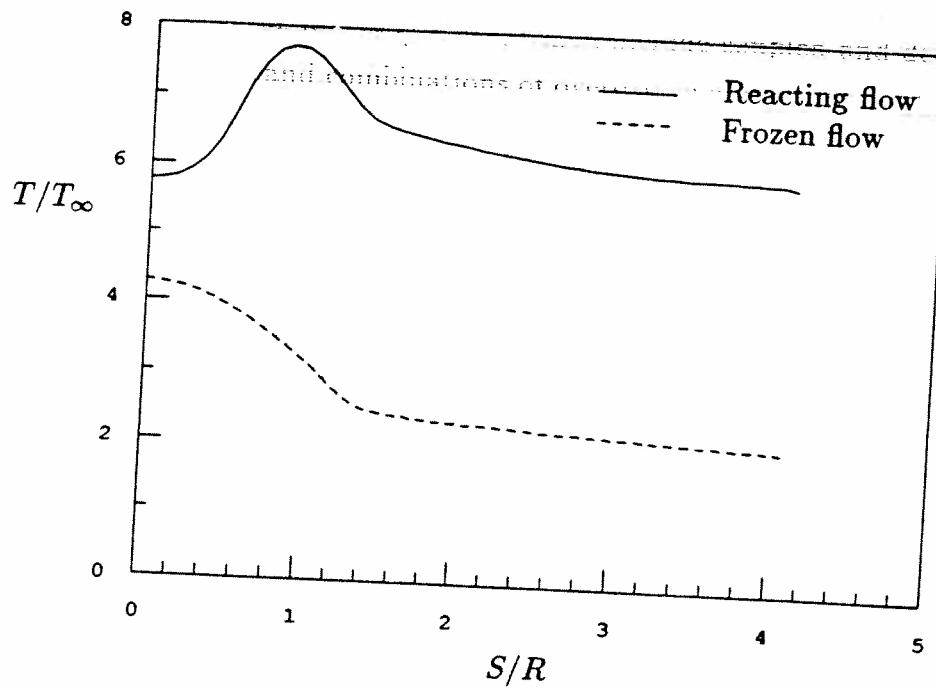


Figure 5.33: Comparison of temperature distribution on the projectile surface for reacting and frozen flows.

Chapter 6

CONCLUSIONS

An inviscid TVD numerical scheme for calculating hypersonic flows involving shock-induced combustion was presented. The analysis included nonequilibrium chemistry, real gas effects, and a 7 species-8 reaction combustion model for hydrogen/oxygen mixtures. Inviscid flow was assumed. The objective of the study was to investigate a hypervelocity mass launcher concept known as the "ram accelerator". The numerical scheme was validated by using benchmark test cases for which analytical, numerical and experimental results were available. Of particular importance were a series of numerical simulations conducted on the exothermic blunt body flow problem. The various combustion regimes observed in exothermic blunt body flows, which include coupled and decoupled shock-deflagration systems and combinations of overdriven and oblique detonation waves, were successfully reproduced using the present numerical scheme for stoichiometric mixtures of H_2/O_2 and H_2/air . The numerical results were compared with previously published experiments. Good agreement between the computed and experimentally observed shock location was obtained. A comparison with the numerical results of Lee and Deiwert was also presented. The results obtained with the two numerical methods were in good agreement. The numerical scheme was subsequently applied to investigate the flow, combustion, and performance characteristics of various ram accelerator configurations in the superdetonative velocity range of 5.0 to 10.0 km/s. The ballistic efficiency and thrust pressure ratio increased when the projectile nose and tail angles were reduced, however, the ram accelerator would have to operate at higher Mach numbers. The ballistic efficiency increased with increasing projectile-to-tube area ratio. This area ratio had no significant effect on the thrust pressure ratio. Ballistic efficiencies of up to 28% and thrust pressure ratios as high as 17% were observed. An investigation of the effects of gas mixture composition on the performance of the ram accelerator was also conducted. The ratio of specific heats of the

mixture, γ_∞ , was found to have a significant effect on the ignition characteristics of the ram accelerator. The minimum value of the Mach number necessary to ignite the flow increased significantly with decreasing γ_∞ . Also, for a given Mach number, the highest thrust levels were obtained for the mixture having the highest specific chemical energy content. The effects of nose blunting on the flow and combustion processes in the ram accelerator were also investigated. Under the assumption of inviscid flow, it was found that the high temperature, thin entropy layer produced under certain conditions, remains attached to the body even in the region behind the reflected shock wave impinging upon it. However, the presence of the entropy layer created a Mach reflection at the projectile surface. Viscous effects on this shock-entropy layer interaction should be investigated. This limited combustion layer had a very small effect on the pressure distribution at the projectile surface. Therefore, it can be concluded that limited combustion can be allowed to take place in the frontal area of the projectile, without significantly reducing the thrust force in the ram accelerator. Even in the most severe case of full premature combustion at the bow shock, a drag reduction (and sometimes even a very small positive thrust force) was observed. *None of Gasdynamic Phenomena Associated with the Ram Accelerator*

LIST OF REFERENCES

- [1] O'Brien, C.J. and Kobayashi, A.C., "Advanced Earth-to-orbit Propulsion Concepts," AIAA Paper 86-1386, June 1986.
- [2] Pratt, D.T., Humphrey, J.W. and Glenn, D.E., "Morphology of a Standing Oblique Detonation Wave," AIAA Paper 87-1785, June 1987.
- [3] Hertzberg, A., Bruckner, A.P. and Bogdanoff, D.W., "Ram Accelerator: A New Chemical Method for Accelerating Projectiles to Ultrahigh Velocities," *AIAA Journal*, vol. 26, Feb. 1988, pp 195-203.
- [4] Bruckner, A.P., Bogdanoff, D.W., Knowlen, C. and Hertzberg, A., "Investigations of Gasdynamic Phenomena Associated with the Ram Accelerator Concept," AIAA Paper 87-1327, June 1987.
- [5] Knowlen, C., Bruckner, A.P., Bogdanoff, D.W. and Hertzberg, A., "Performance Capabilities of the Ram Accelerator," AIAA Paper 87-2152, June 1987.
- [6] Bruckner, A.P., Knowlen, C., Scott, K.A. and Hertzberg, A., "High Velocity Modes of the Thermally Choked Ram Accelerator," AIAA Paper 88-2925, July 1988.
- [7] Yungster, S., Eberhardt, S. and Bruckner, A.P., "Numerical Simulation of Shock-Induced Combustion Generated by High-Speed Projectiles in Detonable Gas Mixtures," AIAA Paper 89-0673, Jan. 1989.
- [8] Yungster, S. and Bruckner, A.P., "A Numerical Study of the Ram Accelerator Concept in the Superdetonative Velocity Range," AIAA Paper 89-2677, July 1989.

- [9] Brackett, D.C. and Bogdanoff, D.W., "Computational Investigation of Oblique Detonation Ramjet-in-Tube Concepts," *Journal of Propulsion and Power*, Vol. 5, No. 3, May-June 1989, pp. 276-281.
- [10] Rom, J. and Kivity, Y., "Accelerating Projectiles up to 12 km/s Utilizing the Continuous Detonation Propulsion Method," AIAA Paper 88-2969, July 1988.
- [11] Kull, A., Burnham, E., Knowlen, C., Bruckner, A.P. and Hertzberg, A., "Experimental Studies of Superdetonative Ram Accelerator Modes," AIAA Paper 89-2632, July 1989.
- [12] Bruckner, A.P. and Hertzberg, A., "Ram Accelerator Direct Launch System for Space Cargo," Paper No. IAF-87-211, 38th Congress of the International Astronautical Federation, Brighton, England, Oct. 1987.
- [13] Kaloupis, P. and Bruckner, A.P., "The Ram Accelerator: A Chemically Driven Mass Launcher," AIAA Paper 88-2968, July 1988.
- [14] Dwoyer, D.L., Kutler, P., and Povinelli, L.A., "Retooling CFD for Hyperonic Aircraft," *Aerospace America*, Vol. 25, Oct. 1987, pp 32-35.
- [15] Povinelli, L.A., "Advanced Computational Techniques for Hypersonic Propulsion," NASA Technical Memorandum 102005, Sept. 1989.
- [16] Bogdanoff, D.W. and Brackett, D.C., "A Computational Fluid Dynamics Code for the Investigation of Ramjet-in-Tube Concepts," AIAA Paper 87-1978, June 1987.
- [17] Vincenti, W.G. and Kruger, C.H., *Introduction to Physical Gas Dynamics*, Wiley, New York, 1985, Chap. VII.
- [18] Stull, D.R. and Prophet, H., "JANAF Thermochemical Tables, 2nd. Ed.," NSRDS-Report 37, National Bureau of Standards, June 1971.

- [19] Esch, D.D., Siripong, A. and Pike, R. W., "A technical Report on Thermodynamic Properties In Polynomial Form For Carbon, Hydrogen, Nitrogen and Oxygen Systems From 300 to 15000°K," NASA-RFL-TR-70-3, Nov. 1970.
- [20] Wada, Y., Kubota, H., Ogawa, S. and Ishiguro, T., "A Diagonalizing Formulation of General Real Gas-Dynamic Matrices With a New Class of TVD Schemes," AIAA Paper 88-3596-CP, July 1988.
- [21] Moretti, G., "A New Technique for the Numerical Analysis of Nonequilibrium Flows," *AIAA Journal*, vol. 3, Feb. 1965, pp. 223-229.
- [22] Evans, J.S. and Schexnayder, C.J., "Influence of Chemical Kinetics and Unmixedness on Burning in Supersonic Hydrogen Flames," *AIAA Journal*, vol. 18, Feb. 1980, pp. 188-193.
- [23] Jachimowski, C.J., "An Analytical Study of the Hydrogen-Air Reaction Mechanism with Application to Scramjet Combustion," NASA TP 2791, Feb. 1988.
- [24] Oran, E., Young, T. and Boris, J., "Application of Time-Dependent Numerical Methods to the Description of Reactive Shocks," *Proc. 17th Int. Symp. on Combustion*, The Combustion Institute, Pittsburg, Pa., 1978.
- [25] Rogers, R.C. and Chinitz, W., "On the Use of a Global Hydrogen-Air Combustion Model in the Calculation of Turbulent Reacting Flow," AIAA Paper 82-0112, 1982.
- [26] Taki, S. and Fujiwara, T., "Numerical Analysis of Two-Dimensional Nonsteady Detonations," *AIAA Journal*, vol. 16, No. 1, Jan. 1978.
- [27] Cambier, J.L., Adelman, H. and Menees, G.P., "Numerical Simulations of an Oblique Detonation Wave Engine," AIAA Paper 88-0063, Jan. 1988.
- [28] Bussing, T.R.A. and Murman, E.M., "Finite-Volume Method for the Calculation of Compressible Chemically Reacting Flows," *AIAA Journal*, vol. 26, Sept. 1988, pp. 1070-1078.

- [29] Candler, G.V. and MacCormack, R.W., "The Computation of Hypersonic Ionized Flows in Chemical Thermal Nonequilibrium," AIAA Paper 88-0511, Jan. 1988.
- [30] Yee, H.C. and Shinn, J.L., "Semi Implicit and Fully Implicit Shock-Capturing Methods for Nonequilibrium Flows," *AIAA Journal*, vol. 27, March 1989, pp. 299-307.
- [31] Park C. and Yoon, S., "A Fully-Coupled Implicit Method for Thermo-Chemical Nonequilibrium Air at Sub-Orbital Flight Speeds," AIAA Paper 89-1974, June 1989.
- [32] Yoon, S. and Jameson, A., "Lower-Upper Symmetric-Gauss-Seidel Method for the Euler and Navier-Stokes Equations," *AIAA Journal*, vol. 26, Sept. 1988, pp. 1025-1026.
- [33] Roe, P.L., "Generalized Formulation of TVD Lax-Wendroff Schemes," Inst. for Computer Applications in Science and Engineering, Hampton, VA, Rept. 84-20, June 1984.
- [34] Anderson, D.A., Tannehill, J.C. and Pletcher, R.H., *Computational Fluid Mechanics and Heat Transfer*, Hemisphere/McGraw-Hill, 1984, Chap. 9.
- [35] MacCormack, R.W., "Numerical Solution of the Interaction of a Shock Wave with a Laminar Boundary Layer," *Proc. Second Int. Conf. Num. Methods Fluid Dyn., Lecture Notes in Physics*, vol. 8, Springer-Verlag, New York, 1971, pp. 151-163.
- [36] Eberhardt, S. and Brown, K., "A Shock Capturing Technique for Hypersonic, Chemically Relaxing Flows," AIAA Paper 86-0231, June 1986.
- [37] Oran, E.S. and Boris, J.P., *Numerical Simulation of Reactive Flow*, Elsevier, 1987, Chap. 13.
- [38] Liepmann, H. and Roshko, A., *Fundamentals of Gas Dynamics*, Wiley, 1957.

- [39] Chakravarthy, S.R., Anderson, D.A. and Salas, M.D., "The Split-Coefficient Matrix Method for Hyperbolic Systems of Gasdynamic Equations," AIAA Paper 80-0268, 1980.
- [40] Lyubimov, A.N. and Rusanov, V.V., "Gas Flows Past Blunt Bodies, Part II: Tables of the Gas-Dynamic Functions," NASA TT F-715, Feb. 1973.
- [41] Ruegg, F.W. and Dorsey, W.W., "A Missile Technique for the Study of Detonation Waves," *J. Res. Nat. Bur. Stand.* 66C, Jan. 1962, pp. 51-58.
- [42] Chernyi, G.G., "Supersonic Flow Around Bodies With Detonation and Deflagration fronts," *Astronautica Acta* 13, 1967, pp. 464-480.
- [43] Behrens, H., Struth, W. and Wecken, F., "Shock- Induced Combustion in the Bow Waves of High-Speed Missiles," Deutsch-Französisches Forschungsinstitut, Rep. 2/66, Saint-Louis, France, 1966.
- [44] Lehr, H.F., "Experiments on Shock-Induced Combustion," *Astronautica Acta*, vol. 17, 1972, pp. 589-597.
- [45] Fujiwara, T., Matsuo, A. and Nomoto, H., "A Two-Dimensional Detonation Supported by a Blunt Body or a Wedge," AIAA Paper 88-0098, Jan. 1988.
- [46] Lee, S. and Deiwert, G.S., "Calculation of Nonequilibrium Hydrogen-Air Reactions with Implicit Flux Vector Splitting Method," AIAA Paper 89-1700, June 1989.
- [47] Prabhu, R., Thareja, R. and Stewart, J., "A Navier-Stokes Solver for High Speed Equilibrium Flows and Application to Blunt Bodies," AIAA Paper 89-0668, Jan. 1989.

Appendix A

EXPRESSIONS FOR THE CHEMICAL SOURCE TERM

The procedure described in section 2.4 for calculating the chemical source term is applied here to the combustion model presented in section 2.3. The seven species, H , O , H_2O , OH , O_2 , H_2 , and an inert species, will be numbered 1, 2, 3, 4, 5, 6 and 7. The eight reactions of the combustion model are listed below

1. $H + O_2 \rightleftharpoons OH + O$
2. $O + H_2 \rightleftharpoons OH + H$
3. $H_2 + OH \rightleftharpoons H + H_2O$
4. $2OH \rightleftharpoons O + H_2O$
5. $H_2 + X \rightleftharpoons 2H + X$
6. $H_2O + X \rightleftharpoons OH + H + X$
7. $OH + X \rightleftharpoons O + H + X$
8. $O_2 + X \rightleftharpoons 2O + X$

Remembering that \tilde{y}_i is the concentration of species i , and $\dot{\tilde{y}}_{i,j}$ denotes the rate of change of the concentration of species i in reaction j , equations (2.11) now read

$$\dot{\tilde{y}}_{21} = K_{f,1}\tilde{y}_1\tilde{y}_5 - K_{b,1}\tilde{y}_2\tilde{y}_4 \quad \dot{\tilde{y}}_{41} = \dot{\tilde{y}}_{21} \quad \dot{\tilde{y}}_{11} = \dot{\tilde{y}}_{51} = -\dot{\tilde{y}}_{21} \quad (A.1)$$

$$\dot{\tilde{y}}_{12} = K_{f,2}\tilde{y}_2\tilde{y}_6 - K_{b,2}\tilde{y}_1\tilde{y}_4 \quad \dot{\tilde{y}}_{42} = \dot{\tilde{y}}_{12} \quad \dot{\tilde{y}}_{22} = \dot{\tilde{y}}_{62} = -\dot{\tilde{y}}_{12} \quad (A.2)$$

$$\dot{\tilde{y}}_{13} = K_{f,3}\tilde{y}_6\tilde{y}_4 - K_{b,3}\tilde{y}_1\tilde{y}_3 \quad \dot{\tilde{y}}_{33} = \dot{\tilde{y}}_{13} \quad \dot{\tilde{y}}_{63} = \dot{\tilde{y}}_{43} = -\dot{\tilde{y}}_{13} \quad (A.3)$$

$$\dot{\tilde{y}}_{24} = K_{f,4}\tilde{y}_4^2 - K_{b,4}\tilde{y}_2\tilde{y}_3 \quad \dot{\tilde{y}}_{34} = \dot{\tilde{y}}_{24} \quad \dot{\tilde{y}}_{44} = -2\dot{\tilde{y}}_{24} \quad (A.4)$$

$$\dot{\tilde{y}}_{15} = K_{f,5}\tilde{y}_6\tilde{Y} - K_{b,5}\tilde{y}_1^2\tilde{Y} \quad \dot{\tilde{y}}_{65} = -\frac{1}{2}\dot{\tilde{y}}_{15} \quad (\text{A.5})$$

$$\dot{\tilde{y}}_{16} = K_{f,6}\tilde{y}_3\tilde{Y} - K_{b,6}\tilde{y}_1\tilde{y}_4\tilde{Y} \quad \dot{\tilde{y}}_{46} = \dot{\tilde{y}}_{16} \quad \dot{\tilde{y}}_{36} = -\dot{\tilde{y}}_{16} \quad (\text{A.6})$$

$$\dot{\tilde{y}}_{17} = K_{f,7}\tilde{y}_4\tilde{Y} - K_{b,7}\tilde{y}_1\tilde{y}_2\tilde{Y} \quad \dot{\tilde{y}}_{27} = \dot{\tilde{y}}_{17} \quad \dot{\tilde{y}}_{47} = -\dot{\tilde{y}}_{17} \quad (\text{A.7})$$

$$\dot{\tilde{y}}_{28} = K_{f,8}\tilde{y}_5\tilde{Y} - K_{b,8}\tilde{y}_2^2\tilde{Y} \quad \dot{\tilde{y}}_{58} = -\frac{1}{2}\dot{\tilde{y}}_{28} \quad (\text{A.8})$$

where \tilde{Y} represents the sum of the concentrations of all species:

$$\tilde{Y} = \sum_{i=1}^7 \tilde{y}_i \quad (\text{A.9})$$

Equations (2.12) now read:

$$\dot{\tilde{y}}_1 = \dot{\tilde{y}}_{11} + \dot{\tilde{y}}_{12} + \dot{\tilde{y}}_{13} + \dot{\tilde{y}}_{15} + \dot{\tilde{y}}_{16} + \dot{\tilde{y}}_{17} \quad (\text{A.10})$$

$$\dot{\tilde{y}}_2 = \dot{\tilde{y}}_{21} - \dot{\tilde{y}}_{12} + \dot{\tilde{y}}_{24} + \dot{\tilde{y}}_{17} + \dot{\tilde{y}}_{28} \quad (\text{A.11})$$

$$\dot{\tilde{y}}_3 = \dot{\tilde{y}}_{13} + \dot{\tilde{y}}_{24} - \dot{\tilde{y}}_{16} \quad (\text{A.12})$$

$$\dot{\tilde{y}}_4 = \dot{\tilde{y}}_{21} + \dot{\tilde{y}}_{12} - \dot{\tilde{y}}_{13} - 2\dot{\tilde{y}}_{24} + \dot{\tilde{y}}_{16} - \dot{\tilde{y}}_{17} \quad (\text{A.13})$$

$$\dot{\tilde{y}}_5 = -\dot{\tilde{y}}_{21} - \frac{1}{2}\dot{\tilde{y}}_{28} \quad (\text{A.14})$$

$$\dot{\tilde{y}}_6 = -\dot{\tilde{y}}_{12} - \dot{\tilde{y}}_{13} - \frac{1}{2}\dot{\tilde{y}}_{15} \quad (\text{A.15})$$

The following two equations, which express the conservation of the number of atoms of oxygen and hydrogen, are obtained as linear combinations of equations A.10-A.15

$$2\dot{\tilde{y}}_6 + \dot{\tilde{y}}_1 + \dot{\tilde{y}}_4 + 2\dot{\tilde{y}}_3 = 0 \quad (\text{A.16})$$

$$2\dot{\tilde{y}}_5 + \dot{\tilde{y}}_2 + \dot{\tilde{y}}_4 + \dot{\tilde{y}}_3 = 0 \quad (\text{A.17})$$

Equations (A.16) and (A.17) could replace any two of equations (A.10)-(A.15).

The above expressions for $\dot{\tilde{y}}_i$ ($i = 1, 6$), are then inserted into equations (2.13) and (2.14) for obtaining the chemical source terms w_i .

Appendix B

EXPRESSIONS FOR THE DISSIPATION TERMS

The vector $\alpha_{j+\frac{1}{2}}$ defined in equation (2.25) is given by

$$\alpha_{j+\frac{1}{2}} = \begin{bmatrix} \Delta q_1 - c_1 aa \\ \Delta q_2 - c_2 aa \\ \vdots \\ \Delta q_n - c_n aa \\ (-\xi_y^* u + \xi_x^* v)bb + \xi_y^* \Delta q_{n+1} - \xi_x^* \Delta q_{n+2} \\ \frac{1}{2}(aa - \frac{U^*}{a}bb + \frac{\xi_x^*}{a}\Delta q_{n+1} + \frac{\xi_y^*}{a}\Delta q_{n+2}) \\ \frac{1}{2}(aa + \frac{U^*}{a}bb - \frac{\xi_x^*}{a}\Delta q_{n+1} - \frac{\xi_y^*}{a}\Delta q_{n+2}) \end{bmatrix} \quad (B.1)$$

with

$$\xi_x^* = \frac{\xi_x}{\sqrt{\xi_x^2 + \xi_y^2}} \quad \xi_y^* = \frac{\xi_y}{\sqrt{\xi_x^2 + \xi_y^2}} \quad (B.2)$$

$$U^* = \frac{U}{\sqrt{\xi_x^2 + \xi_y^2}} \quad (B.3)$$

$$aa = \frac{1}{a^2} \left[\sum_{i=1}^n P_{\rho_i} \Delta q_i - p_e (u \Delta q_{n+1} + v \Delta q_{n+2} - \Delta q_{n+3}) \right] \quad (B.4)$$

$$bb = \sum_{i=1}^n \Delta q_i, \quad \Delta q = \frac{q_{j+1,k} J_{j+1,k} - q_{j,k} J_{j,k}}{0.5(J_{j+1,k} + J_{j,k})} \quad (B.5)$$

And it is understood that all the terms are evaluated at $(j + \frac{1}{2}, k)$. The vector $\mathbf{R}\Phi$ which appears in equation (2.20) is given by

$$\mathbf{R}_{j+\frac{1}{2}}\Phi_{j+\frac{1}{2}} = \begin{bmatrix} \phi^1 + c_1 K_1 \\ \phi^2 + c_2 K_1 \\ \vdots \\ \phi^n + c_n K_1 \\ u K_2 + \xi_y^* \phi^{n+1} + \xi_x^* a K_3 \\ v K_2 - \xi_x^* \phi^{n+1} + \xi_y^* a K_3 \\ H K_2 - \frac{1}{p_e} \sum_{i=1}^n a_i^2 \phi^i + a U^* K_3 \\ + (\xi_y^* u - \xi_x^* v) \phi^{n+1} \end{bmatrix} \quad (\text{B.6})$$

with

$$K_1 = \phi^{n+2} + \phi^{n+3}, \quad K_2 = \sum_{i=1}^{n+3} \phi^i$$

$$K_3 = \phi^{n+2} - \phi^{n+3}$$

where the elements, ϕ^l , of the dissipation vector are given by equation (2.22). The eigenvalues, $a_{j+\frac{1}{2}}^l$, are given by

$$(a_{j+\frac{1}{2}}^1, \dots, a_{j+\frac{1}{2}}^{n+3}) = (U, \dots, U, U, U + a\sqrt{\xi_x^2 + \xi_y^2}, U - a\sqrt{\xi_x^2 + \xi_y^2})_{j+\frac{1}{2}, k} \quad (\text{B.7})$$

The frozen sound speed a is

$$a^2 = p_\rho + p_e(H - u^2 - v^2) \quad (\text{B.8})$$

with H being the total enthalpy per unit mass. Also the following relations are needed

$$p_{\rho_i} = \frac{RT}{M_i}(1 - p_e) + p_e\left(\frac{u^2 + v^2}{2} - \int^T c_{p_i} dT - h_i^0\right) \quad (\text{B.9})$$

$$p_e = \sum_{i=1}^n \frac{c_i}{M_i} \frac{R}{c_v} \quad (\text{B.10})$$

$$p_\rho = \sum_{i=1}^n c_i p_{\rho_i} \quad (\text{B.11})$$

Similar expressions for $\alpha_{k+\frac{1}{2}}$ and $\mathbf{R}_{k+\frac{1}{2}}\Phi_{k+\frac{1}{2}}$ are obtained by replacing ξ_x by η_x , ξ_y by η_y and U by V .

Appendix C

CALCULATION OF THE SCALING MATRIX

The scaling matrix \mathbf{D} for the predictor and corrector steps of the numerical algorithm was defined in equations (2.21). Taking the predictor step for example, we rewrite the first of equations (2.21) below

$$\mathbf{D} = (\mathbf{I} - \Delta t \theta \frac{\partial \mathbf{W}}{\partial \mathbf{q}}) \quad (\text{C.1})$$

where we have dropped the superscript n for clarity. In section 2.6 we partitioned this matrix in order to simplify the calculations

$$\mathbf{D} = \begin{pmatrix} \mathbf{D}^{11} & \mathbf{D}^{12} \\ \mathbf{D}^{21} & \mathbf{D}^{22} \end{pmatrix} \quad (\text{C.2})$$

and we noted that \mathbf{D}^{21} is a null matrix, and \mathbf{D}^{22} is an identity matrix. Matrices \mathbf{D}^{11} and \mathbf{D}^{12} are given by

$$\mathbf{D}^{11} = \begin{pmatrix} 1 - \frac{\Delta t \theta}{J-1} \frac{\partial w_1}{\partial \rho_1} & -\frac{\Delta t \theta}{J-1} \frac{\partial w_1}{\partial \rho_2} & \cdots & -\frac{\Delta t \theta}{J-1} \frac{\partial w_1}{\partial \rho_n} \\ -\frac{\Delta t \theta}{J-1} \frac{\partial w_2}{\partial \rho_1} & 1 - \frac{\Delta t \theta}{J-1} \frac{\partial w_2}{\partial \rho_2} & \cdots & -\frac{\Delta t \theta}{J-1} \frac{\partial w_2}{\partial \rho_n} \\ \vdots & \vdots & \ddots & \vdots \\ -\frac{\Delta t \theta}{J-1} \frac{\partial w_n}{\partial \rho_1} & -\frac{\Delta t \theta}{J-1} \frac{\partial w_n}{\partial \rho_2} & \cdots & 1 - \frac{\Delta t \theta}{J-1} \frac{\partial w_n}{\partial \rho_n} \end{pmatrix} \quad (\text{C.3})$$

and

$$\mathbf{D}^{12} = \begin{pmatrix} -\frac{\Delta t \theta}{J-1} \frac{\partial w_1}{\partial M} & -\frac{\Delta t \theta}{J-1} \frac{\partial w_1}{\partial N} & -\frac{\Delta t \theta}{J-1} \frac{\partial w_1}{\partial e} \\ -\frac{\Delta t \theta}{J-1} \frac{\partial w_2}{\partial M} & -\frac{\Delta t \theta}{J-1} \frac{\partial w_2}{\partial N} & -\frac{\Delta t \theta}{J-1} \frac{\partial w_2}{\partial e} \\ \vdots & \vdots & \vdots \\ -\frac{\Delta t \theta}{J-1} \frac{\partial w_n}{\partial M} & -\frac{\Delta t \theta}{J-1} \frac{\partial w_n}{\partial N} & -\frac{\Delta t \theta}{J-1} \frac{\partial w_n}{\partial e} \end{pmatrix} \quad (\text{C.4})$$

where we have used the notation $M = \rho u$, and $N = \rho v$. Also, all the partial derivatives are evaluated holding all the other variables constant. That is

$$\frac{\partial w_i}{\partial \rho_j} = \left(\frac{\partial w_i}{\partial \rho_j} \right)_{\rho_k, M, N, e} \quad k = 1, \dots, j-1, j+1, \dots, n \quad (\text{C.5})$$

$$\frac{\partial w_i}{\partial M} = \left(\frac{\partial w_i}{\partial M} \right)_{\rho_j, N, e} \quad j = 1, \dots, n \quad (C.6)$$

and similarly for the other derivatives. The source terms w_i were derived in section 2.4. From equations (2.13) and (2.14), we can write the following expression for w_i

$$w_i = \frac{J^{-1} \tau_f}{\rho_\infty} M_i(\dot{\bar{y}}_i) \quad (C.7)$$

where τ_f is a characteristic convection time defined as $\tau_f = L c_\infty$, and $\dot{\bar{y}}_i$ is obtained from equations (2.11) and (2.12). The partial derivatives that appear in matrix **D** are evaluated as follows

$$\frac{1}{J^{-1}} \left(\frac{\partial w_i}{\partial \rho_j} \right)_{\rho_k, M, N, e} = \frac{\tau_f}{\rho_\infty} M_i \left(\frac{\partial \dot{\bar{y}}_i}{\partial \rho_j} \right)_{\rho_k, M, N, e} \quad (C.8)$$

$$\rho_j = \frac{M_j \bar{y}}{\rho_\infty} \quad (C.9)$$

therefore

$$\frac{1}{J^{-1}} \left(\frac{\partial w_i}{\partial \rho_j} \right)_{\rho_k, M, N, e} = \tau_f \frac{M_i}{M_j} \left(\frac{\partial \dot{\bar{y}}_i}{\partial \bar{y}_j} \right)_{\rho_k, M, N, e} \quad (C.10)$$

Similarly, we can write the following equations

$$\frac{1}{J^{-1}} \left(\frac{\partial w_i}{\partial M} \right)_{\rho_j, N, e} = \tau_f c_\infty \left(\frac{\partial \dot{\bar{y}}_i}{\partial \bar{M}} \right)_{\rho_j, N, e} \quad (C.11)$$

$$\frac{1}{J^{-1}} \left(\frac{\partial w_i}{\partial N} \right)_{\rho_j, M, e} = \tau_f c_\infty \left(\frac{\partial \dot{\bar{y}}_i}{\partial \bar{N}} \right)_{\rho_j, M, e} \quad (C.12)$$

$$\frac{1}{J^{-1}} \left(\frac{\partial w_i}{\partial e} \right)_{\rho_j, M, N} = \tau_f c_\infty^2 \left(\frac{\partial \dot{\bar{y}}_i}{\partial \bar{e}} \right)_{\rho_j, M, N} \quad (C.13)$$

These derivatives are calculated in a straightforward manner. The only difficulty is associated with the fact that $\dot{\bar{y}}_i$ depends on the temperature (through the rate constants K_f and K_b) and therefore, on all the rest of the variables (through the energy equation). Thus, we have to evaluate the following derivatives

$$\left(\frac{\partial K_i}{\partial \bar{y}_j} \right)_{\rho_k, M, N, e} \quad \left(\frac{\partial K_i}{\partial \bar{M}} \right)_{\rho_j, N, e} \quad \text{etc.} \quad (C.14)$$

where K_i denotes either the forward or backward reaction rate. These derivatives are calculated as follows:

$$\frac{\partial K_i}{\partial \bar{y}_j} = \frac{\partial K_i}{\partial \bar{T}} \frac{\partial \bar{T}}{\partial \bar{y}_j} = \frac{\gamma T_\infty}{\rho_\infty / M_j} \frac{\partial K_i}{\partial \bar{T}} \frac{\partial T}{\partial \rho_j} \quad (\text{C.15})$$

therefore

$$\left(\frac{\partial K_i}{\partial \bar{y}_j} \right)_{\rho_k, M, N, e} = \frac{\gamma T_\infty M_j}{\rho_\infty} \frac{\partial K_i}{\partial \bar{T}} \left(\frac{\partial T}{\partial \rho_j} \right)_{\rho_k, M, N, e} \quad (\text{C.16})$$

$$\left(\frac{\partial K_i}{\partial M} \right)_{\rho_j, N, e} = \frac{\gamma T_\infty}{\rho_\infty c_\infty} \frac{\partial K_i}{\partial \bar{T}} \left(\frac{\partial T}{\partial M} \right)_{\rho_j, N, e} \quad (\text{C.17})$$

and similarly for $\frac{\partial K_i}{\partial N}$. The last derivative needed is

$$\left(\frac{\partial K_i}{\partial \bar{e}} \right)_{\rho_j, M, N} = \frac{\gamma T_\infty}{\rho_\infty c_\infty^2} \frac{\partial K_i}{\partial \bar{T}} \left(\frac{\partial T}{\partial e} \right)_{\rho_j, N, e} \quad (\text{C.18})$$

The derivatives involving the temperature T in equations (C.16) to (C.18) are obtained from the definition of total energy. They are obtained as follows.

First, we rewrite below the equation for the total energy (equation (2.6))

$$\sum_{j=1}^n \rho_j e_j^{\text{int}} = e - \frac{(M^2 + N^2)}{2\rho} - \sum_{j=1}^n \rho_j h_j^0 \quad (\text{C.19})$$

where the following notation has been used:

$$e_j^{\text{int}} = \int^T c_{vj} dT \quad (\text{C.20})$$

Taking the derivative of the above equation with respect to ρ_i we obtain

$$\sum_{j=1}^n \rho_j \frac{\partial e_j^{\text{int}}}{\partial T} \left(\frac{\partial T}{\partial \rho_i} \right)_{\rho_k, M, N, e} + e_j^{\text{int}} \left(\frac{\partial \rho_j}{\partial \rho_i} \right)_{\rho_k, M, N, e} = - \frac{(M^2 + N^2)}{2} \frac{1}{\rho^2} - \sum_{j=1}^n h_j^0 \left(\frac{\partial \rho_j}{\partial \rho_i} \right)_{\rho_k, M, N, e} \quad (\text{C.21})$$

Note that

$$\left(\frac{\partial \rho_j}{\partial \rho_i} \right)_{\rho_k, M, N, e} = \begin{cases} 0 & j \neq i \\ 1 & j = i \end{cases} \quad (\text{C.22})$$

therefore

$$\left(\sum_{j=1}^n \rho_j c_{vj} \right) \left(\frac{\partial T}{\partial \rho_i} \right)_{\rho_k, M, N, e} + e_i^{\text{int}} = \frac{1}{2} (u^2 + v^2) - h_i^0 \quad (\text{C.23})$$

and finally

$$\left(\frac{\partial T}{\partial \rho_i}\right)_{\rho_k, M, N, e} = \frac{e_i^{int} + \frac{1}{2}(u^2 + v^2) - h_i^0}{\rho c_v} \quad (C.24)$$

Similarly, we obtain the following expressions for the rest of the derivatives

$$\left(\frac{\partial T}{\partial M}\right)_{\rho_j, N, e} = -\frac{u}{\rho c_v} \quad (C.25)$$

$$\left(\frac{\partial T}{\partial N}\right)_{\rho_j, M, e} = -\frac{v}{\rho c_v} \quad (C.26)$$

$$\left(\frac{\partial T}{\partial e}\right)_{\rho_j, M, N} = -\frac{1}{\rho c_v} \quad (C.27)$$

of shock waves and contact discontinuities without spurious oscillations.
It should be pointed out that all the high order PDEs obtained in this

Appendix D

TVD SCHEMES: FUNDAMENTAL CONCEPTS

Total variation diminishing (TVD) schemes provides an example that sophisticated mathematical analysis can be just as important in developing computational methods as it has been for analytical methods. The notion of TVD schemes was introduced by Harten¹. Based on this concept, explicit and implicit second-order accurate TVD schemes were developed by Harten², Roe³, Yee⁴, Davis⁵, Yee and Harten⁶ and Yee and Shinn⁷. Recently, Wada et.al.⁸ have proposed a new third-order TVD Scheme. Some of these methods can be viewed as three-point central difference schemes with a "smart" numerical dissipation. The addition of numerical dissipation is needed for two reasons^{9,10}: first, to control the odd-even uncoupling of grid points typical of central differencing and, second, to allow the clean capture of shock waves and contact discontinuities without spurious oscillations.

It should be pointed out that all the high-order TVD schemes are constructed so that no spurious oscillations are generated for one-dimensional nonlinear scalar hyperbolic conservation laws and constant coefficient hyperbolic systems. The resulting schemes are then formally extended to nonlinear hyperbolic systems.

Another important aspect of TVD schemes is that, a crucial estimate involved in convergence proofs on difference approximation to nonlinear scalar hyperbolic equations is a bound on the total variation (to be defined below) of the solution.

In order to illustrate how TVD schemes are constructed, let's consider the following equation

$$\frac{\partial u}{\partial t} + a \frac{\partial u}{\partial x} = 0 \quad (\text{D.1})$$

on a rectangular mesh $x = j\Delta x$, $t = n\Delta t$. Let u_j^n be the numerical solution of equation (D.1) at point (j, n) . The total variation of a mesh function u^n is defined to be

$$TV(u^n) = \sum_{j=-\infty}^{\infty} |u_{j+1}^n - u_j^n| \quad (\text{D.2})$$

A numerical scheme is said to be TVD if

$$TV(u^{n+1}) \leq TV(u^n) \quad (D.3)$$

When deriving second order TVD schemes, the numerical method is usually written in the following general form

$$u_j^{n+1} = u_j^n - C_{j-\frac{1}{2}} \Delta u_{j-\frac{1}{2}} + D_{j+\frac{1}{2}} \Delta u_{j+\frac{1}{2}} \quad (D.4)$$

where, $C_{j-\frac{1}{2}}$ and $D_{j+\frac{1}{2}}$ are coefficients that depend on the set u_j , and $\Delta u_{j+\frac{1}{2}} = u_{j+1}^n - u_j^n$. Then it can be easily shown¹ that sufficient conditions for the scheme to be TVD are the inequalities

$$C_{j-\frac{1}{2}} \geq 0 \quad \forall j \quad (D.5)$$

$$D_{j+\frac{1}{2}} \geq 0 \quad \forall j \quad (D.6)$$

$$C_{j+\frac{1}{2}} + D_{j+\frac{1}{2}} \leq 1 \quad \forall j \quad (D.7)$$

A good example of this approach is given by Roe's³ derivation of the TVD Lax-Wendroff scheme. In his derivation, Roe considered a scheme of the following form

$$\begin{aligned} u_j^{n+1} = & u_j^n - \frac{1}{2}\nu(1+\nu)\Delta u_{j-\frac{1}{2}} - \frac{1}{2}\nu(1-\nu)\Delta u_{j+\frac{1}{2}} \\ & - \frac{1}{2}|\nu|(1-|\nu|)(\Delta u_{j-\frac{1}{2}} - Q_{j-\frac{1}{2}}) \\ & + \frac{1}{2}|\nu|(1-|\nu|)(\Delta u_{j+\frac{1}{2}} - Q_{j+\frac{1}{2}}) \end{aligned} \quad (D.8)$$

Here, $\nu = a\Delta t/\Delta x$. The first line represents the usual Lax-Wendroff scheme, and the other terms represent an additional conservative dissipation. The function $Q_{j+\frac{1}{2}}$ depends on three consecutive gradients $\Delta u_{j-\frac{1}{2}}$, $\Delta u_{j+\frac{1}{2}}$ and $\Delta u_{j+\frac{3}{2}}$, and is of the form

$$Q_{j+\frac{1}{2}} = Q(\Delta u_{j-\frac{1}{2}}, \Delta u_{j+\frac{1}{2}}, \Delta u_{j+\frac{3}{2}}) \quad (D.9)$$

The function Q is chosen in such a way as to ensure that the scheme given by equation (D.8) is TVD. For this purpose, the scheme is written in the form given by equation (D.4). For example, in the case $\nu > 0$, scheme (D.8) can be written as

$$u_j^{n+1} = u_j^n - \nu[1 - \frac{1}{2}(1-\nu)Q_{j-\frac{1}{2}}/\Delta u_{j-\frac{1}{2}} + \frac{1}{2}(1-\nu)Q_{j+\frac{1}{2}}/\Delta u_{j-\frac{1}{2}}]\Delta u_{j-\frac{1}{2}} \quad (D.10)$$

which is of the form (D.4) with $D_{j+\frac{1}{2}} = 0$, and

$$C_{j-\frac{1}{2}} = \nu[1 - \frac{1}{2}(1 - \nu)Q_{j-\frac{1}{2}}/\Delta u_{j-\frac{1}{2}} + \frac{1}{2}(1 - \nu)Q_{j+\frac{1}{2}}/\Delta u_{j-\frac{1}{2}}] \quad (D.11)$$

If one assumes that $Q_{j+\frac{1}{2}}/\Delta u_{j+\frac{1}{2}}$ and $Q_{j+\frac{1}{2}}/\Delta u_{j+\frac{3}{2}}$ are always positive, then Roe³ shows that a set of sufficient conditions for equation (D.8) to be TVD is

$$\frac{Q_{j+\frac{1}{2}}}{\Delta u_{j-\frac{1}{2}}} < \frac{2}{|\nu|} \quad (D.12)$$

$$\frac{Q_{j+\frac{1}{2}}}{\Delta u_{j+\frac{1}{2}}} < \frac{2}{1 - |\nu|} \quad (D.13)$$

$$\frac{Q_{j+\frac{1}{2}}}{\Delta u_{j+\frac{3}{2}}} < \frac{2}{|\nu|} \quad (D.14)$$

Some examples of the "limiter" function Q , that satisfies the above conditions, are⁴

$$\begin{aligned} Q(\Delta u_{j-\frac{1}{2}}, \Delta u_{j+\frac{1}{2}}, \Delta u_{j+\frac{3}{2}}) &= \minmod(\Delta u_{j+\frac{1}{2}}, \Delta u_{j-\frac{1}{2}}) \\ &+ \minmod(\Delta u_{j+\frac{1}{2}}, \Delta u_{j+\frac{3}{2}}) - \Delta u_{j+\frac{1}{2}} \end{aligned} \quad (D.15)$$

$$Q(\Delta u_{j-\frac{1}{2}}, \Delta u_{j+\frac{1}{2}}, \Delta u_{j+\frac{3}{2}}) = \minmod(\Delta u_{j-\frac{1}{2}}, \Delta u_{j+\frac{1}{2}}, \Delta u_{j+\frac{3}{2}}) \quad (D.16)$$

$$Q(\Delta u_{j-\frac{1}{2}}, \Delta u_{j+\frac{1}{2}}, \Delta u_{j+\frac{3}{2}}) = \supb(\Delta u_{j+\frac{1}{2}}, \Delta u_{j-\frac{1}{2}}) + \supb(\Delta u_{j+\frac{1}{2}}, \Delta u_{j+\frac{3}{2}}) - \Delta u_{j+\frac{1}{2}} \quad (D.17)$$

$$Q(\Delta u_{j-\frac{1}{2}}, \Delta u_{j+\frac{1}{2}}, \Delta u_{j+\frac{3}{2}}) = \vl(\Delta u_{j+\frac{1}{2}}, \Delta u_{j-\frac{1}{2}}) + \vl(\Delta u_{j+\frac{1}{2}}, \Delta u_{j+\frac{3}{2}}) - \Delta u_{j+\frac{1}{2}} \quad (D.18)$$

The *minmod* function of a list of arguments is equal to the smallest number in absolute value if the list of arguments is of the same sign, or is equal to zero if any argument is of the opposite sign. The functions *supb*(x, y) and *vl*(x, y) are defined as follows

$$\supb(x, y) = \operatorname{sgn}(x)[\max\{0, \min(2|x|, \operatorname{sgn}(x)y), \min(|x|, \operatorname{sgn}(x)2y)\}] \quad (D.19)$$

and

$$\vl(x, y) = \frac{xy + |xy|}{x + y} \quad (D.20)$$

The limiter given by equation (D.17), due to Roe¹¹ and nicknamed "superbee," is the most compressive among the above four Q functions. The limiter given by equation (D.18) is due to Van Leer¹². The limiter form used in the present study is the one given in equation (D.16). A comparison of the various limiters was presented by Sweby¹³, who also shows that the above limiters preserve the second order accuracy of the numerical scheme.

The numerical method used in the present study (described in section 2.5) is an extension of the scalar explicit TVD Lax-Wendroff scheme (described above) in predictor-corrector form for the nonlinear hyperbolic system given in equation 2.2. Some of the details of the extension procedure are given in Ref. 4.

References

1. Harten, A., "High Resolution Schemes for Hyperbolic Conservation Laws," *Journal of Computational Physics*, vol. 49, 1983, pp. 357-393.
2. Harten, A., "On a Class of High Resolution Total Variation Stable Finite-Difference Schemes," *SIAM Journal of Numerical Analysis*, vol. 21, No. 1, Feb. 1984, pp. 1-23.
3. Roe, P.L., "Generalized Formulation of TVD Lax-Wendroff Schemes," Inst. for Computer Applications in Science and Engineering, Hampton, VA, Rept. 84-53, Oct. 1984.
4. Yee, H.C., "Construction of Explicit and Implicit Symmetric TVD Schemes and Their Applications," *Journal of Computational Physics*, vol. 68, Jan. 1987, pp. 151-179.
5. Davis, S.F., "TVD Finite Difference Schemes and Artificial Viscosity," Inst. for Computer Applications in Science and Engineering, Hampton, VA, Rept. 84-20, June 1984.
6. Yee, H.C. and Harten, A., "Implicit TVD Schemes for Hyperbolic Conservation Laws in Curvilinear Coordinates," *AIAA Journal*, vol. 25, Feb. 1987, pp. 266-274.
7. Yee, H.C. and Shinn, J.L., "Semi-Implicit and Fully Implicit Shock-Capturing Methods for Nonequilibrium Flows," *AIAA Journal*, vol. 27, March 1989, pp. 299-307.
8. Wada, Y., Kubota, H., Ogawa, S. and Ishiguro, T., "A Diagonalizing Formulation Of General Real Gas-Dynamic Matrices with a New Class of TVD Schemes," AIAA Paper 88-3596-CP, 1988.
9. Jameson, A., "Successes and Challenges in Computational Aerodynamics," AIAA Paper 87-1184-CP, 1987.

10. Pulliam, T.H., "Artificial Dissipation Models for the Euler Equations," *AIAA Journal*, vol. 24, No. 12, Dec. 1986.
11. Roe, P.L., "in *Proceedings of the AMS-SIAM Summer Seminar on Large-Scale Computation in Fluid Mechanics*, 1983, edited by B.E. Engquist et.al. Lectures in Applied Mathematics, vol. 22, pp. 163.
12. Van Leer, B., "Towards the Ultimate Conservative Difference Scheme,II. Monotonicity and Conservation Combined in a Second Order Scheme," *Journal of Computational Physics*, vol. 14, 1974, pp. 361-370.
13. Sweby, P.K., "High Resolution Schemes Using Flux Limiters for Hyperbolic Conservation Laws," *SIAM Journal of Numer. Anal.*, vol. 21 , No. 5, Oct. 1984.

Vita

Name: Shaye Yungster.

Date of birth: November 25 1958.

Place of birth: Mexico city, Mexico.

Education

B.Sc. Aeronautical Engineering, Technion-Israel Institute of Technology.

Date of graduation: July 1981.

M.Sc. Aeronautical Engineering, Technion-Israel Institute of Technology.

Major field: Aerodynamics and Fluid Mechanics.

Date of graduation: July 1985.

Ph.D. Aeronautics and Astronautics, University of Washington.

Date of graduation: October 1989.